Use of Secondary Sphere Hydrogen Bonds for Stabilization and Divergent Reactivity in Transition Metal Complexes

by

Jessica R. Wilson

A dissertation submitted in partial fulfillment
of the requirements for the degree of
Doctor of Philosophy
(Chemistry)
in the University of Michigan
2022

Doctoral Committee:

Professor Nathaniel K. Szymczak, Chair
Professor Nicolai Lehnert
Professor Anne J. McNeil
Associate Professor Alison Narayan

Jessica Wilson

jessrwil@umich.edu

ORCID iD: 0000-0002-7116-4737

Dedication

This thesis is dedicated to the Wilsons – I couldn’t have done this without you.

Thank you, and I love you.

Acknowledgements

I wish to acknowledge and express my deepest gratitude to those who have made the completion of this thesis possible, both academically and personally, and to those without whom I would not have had such a wonderful experience at the University of Michigan and in Ann Arbor. I am sure to have missed someone – know that I am grateful for you.

First, the completion of this dissertation in its current form would not have been possible without Nate Szymczak. Nate opened his lab to me despite the fact I had never been trained as an inorganic chemist and had only the most rudimentary experience in inorganic chemistry at all. I was beyond surprised when he told me he would be happy to have me in his lab, and that the Szymczak group would teach me everything I needed to know to be a successful inorganic chemist. Thank you for that opportunity. My time in your group has been truly formative – I have not only become a better independent scientist, a more skeptical and deeper thinking chemist, I have been challenged in many ways that have allowed me to grow as an individual. Thank you for believing in me so many years ago, and for the assistance along the way to the completion of this thesis.

I would not be a chemist were it not for the fantastic support and instruction from the faculty at Muhlenberg College. My chemistry classes were some of the best experiences in my college career from day one, and without them I would not be writing this today. I especially need to thank my research advisor, Dr. Marsha Baar, for taking me on as a very young research student, with only her honors organic chemistry class as experience. Dr. Baar, thank you for your guidance and support during my time at Muhlenberg – you helped me realize my love of chemistry research and to develop the confidence to move into graduate school, even if I did decide not to be an

organic chemist after all. I would be remiss if I did not also thank Dr. Bruce Anderson and Dr. Christine Ingersoll – both chairs of the department – as they helped foster an amazing environment for young chemists and have maintained an excellent undergraduate research program at Muhlenberg that I and many other students have and continue to benefit from greatly. Dr. Ingersoll, I'm so grateful for your help in getting me in contact with Dr. Anne McNeil at the University of Michigan for summer research. It set me on the path to the completion of this thesis, and your support during that time was particularly helpful. Thank you!

I would not be at the University of Michigan if not for Dr. Anne McNeil. Your willingness to host me for a summer of undergraduate research was crucial in my development as a chemist and gave me the incredible opportunity to see what the graduate school experience was like at Michigan. I called it my "dry run" of grad school, and it proved to me that I not only wanted to pursue a graduate degree in chemistry, but also gave me the chance to try new approaches to chemistry and research. I am forever grateful for that opportunity. Thank you also for the chance to spend a rotation in your lab for a semester: it was a great learning experience. Since then, having you on my committee has been incredibly beneficial. Your thoughtful comments and support during Nate's sabbatical made me a better, more independent scientist, and I am very grateful.

I must also thank my other committee members, Dr. Nicolai Lehnert, and Dr. Alison Narayan. Your feedback and encouragement during our meetings over the past few years have been invaluable. The ability to work in a department with such incredible scientists and leaders like you has not been lost on me, and I greatly appreciate your guidance through this degree.

I have many thanks to pass out to the members of Szymczak group. First and foremost, to Lily Hale, who was my mentor during my rotation, and quickly became a lifelong friend and colleague. My first impression of "wow she's so smart, and also a little scary, maybe don't mess with her" was spot on, but having you in my corner, to help me think about chemistry, and propose new hypotheses and generally discuss grad school has been incredibly important for my development as a scientist. You were a major reason for my joining the Szymczak lab, and I am very gratefully for that. Your support even long after you graduated means the world to me, and I cannot thank you enough. I am proud to have you as a friend and mentor. Eric Dahl also deserves special thanks, as Nate plopped me onto a project related to his only a short six months before he defended, and he still managed to find time to help bring me into the hydrogen bonding group. Your help in teaching me e-chem, Schlenk technique, and how to wrangle H-bonding complexes was helpful in spring-boarding me into this thesis work, so thank you. John Kiernicki (Kiernicky? Kiernikki? Kiernickee?) joined Nate's lab only a few weeks before I started, and we spent many years together in adjacent gloveboxes. Thank you for modeling such incredible work ethic and how to be an excellent chemist, and for helping me learn not to be afraid to just try something. Your encouragement, eye for detail, and well-reasoned suggestions helped guide me through these projects and made me really consider my approach to chemistry. You've been a fantastic colleague and teacher. I must especially thank Michael Wade Wolfe, who has been stuck with me from day one in Nate's lab. You've been one of my most consistent friends throughout grad school, and I would not be here today without you. Your eye as a chemist is excellent, and your always spot-on questions have been so helpful (even when I've been mad that I didn't think about them before). Thanks for being my second pair of eyes, my desk-mate, my lunch partner, my drinking/cigar buddy, and my friend. Cheers! And lastly, Emily Norwine, who was one of my personal recruits to the lab, and who has been an excellent lab-mate and friend since the day she first showed up. Thank you for asking me the hard questions, for letting me talk your ear off when I need to vent, and for being a true light in our lab. You have become an amazing chemist in your time with us, and I can’t wait to see what else you do with your career. I leave the group knowing they’re in good hands with you leading the way.

To the remaining members of the Szymczak lab, of whom there are many – thank you for your support, your suggestions, your many questions, and your friendship through the years. Jacob, Jim, Grayson, Cheyanne, Wei, Shreya, Andrew, Dan, Chris, Jiaxiang, Shuo, Zhongyuan, Lucy, and Trey: you’ve made the Szymczak group a really incredible place to work and working with you has been truly a pleasure. I wish you all the best.

A special thanks needs to be said to the students I’ve mentored in my time here. First, to Michael Lengel, who rotated with us during one of most ridiculous semesters I’ve ever experienced in the fall of 2020: thank you for bearing with me during that semester. I truly enjoyed working with you and guiding your project as you got into the groove of graduate research. The Lehnert group is lucky to have you, and I count myself lucky to have been able to mentor you for a semester. Jared Gonder, you’ve had quite the tumultuous time as an undergrad in our group with the lab shut-downs and inability to work with us for almost a year. Having you come back into the lab this fall was truly a wonderful day for me, and it has been pleasure working with you. Watching you grow as a chemist through the past two years has been awesome, and I hope you continue to become the great chemist I know you are. I applaud your diligence and your dedication to working in our lab, learning new chemistry, and will miss working with you. Thanks for making me a better mentor. Taylor Soucy, being your friend and unofficial mentor over the years has been a pleasure and a support structure I never knew I needed. Thank you for making grad school fun, for being a solid sounding board, and for your friendship. Grad school wouldn’t have been the same without you! And lastly, to Jessica Tami – my mentee through the departmental mentoring program, having Liz Oxford match us that first year was life-changing. I know I was supposed to be your mentor, and I know I did my absolute best to guide you through some seriously rocky parts of grad school, but I have to thank you for all the support you have given me in return. You made some of the hardest years of grad school bearable, you've made the fun times even more enjoyable, and I am wholly better person because of you.

I must also take the time to thank my many friends outside of the Szymczak lab but still embedded within the department, the LSI, and the hospital. I have had the pleasure of forming several long-standing friendships throughout the course of graduate school, without whom I would not have enjoyed my time in Ann Arbor nearly as much. Sam, Ted, Justin (and Emily), Wes, Zach, Matt H., and Joe; Sam, Brennan, Jorge, Alex, and Nick; John, Kathleen, and the residents - thank you for your years of friendship, and I look forward to seeing you all in social settings again outside of Ann Arbor! And Olivia, who has been a truly fantastic roommate and friend for nearly six years: thanks for putting up with me and my quirks, for being such a good friend, and for bringing me along as a fake member of the Mapp lab for all these years. It means the world.

And finally, and perhaps most importantly, I must thank my family. My extended family, my grandparents and aunt, but especially Steve, Lori, and Corinne: I think you know that I depend on you for support and guidance and have in particular through my time in grad school. I think now is time to say, from the bottom of my heart: thank you. Thank you for the (near daily) phone calls, for the care packages, funny texts/DMs, for the trips home and trips to Ann Arbor. Thank you for being a shoulder to cry on (literally and metaphorically *via* long distance), for helping me pick myself up and giving me pep talks, and for supporting me in all my decisions. Thank you for giving me the opportunity to even be here, by providing me with so many opportunities to become a good student and for helping me find ways to be successful in whatever I've decided to do. I truly would not have made it to this point without the three of you. Your love, your support, and your encouragement have made me who I am, and made this thesis, this degree, possible. I am so proud to be a Wilson. Words are starting to fail me, so I’ll simply say, thank you, and I love you.

- *Jessi*

Table of Contents

List of Tables

List of Figures

Abstract

This dissertation describes advances made in the synthesis and reactivity of first row transition metal complexes featuring ligands with secondary sphere hydrogen bonding moieties. Inspiration for these complexes comes from biological systems, in which metalloenzymes incorporate outer sphere acidic residues for a variety of purposes, including substrate binding and stabilization of reactive intermediates. The difficulty of strategically modifying enzymes and characterization of the resulting species has led to the development of a wide array of synthetic complexes, with the intent of mimicking structures and reactivity observed in the related biological systems. Synthetic systems used to model biological active site reactivity and mechanism have more recently been modified with the addition of secondary sphere acidic residues to better mimic enzyme active sites. In enzymes, such acidic residues are naturally stable even in reducing environments, however, this can present synthetic challenges in model systems. Additionally, while secondary coordination sphere acidic residues can help in the capture and stabilization of elusive and reactive intermediates, observing these intermediates in synthetic model systems remains difficult. With these challenges in minds, we synthesized a series of nickel, iron, and copper complexes with a neutral ligand that features three hydrogen bond donor groups in the secondary coordination sphere. We set out to demonstrate that the secondary sphere hydrogen bonds would enable us to stabilize highly reactive complexes and capture intermediates along small molecule activation pathways. With a set of nickel(II) complexes, we found that the compounds are stable in the presence of strong reductants, allowing us to isolate and characterize a rare nickel(I) complex with hydrogen bonds. This species showed enhanced stability and selective reactivity for fluoride abstraction that a related complex without hydrogen bonds did not. In another study, we used the same ligand to stabilize a high-valent intermediate of dioxygen activation using an iron(II) precursor. On the same timescale, no dioxygen activation was observed when using ligands without hydrogen bonds, indicating they may play a role in stabilizing of the intermediates and products of the oxygen reduction reaction. Finally, a series of copper(I) complexes were synthesized using several ligand variants with varying hydrogen bond donor strength. Capture and reduction of nitrite by these copper(I) complexes was observed, and hydrogen bond donor strength was shown to affect the stability of the complex. Reactions of analogous, stable copper(I) fluoride complexes with a nitrite source resulted in immediate reduction of nitrite, indicating the mechanism of reduction may be dependent on the binding of nitrite to the complex with hydrogen bonds. Together, these studies demonstrate how small molecule activation may be enabled by the presence of secondary sphere hydrogen bonds, which can stabilize reactive intermediates and/or their products, as observed in metalloenzymes.

Chapter 1 Introduction

1.1 Secondary-sphere interactions in biology

Transformations of small molecules in Nature are frequently mediated by transition metal active sites in enzymes.[1] These active sites contain metals bound to amino acid residues (i.e. cysteine and histidine) that make up the primary coordination sphere, which control the geometry and electronic nature of the metal species.[2] Since these active sites are embedded within the larger structure of the enzyme, the transition metal active sites also engage in contacts with acidic residues in the secondary coordination sphere.[3] These non-covalent interactions can consist of Lewis and Brønsted acidic residues such as secondary sphere metals and/or amino acids. Specifically, secondary sphere amino acids can participate in hydrogen bonding (H-bonding) interactions that can play a role in substrate coordination, redox leveling, intermediate stabilization, proton and electron transfer reactions, and substrate activation at the metal active site.[2, 4-6]

A growing body of work has established the prominence of H-bonding moieties in the secondary coordination sphere of enzymatic active sites. Recent work has identified amino acid residues in the [NiFe] hydrogenase enzyme that are critical to substrate binding and subsequent reactivity (Fig 1.1).[7-8] Amino acid residues in the secondary coordination sphere of nitrogenases have been shown to be critical for N_2 binding and protonation at the distal nitrogen.[9-10] Work in the heme and non-heme literature has also established the necessity of secondary sphere acidic residues for substrate positioning at the active site.[3, 11-12] The prevalence of these outer sphere interactions suggests that while many current synthetic systems focus on tuning primary sphere ligands, those moieties in the secondary sphere may have significant effects on the chemistry performed by these systems. This could have important impacts on industrial processes, such as N_2, CO_2, and O_2 reduction, which are energetically inefficient compared to the biological systems that perform the same reactions.

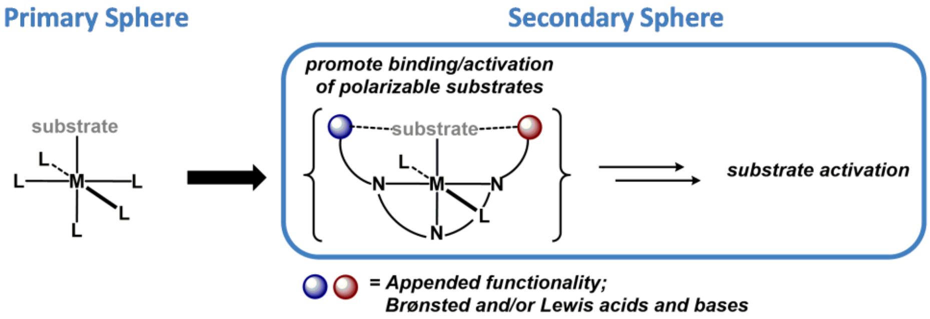

Figure 1.1 Moving towards secondary sphere modifications for small molecule capture and activation in synthetic model systems.

Synthetic models for metalloenzyme active sites often focus on primary coordinate sphere changes. Ligands that directly bind to the metal center have dramatic effects on the ligand field, electronics, and reactivity of the metal complex, however, do not necessarily provide secondary sphere interactions akin to those observed in enzyme active sites. More recently, synthetic model systems have begun to incorporate secondary sphere interactions into ligand scaffolds to promote intramolecular interactions.[3, 13-22] Such appended groups have included sterically bulky groups, Lewis acids and bases, and hydrogen bonding moieties to model sterically protected active sites and outer sphere amino acid residues. By incorporating bulk and/or acidic groups into ligand scaffolds, particularly those which can be tuned, the effects of those secondary sphere interactions can be probed in relationship to binding, stabilization, and activation of small molecule substrates (Fig. 1.1).

1.1.1 Synthetic systems incorporating secondary sphere interactions

Significant contributions have been made in recent years to incorporate secondary sphere moieties in synthetic transition metal complexes. General strategies have incorporated amine or urea-type H-bond donors and typically modify existing ligand frameworks. The Masuda group developed several tris(2-pyridyl)amine (TPA) ligands with steric bulk and H-bonds in the secondary sphere for use in O_2 activation chemistry. The incorporation of pivaloylamino[23] or neopentylamino[24] groups in the secondary sphere as H-bond donors enabled isolation of mononuclear copper and iron complexes with biologically relevant coordination spheres for O_2 activation. Parallel work in the Que group incorporated a phenyl group in the TPA framework, which functioned well to provide steric bulk for the formation of mononuclear complexes, but also suffered from intramolecular C-H activation of the ligand by high-valent intermediates.[25-26]

Other groups have developed a variety of nitrogen-containing ligands with secondary sphere H-bonding moieties. The Nocera group developed porphyrin ligands with appended H-bonds for O_2 and other small molecule activation.[27-29] The Chang group developed non-heme style ligands with both with steric bulk[30] and appended H-bonds[31] for small molecule activation with first row transition metals. The pentadentate ligand N4Py can be appended with neopentyl or phenyl groups, and provide opportunity to compare appended alkyl and aryl amines for H-bonding interactions for O_2 activation.[31] Work in the Borovik group established a new tri-anionic ligand with three appended H-bonding groups – this new framework enabled the isolation of a the first Fe(III)-oxo complex derived from O_2[13] and provided the basis for a wide range of studies for small molecule activation with varieties of the ligand ranging from 0-3 H-bond donors.[32-37] Recent work from the Fout group has introduced a new series of tautomeric H-bond donor and acceptor ligands which have enabled nitrate, perchlorate, nitrite, and O_2 reductions.[38-41] Other ligands developed by

Goldberg and coworkers incorporated both sulfur ligands in the primary sphere and N-H bonds in the secondary sphere as models for dioxygenase enzymes.[42-43]

Advances related to secondary sphere H-bonding in our own group has gone through several iterations. Our interest in structure-function relationship drove us to study the effects of strong H-bond donors for small molecule reductions. Early efforts appended hydroxyl group on the meridional tridentate terpyridine ligand for proton-responsive hydrogenation chemistry.[44] We also designed a new variant of the TPA ligand which was synthesized from hydroxyl pyridine, and could undergo tautomerization to act as either a H-bond donor and/or acceptor.[45] We established that these ligands were difficult to work with in the presence of strong bases and/or reductants, due to their propensity to form dimeric or cluster species. In order to prevent this, we drew from other groups' success by providing additional steric bulk to protect the H-bonding groups. By switching to a phenylamine appended H-bond from a hydroxyl group, steric protection prevented unwanted dimerization, while also enabling a simple route to tune the H-bond donor strength by simply changing the electronics of the appended phenylamine. These -NHPh bond donors enabled isolation of an unusual geometry of copper(I),[46] and isolation of both dicopper peroxo[22] and dizinc peroxo[18] complexes with H-bonding to the bridging O_2 unit (Fig. 1.2). Other ligand development in our group has established difluoromethyl groups as weak H-bond donors that are reductively stable – this has potential to be useful in the study of synthetic models of low-valent active sites, as found in [NiFe] hydrogenase and nitrogenase.[47]

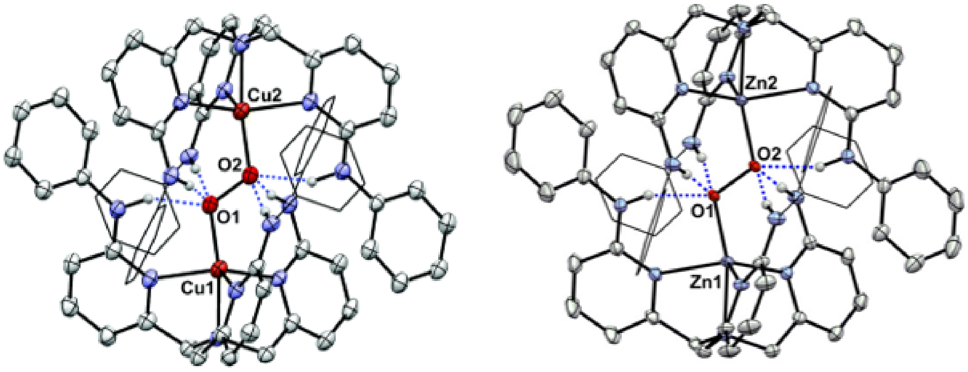

Figure 1.2 Dicopper- and dizinc 1,2-peroxo complexes stabilized by L^H, with directed H-bonds the bridging O_2 unit.

1.2 Activation of small molecules: O_2 and $^-NO_2$

1.2.1 Activation of O_2

Capture and activation of dioxygen by metalloenzymes is necessary to perform O_2 reduction and substrate oxidation reactions in Nature. There are several classes of enzymes that can activate dioxygen, including cytochromes,[48] mono- and dioxygenases,[49] peroxidase, and oxidases,[48] and different transition metals are used for activation and subsequent reactions. Heme active sites typically incorporate iron and manganese,[11, 50] while non-heme enzymes can incorporate iron, manganese, and nickel,[11, 51-52] and multiple enzyme classes are dependent upon copper for reactivity (e.g. blue copper proteins, copper superoxide dismutase).[53-54] Substrates for these enzymes vary widely but reactions include alkane and alkene hydroxylation and oxidation (*via* C-H or C=C activation or O-atom insertion). [26, 55-59]

Reduction of dioxygen can occur *via* either a 4 or 2 electron pathway. The direct 4 electron route results in the formation of water (with addition of 4 H^+), while the indirect 2 electron pathway proceeds *via* a peroxide intermediate.[60] Coordination of O_2 to metal active sites lowers the energy requirement for this reduction (for O_2, $E° = +1.23$ V vs SHE in H_2O) and provides an environment rich in proton-containing residues. The mechanism for mononuclear transition metal mediated activation of O_2 has proposed to go through several high valent intermediates.[13, 61] Dioxygen binds as a superoxide ligand (end- or side-on), concomitant with oxidation by one electron of the metal center. Such superoxo species can react with another unit of the active metal site to form a dimetal-peroxo species, or it can form a hydroperoxo species by sequestering a H-atom from the surrounding environment. This is followed by homolytic cleavage of the O–O bond and oxidation of the metal center to yield a high-valent M-oxo species. This high valent oxo can be reduced by abstracting hydrogen atoms from the substrate in one or two steps to form a M-OH or M-OH_2. The high valent intermediates and their derivatives (peroxo, hydro- and alkyl-peroxo, oxo, and various bridging derivatives) have been implicated as the active species in substrate oxidation and hydroxylation, with different product distribution suggesting different active species.[11, 13, 62]

Studying these small molecule reactions in their native enzyme structures presents several difficulties. The inability to easily modify primary and secondary residues, interactions with other portions of the protein ternary structure, and difficulties in collecting spectroscopic characterization data have pushed for the development of model systems.[3] Model complexes for a variety of oxygen activation enzymes[52] have been developed over the years (Fig. 1.3), varying in ligand class (heme and non-heme),[11] denticity (tri-, tetra-, and pentadentate),[58, 63-67] and in secondary coordination environments (i.e., steric bulk and/or H-bond donors or acceptors).[68-69] Heme-dioxygen chemistry dates back to the original discovery of hemoglobin; modern work has expanded to investigate incorporation of secondary sphere Lewis acids in the form of other metals for the formation of binuclear complexes[70-72] and the addition of multiple appended H-bond donors to the primary sphere ligands for stabilization of the intermediates. Models of copper-containing enzymes represent a wide swath of literature for activation of O_2 by Cu^I complexes to access elusive high-valent Cu-oxygen intermediates, as well as trapping the intermediates of O_2 activation using di-copper systems.

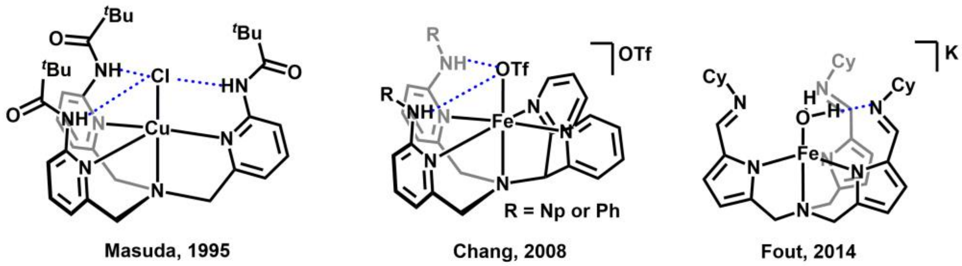

Masuda, 1995 Chang, 2008 Fout, 2014

Figure 1.3 Examples of transition metal complexes with a range of secondary sphere H-bonding moieties.

Non-heme model complexes make up a significant portion of the O_2 activation literature. The relative ease of synthesis of ligands for these complexes makes them attractive targets. With increasing literature on iron containing non-heme active sites in lipoxygenase,[24, 73-74] mono- and dioxygenase enzymes,[49, 75-77] models with similar structure or function are of great importance to help understand the requirements for the mechanisms of O_2 activation and incorporation into substrates.[78] In the mid-90s, the Que and Masuda groups began working with the TPA ligand and several of its derivatives to study the intermediates of O_2 activation. Lim et al demonstrated the oxidation of Fe^{II}TPA by *m*-chloroperbenzoic and peracetic acids and observed an intermediate which was capable of oxidizing thioanisole to the corresponding sulfoxide, as well as oxidizing cyclooctene to the epoxide.[79] Both of these substrate oxidations, along with supporting ESI-MS and Mössbauer spectra, confirm the active high valent intermediate they observed is a high valent Fe^{IV}-oxo. The Masuda group, using a TPA derivative featuring secondary sphere neopentylamino H-bonding groups, synthesized an Fe^{III}-OH complex as a model for the active site of lipoxygenase.[24]

In a report in *Science* in 2000, the Borovik group reported the first Fe^{III}-oxo derived from O_2 activation by an Fe^{II} species.[13] The reaction was proposed to proceed through a high valent Fe^{IV}-oxo intermediate to form an Fe^{III}-oxo complex. This was confirmed by ^{18}O labeling studies and IR spectroscopy. The authors propose O_2 activation occurs through bridging diiron peroxo intermediate followed by O–O bond cleavage to form the Fe^{IV}-oxo, which undergoes HAT from solvent or dihydroanthracene (DHA) to form the Fe^{III}-OH species. From there, intramolecular proton transfer to the basic ligand results in the formation of the Fe^{III}-oxo (Fig. 1.4). The lack of a bridging Fe^{III}-O-Fe^{III} species is thought to be due to the fact that the oxo ligand is buried within the steric bulk of the H-bonding ligand. Crystal structure bond lengths, *ab initio* calculations, and Mössbauer spectroscopy support proposed formulation of an Fe^{III}-oxo species. There have been numerous follow-up studies modifying this H_3buea ligand scaffold and its derivatives for activation of O_2 and capture of the terminal products of the reduction. Modifications include varying the number of H-bonding arms,[32, 80] the transition metal used,[36, 81-82] switching to H-bond acceptors,[35, 81, 83] incorporation of outer sphere Lewis acids[83] – all in an effort to characterize and/or capture the intermediates of O_2 activation, and to demonstrate the effects that ligand coordination environments have on the coordination of oxo ligands and subsequent reactivity of the metal complexes.[84]

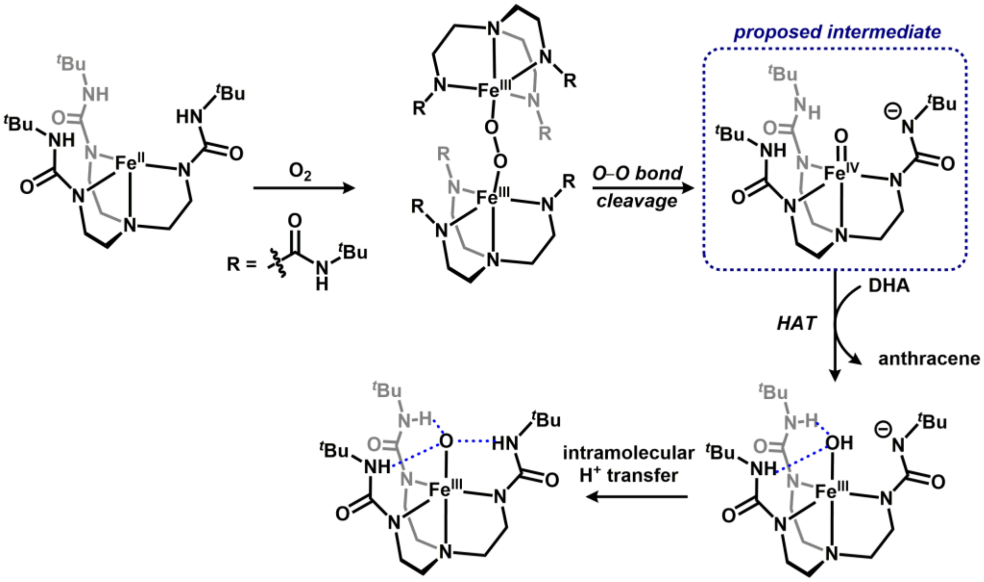

Figure 1.4 Mechanism of O_2 capture, activation, and stabilization by a synthetic non-heme iron complex, Fe(H_3buea).

Identification of the more elusive intermediates of O_2 activation with iron (see: superoxo and peroxo species) remains a challenge.[62, 76, 85-87] Examples of alkyl-[88] and hydroperoxide[27, 89-90] complexes have been characterized and the reactivity and mechanism for substrate oxidation and hydroxylation have been studied extensively,[56, 90-97] particularly in diiron systems.[71, 87, 98-99] The Que group reported on the first evidence of a Fe-superoxo complex (Fig. 1.5), which was formed from the addition of O_2 to a $[Fe_2(\mu\text{-}OH)(6\text{-}Me_3TPA)_2]^{2+}$ dimer complex.[87] Resonance Raman data support a diiron-superoxo species (νO–O: 1,310 cm^{-1}), which is active for proton coupled electron transfer from di-*tert*-butylphenol *via* O-H cleavage.

Figure 1.5 Capture of O_2 at Fe^{II}TPA and observation of a superoxo intermediate.

More recent work continues to work toward capture of the intermediates of dioxygen activation. To enable monomeric complexes similar to the Borovik Fe^{III}-oxo species, incorporation of sterically bulky and/or hydrogen bonding groups has been utilized by several groups. The Fout group has demonstrated facile reduction of O_2 using Fe^{II} complexes featuring their tautomerizing H-bonding complex.[40] Similar to the Borovik group, they have been able to isolate and characterize an Fe^{III}-oxo as well as Fe^{III}-OH and $Fe_2^{III}(\mu\text{-}O)$ dimers as the terminal products of O_2 activation. Electrochemical studies supported the formation of an Fe^{IV}-oxo intermediate that rapidly abstracts an H-atom to form the terminal Fe^{III}-OH species. Work in the Anderson group has used cobalt[100-101] and nickel[102] species on bulky anionic tridentate ligands to isolate high valent species related to O_2 activation. A series of high valent cobalt-oxo complexes represent an unusual example of a d^6 oxo species; reactivity studies demonstrate its ease in activating C-H bonds with BDE up to 85 kcal/mol, however this species is not derived directly from O_2.[100, 103] The nickel superoxo complex undergoes a ligand oxidation and could be induced to release O_2 upon addition of silver triflate, but is unreactive for HAT. Oxygen atom transfer (OAT) reactions, however, were successful; the unusual reactivity here suggests the redox active ligand plays a role in the reactivity of the superoxo ligand.

Recent work by Goldberg and coworkers has demonstrated a series of sulfur or oxygen containing ligands metaled with Fe^{II}, which are active for O_2 activation. Multiple intermediates of O_2 activation, including a diiron 1,2-peroxo, an Fe^{IV}-oxo and a terminal Fe^{III}-OH, were spectroscopically characterized.[104] In a mixed N, S ligand framework with H-bonds, they also demonstrated hydroxyl radical rebound from O_2 activation, although the high valent intermediates could not be observed, even at low temperature.[105] Our group has been successful in using sterically bulky trifurcated H-bond donor ligands (L^R) to capture and characterize dicopper and dizinc 1,2-peroxo intermediates of O_2 reduction.[18, 22] The dicopper species can then proceed through the O–O bond cleavage to yield a Cu^{II} species. These examples demonstrate the utility of sterically bulky groups and H-bonds for the formation of monomeric iron-oxygen species and helps us frame our own studies of dioxygen activation.

1.2.2 Activation of $^-NO_2$

The reduction of nitrogen-containing small molecules *via* denitrification constitutes a significant portion of the larger global nitrogen cycle.[106] The individual steps of denitrification involve reduction of nitrate to nitrite, followed by nitrite reduction to nitric oxide, which can be converted back to dinitrogen through subsequent reactions. In working to improve catalytic systems for the reduction of nitrogenous intermediates back to N_2, it is critical to understand the requirements that allow biological systems to readily perform these reactions. It is also worth noting that denitrification proceeds through nitric and nitrous oxides, both of which are considered greenhouse gases, so efforts to transform these molecules by reversing denitrification to access the more useful and safer nitrogen source, ammonia, are of broad interest to the global community.

Nitrite reductase enzymes (NiRs) typically rely on iron or copper as the transition metal in the active site.[107] Iron-based NiRs feature low-spin heme structures and can readily bind π-acids. The secondary sphere of these porphyrin systems incorporates multiple H-bonding groups from surrounding amino acid residues, which are proposed to participate in proton shuttling for the reduction of $^{-}NO_2$ while it's bound to the iron active site (Fig. 1.6).[108-109] Copper containing enzymes (CuNiRs) feature two copper sites within the larger subunit – one site (type 1) is similar to other reported blue copper centers, while the second site (type 2), is bound by three histidine ligands and serves as the binding site for nitrite reduction. The type 1 Cu is proposed to be used for electron transfer to type 2 Cu.[110]

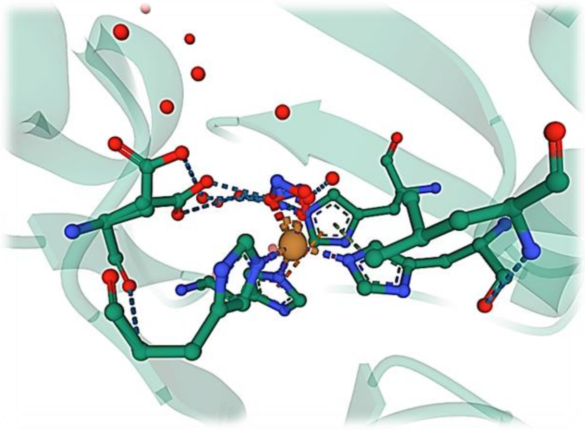

Figure 1.6 Active site of CuNiR (E. coli) with $^{-}NO_2$ bound to Cu; secondary sphere interactions with Asp and H_2O are visible. PDB 516K.

Early work proposed a mechanism for reduction of $^{-}NO_2$ at copper that proceeds from a Cu^{II}-H_2O resting state through a Cu^{II}-NO_2 species, followed by proton transfer with loss of water to form a Cu^{I}-NO^{+} species, which decays to form a Cu^{II}-NO• before loss of NO (g). Later work suggested the Cu^{II}-NO• intermediate was in fact a Cu^{I}-NO+ intermediate following an electron transfer step before loss of NO (g).[107, 110] Secondary sphere amino acid residues are proposed to help position and rearrange the $^-NO_2$ during this process, as well as provide the protons necessary for the transformation. These mechanisms are still under investigation, as results from different spectroscopic and crystallographic experiments give conflicting information, especially regarding the Cu^I-NO species, and are often hindered by the difficulty of analyzing the intermediates in the larger protein structure.[107] Thus, turning to synthetic systems to act as models can help to understand the mechanism of $^-NO_2$ reduction in CuNiRs.

Model complexes for CuNiRs span a wide range of ligand styles, although most incorporate at least two nitrogen arms, and both neutral and ionic ligands have been used. Both Cu^I and Cu^{II} have been used as the active metal in studies of $^-NO_2$ reduction, in part because redox states have been invoked in the CuNiR mechanism. Work from the Lehnert group has demonstrated several iterations of Cu-NO_2 reduction. The use of a monoanionic tris(triazolyl)borate ligand to support Cu^I-NO_2 represented the first functional mimic of CuNiR, with near quantitative yields of NO (g) produced upon addition of H^+.[111] Work performed around the same time by the Hsu group also utilized a monoanionic scorpionate ligand for synthesis of a Cu^I-NO_2 complex. Their direct comparison to a neutral isomer helped demonstrate different mechanistic pathways for the neutral vs. charged Cu^I species: specifically, the neutral Cu^I-NO_2 is directly protonated and releases NO (g), while the charged Cu^I-NO_2 could capture the NO at Cu before release.[112] This mechanistic difference has potentially significant ramifications on other nitrite reduction experiments when starting from different redox states.

Other groups have demonstrated the interplay of redox states for the reduction of $^-NO_2$ at copper. The Lehnert group reported the synthesis of Cu^{II}-NO_2 complexes, which could be electrochemically reduced in aqueous media to produce NO (g). A series of ligands were tested in this study, and were able to tune the reduction potential to achieve high $^-NO_2$ and low O_2

reduction.[113] The Symes group showed that $^{-}NO_2$ could be electrocatalytically reduced at Cu^{I} *via* PCET assisted by a secondary sphere group capable of proton shuttling (Fig. 1.7).[114]

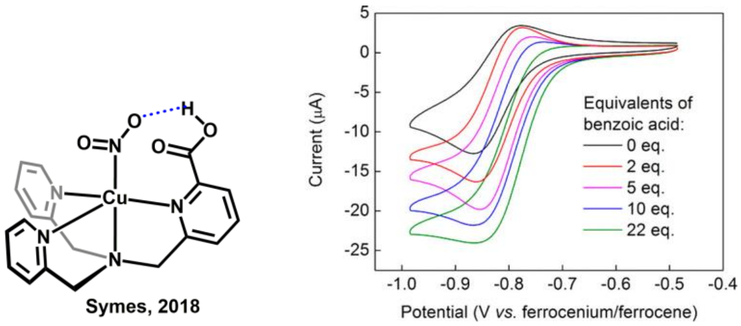

Figure 1.7 Copper(I) complex with secondary sphere carboxylic acid residue capable of performing electrocatalytic nitrite reduction in the presences of benzoic acid (left); cyclic voltammograms showing catalytic wave of $^{-}NO_2$ reduction in the presence of increasing equivalents of benzoic acid (right, CV figure from ref. 112).

Recent work has demonstrated differences in reactivity of Cu-NO_2 complexes based on the binding mode of $^{-}NO_2$. While computational work has shown that the κ^1-N and κ^2-O,O isomers are nearly isoenergetic, their subsequent reactivity can be effected. The Patra group synthesized a model system for CuNiR which was capable of undergoing a $^{-}NO_2$ binding mode conversion from κ^2-O,O to κ^1-N upon reduction from Cu^{II} to Cu^{I}. Formation of NO (g) is proposed to come from a formal Cu^{II}-NO• species in this system, formed after the addition of H^+ and in equilibrium with Cu^{I}-NO^+.[115] Work from the Warren group demonstrated that a Cu^{I}-NO_2 (κ^1-N) was incapable of performing OAT to PPh_3, while the analogous Cu^{II}-NO_2 (κ^2-O,O) complex formed O=PPh_3 in near quantitative yield.[116] Work in our group has calculated that the Cu^{I} κ^1-N, κ^1-O, and κ^2-O,O isomers are nearly isoenergetic, and the coordination of O-NO in a κ^1-O fashion enables facile reduction and release of NO (g), although the intermediates of $^{-}NO_2$ binding prior to reduction have not been identified in this reaction.[117]

1.3 Low-valent metals and hydrogen bonds

1.3.1 Low-valent metals for small molecule activation

Low valent transition metal complexes have been implicated in a multitude of small molecule activations both in biological systems and in synthetic catalytic processes. In biological systems, low valent nickel and iron sites are implicated in the mechanism of hydrogenase,[118-119] carbon monoxide dehydrogenase,[120] and methyl coenzyme M reductase enzymes.[121] Copper(I) and nickel(I) have both been proposed redox states for activation of dioxygen and nitrite.[122-123] These and other transition metals are also used broadly for small molecule activation by a variety of mechanisms.[124-127] These mechanisms can proceed by two or one electron pathways, sometimes interchangeably, and depend both on the substrate and the nature of the metal used in the reaction. Activation and functionalization of C-H bonds by oxidation or insertion reactions make up a significant portion of the reactivity observed in first row transition metal- mediated biochemical reactions (see section above).

In enzymes, low valent metal sites ($< M^{2+}$) are less common than mid- to high-valent active sites, but spectroscopic and crystallographic data suggest that reduced metal centers contribute to important biological transformations. In hydrogenase enzymes, standard [NiFe] clusters can undergo a reduction to access mixed valent active species with relatively low reduction potentials (up to -0.5 V vs NHE), which can then react with protons to form bridging hydrides between nickel and iron.[128-130] Nitrogenase enzymes incorporate multi-nuclear iron clusters which can carry additional electron density, effectively lowering the redox potential of the active site to potentials as negative as -0.6 V vs SHE (Fig. 1.8).[2] In carbon monoxide dehydrogenase/acetyl CoA synthase, reduced nickel active sites enable binding of and reduction of CO_2 due to increased electron density, and increased backdonation into the empty orbitals of CO enables binding and subsequent activation.[131-132] Copper(I) active sites are found in blue copper proteins and exhibit relatively oxidizing potentials in comparison to other M^{+1} active sites.[133] The wide variety of reactivity that stems from these low valent active sites (CO coordination, N_2 activation, H_2 formation) indicates their important role and the necessity for further study through model complexes.

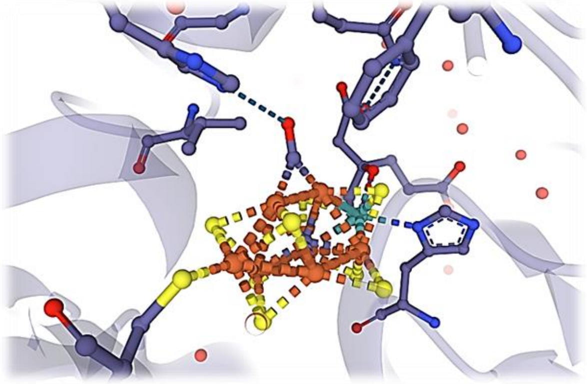

Figure 1.8 Carbon monoxide bound to the FeMo cofactor of nitrogenase (A. vinelandii), with H-bonds from a secondary sphere His interacting with the CO ligand. PDB 4TKV.

In synthetic chemistry, accessing low valent oxidation states enables activation of a wide variety of chemical bonds through one and two electron pathways. In organometallic catalysis, oxidative addition and reductive elimination steps can proceed *via* M^0 or M^I active catalyst *via* two electron transfer mechanisms.[134] Photoredox catalysis can proceed through one or two electron pathways, and numerous transformations can be induced by single electron transfers (SETs).[135-136] Often, the path for one or two electron chemistry is dictated by the transition metal: Pt and Pd typically function by two electron routes, while Ru and Ir can access both two and one electron paths.[137-138] First row transition metals are typically capable of switching from one to two electron mechanisms and are dependent on the conditions and substrates present in the reaction. Iron(II) species can perform two electron transfer reactions when in oxidation conditions, but intermediate iron(III) species accessed by SET are also active for similar reactivity.[139-140] Often, product distribution can help to distinguish between the two routes for reactivity. In nickel catalysis, toggling between Ni^{II}/Ni^{IV} and Ni^{I}/Ni^{III} reactions can be affected by substrates and reaction conditions, and switching from Pd to Ni catalysts enables access to the intermediate Ni^{I} species that are inaccessible with Pd^{0}/Pd^{II} chemistry.[134, 141] This opens up a wider range of chemical reactions that can be performed, including model reactions for enzyme active sites.

1.3.2 Incompatibility of low valent metals and hydrogen bonds

Due to the negative reduction potentials of low-valent transition metals, H-bonding moieties are typically incompatible with such species.[142-145] At the same time, protein crystal structures of methyl coenzyme M reductase,[146] nitrogenase,[147-148] and even hydrogenase[7, 149] invoke secondary sphere amino acid residues that contribute H-bonds to the active site at the reduced metal center.[2] This has been achieved through isolation of the active site, engaging substrates which intercept H-bonding interactions, using well-defined H^+/e^- transport methods, and functioning above the proton reduction potential ($E° > -0.8$ V vs SHE).[6] These combined efforts enable low valent metals to function in enzymes laden with proton-containing amino acid residues and water molecules.

However, the incorporation of H-bonding groups into synthetic systems with low valent metal centers remains a significant challenge. Prior work has demonstrated that multiple examples of ligand deprotonation with concomitant metal hydride formation. Milstein's tautomerizing catalysts are an excellent example of ligand deprotonation and subsequent hydrogenation when acidic H-bond containing residues are in the presence of lower-valent transition metals. Other work has demonstrated general reactivity of H-bond donors with low valent metal species, resulting in protonation of the ligand rather than the substrate (see examples from Mock and Peters) or deprotonation, rather than formation of H-bonding adducts.[143-145, 150] Work in our group has begun to address this issue with the use of reductively stable appended $-CF_2H$ moieties that are capable of forming weak H-bonding interactions while avoiding deprotonation or deleterious reactivity with the metal. [47] Other work in our group has shown that a low valent Fe^0-N_2 compound could form stable adducts with certain Lewis acids but with Brønsted acids was rapidly protonated. Redesign of the system and tuning the redox potential by utilizing a slightly more oxidizing Re^I-N_2 complex enabled isolation of a stable H-bonding adduct with exogenous acids (Fig. 1.9).[145, 151]

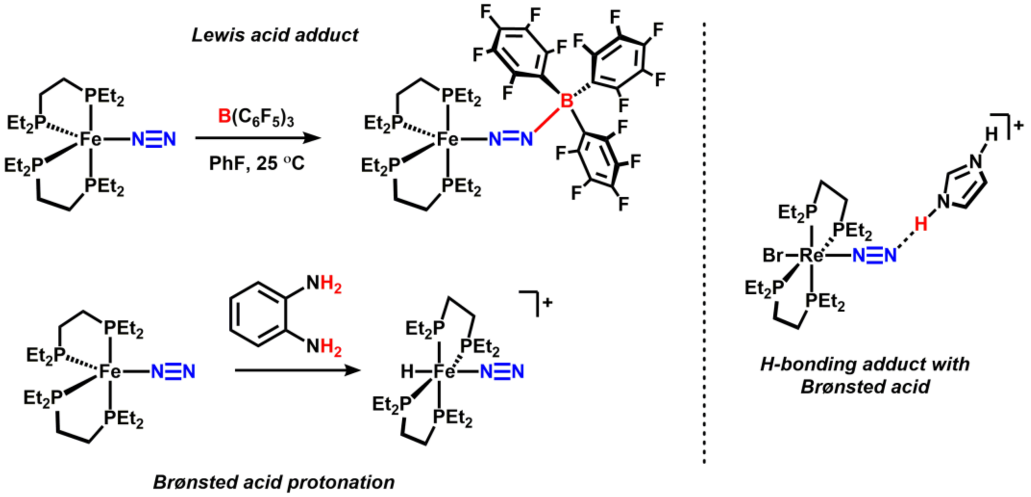

Figure 1.9 Low-valent complex interactions with Lewis and Brønsted acids; Fe^0-N_2 is protonated, while Re^I-N_2 forms a stable adduct.

1.4 Outline and scope of thesis

While prior work has shown the importance of secondary sphere hydrogen bonding for substrate capture and activation, use of a single ligand platform for both low and high-valent transition metal complexes stabilized by transition metals is unusual, especially considering the similarities of amino acid residues within metalloenzyme metal active sites which can access low or high valent states, depending on the enzyme. Our goal has been to develop synthetic complexes which can model the effects of H-bonding like those found in enzyme active site; this includes the synthesis of the ligand platform, L^R, for the purpose of accessing tunable secondary sphere H-bond donors. Efforts to demonstrate the robustness of the ligand platform L^H for stabilization of the products of small molecule activation at different oxidation states across multiple transition metals, as well as the influence of the H-bonding on the reactivity of these complexes will be described. The reductive stability of the L^H ligand is introduced in Chapter 2, in which we establish that the H-bonds are crucial for stabilizing a series of low valent nickel(I) complexes. The stability of the complex enabled its isolation and solid state characterization, and also allowed us to investigate reactivity of the complexes for fluoride abstraction. In Chapter 3, we examine how secondary sphere H-bonding enables us to observe the intermediates of dioxygen activation at iron(II). The terminal product of this reaction is capable of performing hydroxyl radical rebound at higher conversions than a related complex without H-bonds. The activation of O_2 is a direct result of the H-bonds in the Fe^{II} precursor, which we attribute to the kinetic stabilization of the intermediates of O_2 reduction. Finally, in Chapter 4, the synthesis of copper(I) complexes with H-bonds of varying strength are used to interrogate the reduction of nitrite. Two different routes towards $^{-}NO_2$ reduction are identified, and both result in evolution of NO (g) and comparable Cu^{II} products. The aim of this thesis is to demonstrate the utility of H-bonding interactions in transition metal complexes across multiple oxidation states to stabilize intermediates of biologically relevant small molecule activation, specifically, the use of H-bonds to establish divergent reactivity from analogous complexes without secondary sphere residues (Fig. 1.10).

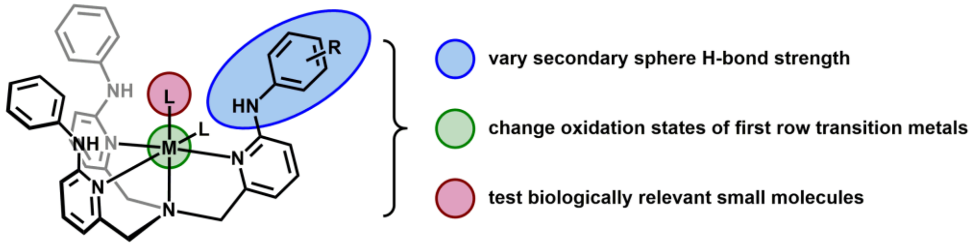

Figure 1.10 Schematics of research goals presented in Chapters 2-4.

Chapter 2 Hydrogen-bonded Nickel(I) Complexes

Portions of this chapter have been published:

Wilson, J. R., Zeller, M., and Szymczak, N. K.; Hydrogen-bonded nickel(i) complexes *Chem. Commun.*, **2021**, 57, 753-756

2.1 Introduction

Exploration into redox interconversions of nickel-based coordination complexes is motivated by relevance to both the bioinorganic[52] and organometallic fields.[134] In the latter, Ni has recently emerged as a prominent metal with catalytic applications. A key difference between Ni and its congeners (Pd and Pt) is the propensity to undergo single-rather than double-electron transfer during bond cleavage reactions, a feature that has facilitated an expansion of the available chemical transformations.[134, 152] Single electron reduction of the common Ni^{II} state affords Ni^{I} complexes, many of which react with a variety of small molecule substrates.[122, 153-154] Higher coordinate Ni^{I} complexes often feature supporting ligands that contain soft donor and/or π-acceptor groups (e.g. phosphine, CO, CN).[155]

In contrast to synthetic systems, less ligand diversity is available within the active sites of metalloenzymes, and stabilization of reduced states/substrates/intermediates is augmented by a network of secondary sphere interactions.[3] These secondary sphere interactions are critical to the function of many biological transformations including H^+/e^- interconversions,[8, 156-159] and CO_2 reduction.[160] To emulate this design principle, study, and ultimately develop synthetic analogues, complexes containing appended H-bond donors are increasingly used in biomimetic design[3, 38, 161-162] and catalytic transformations.[38, 44, 163-169] However, a key limitation in synthetic systems is the general incompatibility of H-bond donors with low valent metal complexes.[142-145] Thus, most studies are limited to mid- to high-oxidation-state transformations, and/or complexes undergo proton transfer if reduced to a low-valent state.[150, 170] One synthetic strategy to achieve reductive stability is to use weakly acidic H-bond donors that can engage with metal-coordinated substrates.[47] Such donor/acceptor interactions are straightforward to access and study using halides, the strongest acceptor of which is fluoride. Low valent late transition metal fluoride complexes are uncommon,[171] a consequence of electron pair repulsion between occupied p- and d-orbitals on fluorine and the metal, respectively.[172] This destabilizing interaction can be overcome by engaging secondary sphere H-bonds with fluoride, which alleviates the filled–filled repulsive interactions through donor/acceptor interactions. We recently demonstrated this and related principles using –EH-appended TPA based ligands (E = O, NAr),[22, 173] and in one case, the secondary coordination sphere served to capture fluoride in a molecule that would otherwise undergo dissociation.[173] Although both –NHAr and –OH groups engage in highly directed H-bonding interactions,[22, 173-174] –NHAr groups are less acidic, and thus, more stable at reduced potentials.[175] We hypothesized that reductively stable, directed H-bonds could provide necessary stabilization to isolate low valent metal complexes, including $\mathrm{Ni^{I}}$ (Fig. 2.1).

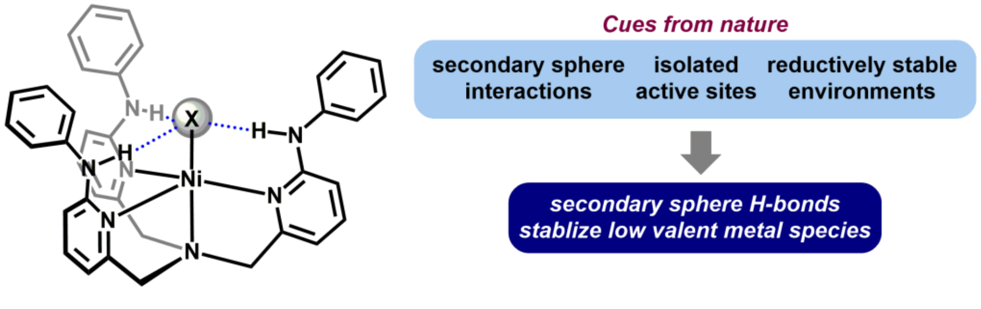

Figure 2.1 Strategy for stabilization of low valent Ni complexes with H-bonds.

2.2 Targeting Ni(II) precursors for access to Ni(I)

We targeted a series of nickel(II) halide complexes containing the tris(6-phenylamino-2-pyridylmethyl)amine ligand (L^H). NiX_2 compounds, where X = Cl or Br, were prepared by metalation of L^H with either $NiCl_2{\bullet}6H_2O$ or $NiBr_2(DME)$ in CH_3CN solvent. After 1 h, the precipitated compounds were decanted to afford $NiCl_2L^H$ and $NiBr_2L^H$ in moderate to high yields. To prepare the fluoride congener, NiF_2L^H, 2 equiv. CsF were combined with $NiCl_2L^H$, and a pale blue-green solid was isolated after 24 h. The ^1H NMR spectrum revealed broad resonances ranging from 7 to 85 ppm. The solution state structure could not be assigned due to overlapping peaks in diamagnetic region of the ^1H NMR spectrum. Structural characterization of $NiCl_2L^H$ revealed a monomeric octahedral complex. Salt metathesis of NiX_2L^H with $TlPF_6$ or $TlBAr'_4$ (BAr''_4 = tetrakis[3,5-bis(trifluoromethyl)phenyl] borate) afforded the monohalide species $[NiXL^H]^+$, $\mathbf{[1^X]^+}$.

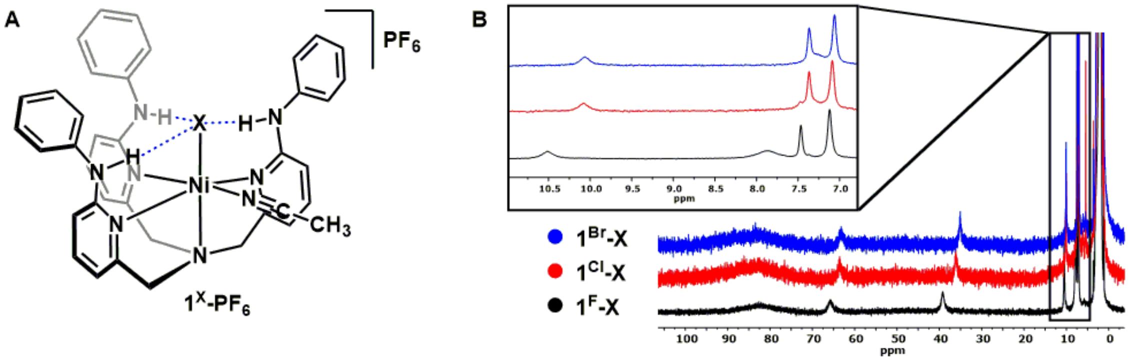

Figure 2.2 General structure of nickel(II)L^H halide complexes (A) and stacked paramagnetic ^1H NMR spectra of complexes $\mathbf{[1^X]^+}$ (B).

Complexes $\mathbf{[1^X]^+}$ were characterized by ^1H NMR and electronic absorption spectroscopy. The soluble, paramagnetic complexes exhibit C_3-symmetric ^1H NMR spectra, similar to previously characterized Ni^{II}TPA complexes (Fig. 2.2).[176-178] Although $\mathbf{1^{Br}\text{-}BAr''_4}$ and $\mathbf{1^{Cl}\text{-}BAr''_4}$ are similar (Br: 656 nm, ε = 13 cm^{-1} M^{-1}; 1075 nm, ε = 20 cm-$^1M^{-1}$; Cl: 638 nm, ε = 19 $cm^{-1}M^{-1}$, 1046 nm, ε

= 28 cm^{-1}M^{-1}), complex **1^{F}-BAr″$_4$** features bands that are shifted to higher energy (581 nm, ε = 11 cm^{-1} M^{-1}; 937 nm, ε = 15 cm^{-1}M^{-1}), consistent with higher ligand field strength.[179-180]

Across the halide series, we evaluated the structural metrics obtained from single crystals of **1^{Br}-PF$_6$**, **1^{Cl}-PF$_6$**, and **1^{F}-PF$_6$**. All three complexes exhibit octahedral geometry, with a coordinated CH_3CN molecule. In all cases, the halide engages in trifurcated H-bonding interactions to the appended aniline –NH groups, with average N–X distances decreasing from –Br to –F (Br = 3.271 Å, Cl = 3.159 Å, F = 2.731 Å). These results are consistent with moderate H-bond strength and increasing H-bond accepting ability across the halide series, Br > Cl > F.[181] Of note, complexes **1^{Br}-PF$_6$** and **1^{Cl}-PF$_6$** crystallize in the same space group (*P*21/c) and are isomorphous, in contrast to **1^{F}-PF$_6$** (Pbca) (Fig. 2.3). The similarities between **1^{Br}-PF$_6$** and **1^{Cl}-PF$_6$** may be a composite of H-bonding as well as crystal packing forces, which we note can have similar strengths.[182]

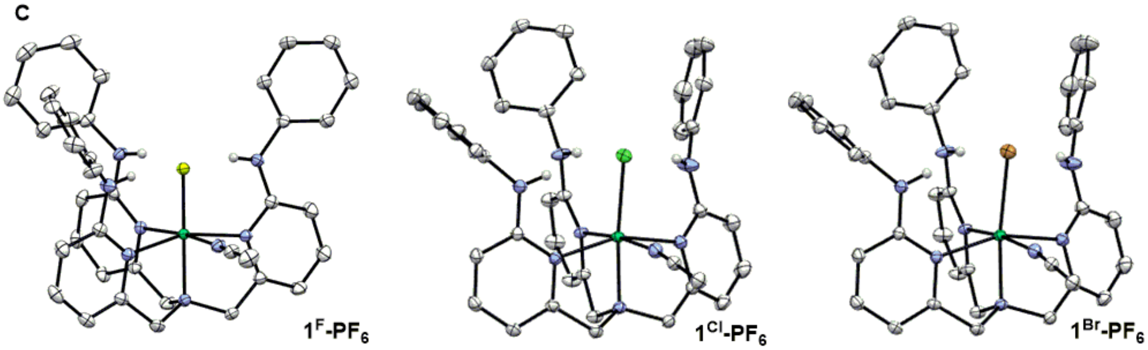

Figure 2.3 Crystal structures of nickel(II) complexes.

We interrogated H-bonding interactions in **$[1^{X}]^+$** by examining the NH stretching frequencies in the infrared spectra.[183] For the strongest acceptor, fluoride, we observed a shift in the ν_{NH} from 3400 cm^{-1} to 3250 cm^{-1} for L^{H} and **1^{F}-BAr″$_4$**, respectively, consistent with an H-bond interaction between –NH and the Ni–F (for ν_{NH} assignment, see Fig. 2.4).[22] Across the halide series, νNH decreases as F > Cl > Br, which is opposite from their respective acceptor abilities. We attribute this feature to distortions from planarity of the aniline N atoms as the halide size.[184] Although **[1^{X}]$^{+}$** exhibit octahedral solid-state structures, room temperature ^{1}H NMR spectroscopy experiments indicated *C*$_3$-symmetry. The spectra of **1^{Cl}-PF$_6$** and **1^{Br}-PF$_6$** are nearly identical, in contrast to **1^{F}-PF$_6$**, which exhibits resonances that are shifted downfield (see Fig. 2.2). To assess the role(s) of fluxional exchange processes on the solution structure, we performed a variable temperature ^{1}H NMR experiment. When a THF solution of **1^{F}-PF$_6$** was cooled to -75 °C, additional resonances appeared (30–70 ppm). Similar resonances were observed at room temperature by adding 1 equiv. of a strongly coordinating ligand, N,N-dimethylaminopyridine. Collectively, these results are consistent with a dynamic ligand association in solution, in which the 5-coordinate Ni^{II} species coordinates a sixth ligand, which imparts a geometrical change from *C*$_3$-symmetry to octahedral geometry: the latter geometry is common in related Ni^{II}TPA complexes.[185-186] In contrast to the ~100 structurally reported Ni^{II}TPA (or TPA-related) complexes, there are no structurally characterized low valent variants.[187] To our knowledge, the only report of a Ni^{I}TPA complex forms from [(Ni(Me$_2$–TPA)(H))$_2$]$^{2+}$, which was not characterized in the solid state.[177] We employed cyclic voltammetry experiments to assess the accessibility of a reduced Ni^{I} state. The free ligand, L^{H}, is reductively stable up to 3 V (glassy carbon vs. Fc^{+}/Fc; 0.1 M [NBu$_4$][OTf] in CH$_3$CN).

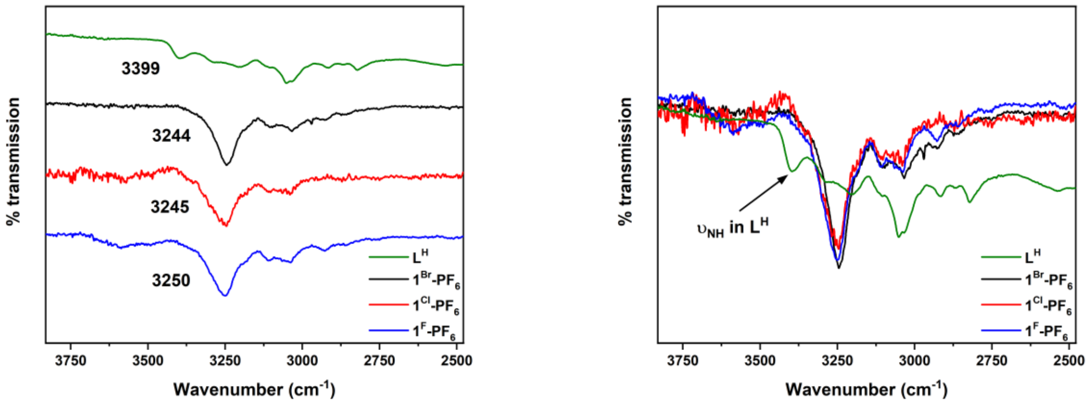

Figure 2.4 Overlay of IR spectra of L^{H} and **1^{X}-PF$_6$** complexes, comparing $\nu_{N\text{-}H}$.

Complexes **1$^{\mathbf{X}}$-BAr″$_{\mathbf{4}}$** exhibit a reversible reduction event at $E_{1/2}$ = -1.81 V, -1.56 V and -1.48 V for **1$^{\mathbf{F}}$-BAr′**$_4$, **1$^{\mathbf{Cl}}$-BAr″**$_4$, and **1Br-BAr′$_{\mathbf{4}}$**, respectively (Fig. 2.5).

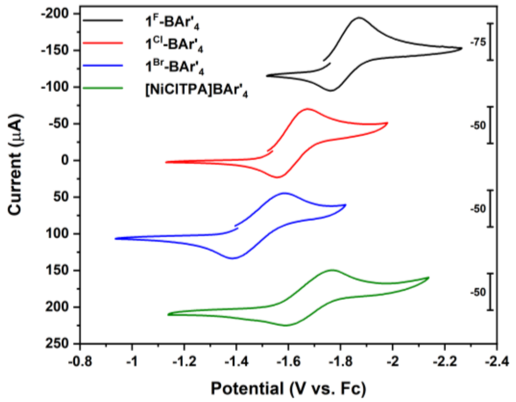

Figure 2.5 Electrochemical analysis of **1$^{\mathbf{X}}$-BAr'$_{\mathbf{4}}$** and [NiClTPA]BAr″$_4$ recorded in CH_3CN with 0.1 M [Bu_4N][OTf].

2.3 Hydrogen bonding to low valent Ni(I)

Chemical reduction of **1$^{\mathbf{F}}$-PF$_{\mathbf{6}}$** with potassium graphite (KC_8) in THF at -78 °C immediately formed a dark blue-green complex (**2$^{\mathbf{F}}$**). Reductions of **1$^{\mathbf{Cl}}$-PF$_{\mathbf{6}}$** and **1$^{\mathbf{Br}}$-PF$_{\mathbf{6}}$** proceeded similarly to afford **2$^{\mathbf{Cl}}$** (blue) and **2$^{\mathbf{Br}}$** (purple). These complexes gradually decompose in THF at room temperature (for **2$^{\mathbf{Cl}}$**, $t_{1/2}$ = 5.1 h) but are stable at lower temperatures (-35 °C). Characterization of the series of **2$^{\mathbf{X}}$** by electronic absorption spectroscopy revealed a single broad absorbance in the visible region (for **2$^{\mathbf{Cl}}$**, λ = 593 nm, ε = 1950 cm^{-1}M^{-1}; for **2$^{\mathbf{F}}$**, λ = 706 nm, ε = 1444 cm^{-1}M^{-1}; and **2Br**, λ = 550 nm, ε = 3030 cm^{-1}M^{-1}) (Fig. 2.6). An X-band EPR spectrum of **2$^{\mathbf{Cl}}$** (110 K) revealed *g* values of 2.28, 2.21, and 2.02, consistent with a d^9 Ni^{I} system,[188-190] with similar spectra for **2$^{\mathbf{F}}$** and **2$^{\mathbf{Br}}$** (Fig. 2.7). It's possible that the splitting observed in complex **2$^{\mathbf{F}}$** is due to the presence of the fluoride ligand, which could cause hyperfine coupling in the EPR spectrum.

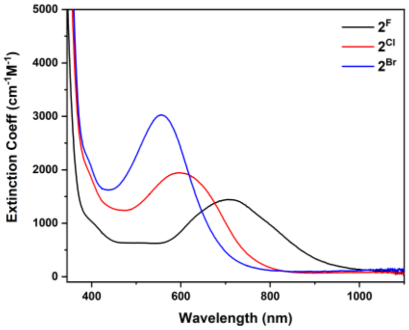

Figure 2.6 Electronic spectra of complexes $\mathbf{2^X}$ (THF, room temperature).

The solid-state structure of $\mathbf{2^F}$ (Fig. 2.8) revealed a trigonal bipyramidal geometry (τ_5= 0.94)[191] with an axial fluoride ligand. In this arrangement, the three appended –NH groups of the pendent anilines engage in moderately strong H-bonding interactions with the Ni–F (avg. N–X bond distance = 2.666 Å). We attempted to identify ν_{NH} by IR spectroscopy; unfortunately, the bands are not sufficiently resolved to include a definitive commentary on H-bonding interactions in the reduced complexes. Upon reduction of $\mathbf{1^F\text{-}PF_6}$ to $\mathbf{2^F}$, the Ni–F distance increases from 2.007(1) Å to 2.097(2) Å. We propose that elongation of the Ni–F bond imparts a higher H-bond acceptor strength, which is consistent with the shorter –NH–F contacts in $\mathbf{2^F}$, compared to $\mathbf{1^F\text{-}PF_6}$.

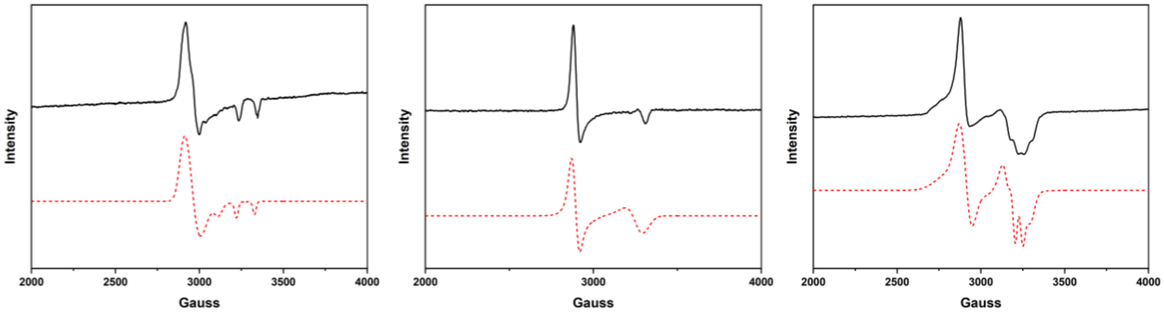

Figure 2.7 EPR spectra of complexes $\mathbf{2^F}$ (left), $\mathbf{2^{Cl}}$ (center), and $\mathbf{2^{Br}}$ (right) in toluene (110K). Experimental spectra are in black, fitted spectra in dashed red. Fitted parameters for complex $\mathbf{2^F}$: g_x = 2.270, g_y =2.240, g_z = 2.028, linewidth = 25, 25, 5 G, freq. = 9.312; $\mathbf{2^{Cl}}$: g_x = 2.020, g_y = 2.280, g_z = 2.210, linewidth = 50, 20, 90 G, freq. = 9.229; $\mathbf{2^{Br}}$: g_x = 2.055, g_y = 2.245, g_z = 2.265, linewidth = 18, 60, 60 G, freq. = 9.258 (Power: 10.28 W. Modulation: 100.00 kHz).

We acknowledge that the geometric change from octahedral to TBP can have a similar effect in the shortening of H-bonding contacts and may contribute to the change observed here. Although most reported Ni^{I} complexes contain soft donor ligands, the primary coordination sphere comprising **2^{F}** contains comparatively harder donors. Complex **2^{F}** represents a structurally rare example of a 5-coordinate Ni^{I} complex featuring halide ligands,[189, 192-193] a feature that we propose is enabled by directed H-bonding interactions. Furthermore, **2^{F}** represents the first example of a Ni^{I} complex containing secondary sphere H-bonding groups.

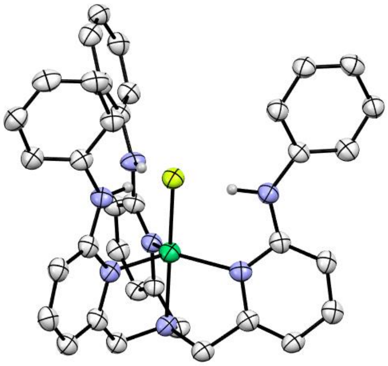

Figure 2.8 Solid state structure of **2^{F}** (50%probability ellipsoids, co-crystallized solvent molecules excluded for clarity).

Several examples of formally Ni^{I} complexes containing pyridine-based ligands are best described as Ni^{II}–L•, rather than Ni^{I}.[194-195] Wieghardt and co-workers showed that these two limiting cases can be distinguished by scrutinizing the pyridine intraligand bond distances.[196-197] The bond lengths of the pyridines in **2^{F}** and **1^{F}-PF$_6$** are normal for both C–C (**2^{F}**: 1.387(5), **1^{F}-PF$_6$**: 1.390 (3)) and C–N bonds (**2^{F}**: 1.353(5), **1^{F}-PF$_6$**: 1.56(2)), (typical values for C–C and C–N: 1.38 ± 0.1 Å and 1.35 ± 0.1 Å, respectively), which is inconsistent with pyridine-based reduction.[196] These crystallographic bond metrics, along with the EPR spectrum are consistent with a Ni-centered metalloradical (*vide supra*) for complex **2^{F}** (and by extension, **2^{Cl}** and **2^{Br}**).

Table 2.1 Selected bond lengths comparing the solid state structures of **1^F-PF_6** and **2^F**

Bond (Å)	**[NiFL^H]PF$_6$**	**NiFL^H**
NH-X (avg)	2.731	2.666
Ni-F	**2.007(1)**	**2.096(2)**
C=C (pyr, avg)	1.386	1.392

2.4 Hydrogen bonding enables reactivity for fluoride transfer

To assess the requirement of H-bonding interactions with Ni–X to isolate Ni^I complexes, we evaluated analogous syntheses using unsubstituted TPA. [NiCl(TPA)]$^+$ was prepared in quantitative yield from NiCl$_2$TPA[176] when subjected to analogous reaction conditions as for **[1Cl]$^+$** . In contrast, when conditions used to prepare NiF$_2$L^H were applied to TPA, we did not observe the formation of NiF$_2$TPA, in line with the absence of prior reports. Reduction of [NiCl(TPA)]BAr″$_4$ with KC$_8$ afforded a deep teal solution, which was characterized by ^{1}H NMR, electronic, and EPR spectroscopies. The electronic absorption spectrum features a single broad absorbance at 720 nm (ε = 4271 cm^{-1}M^{-1}). Due to the inability to isolate the reduced species, this value represents the maximum extinction coefficient, calculated from the concentration of [NiCl(TPA)]BAr′$_4$ prior to reduction. The X-band EPR spectrum (110 K) reveals *g* values of 2.10, 2.20, and 2.09. These data are similar to a prior report that analyzed an *in situ* generated Ni^I(CH$_3$CN)$_2$(Me$_2$-TPA) at low temperature (7 K).[177] Despite their spectroscopic similarities, the solution behaviors of **2^{Cl}** and NiCl(TPA) are distinct. The unsubstituted variant is prone to rapid decomposition ($t_{1/2}$ = 0.3 h at 25 °C) in comparison to **2^{Cl}** ($t_{1/2}$ = 5.1 h, Fig. 2.9). These data indicate large differences in stability (**2^{Cl}** is ~15× more stable than NiCl(TPA)), a feature that we propose is due to halide H-bonding interactions present in **2^{Cl}**.

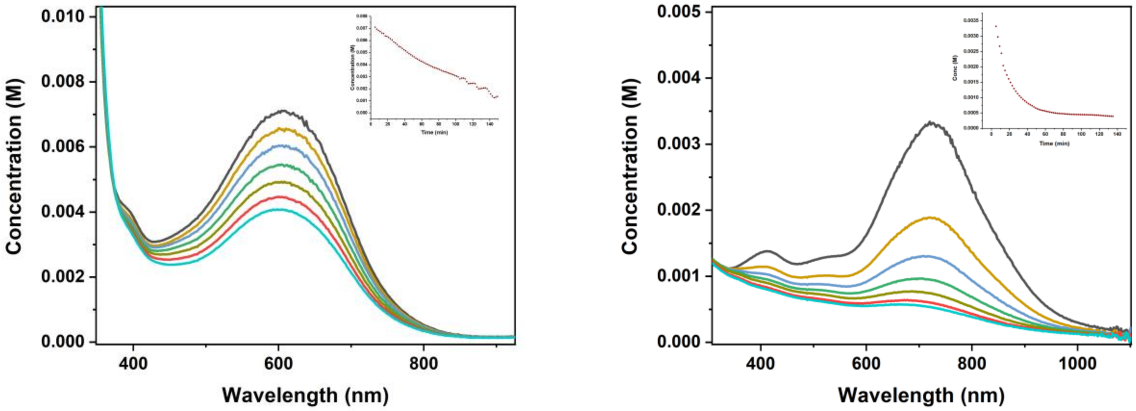

Figure 2.9 Kinetic traces of room temperature half-life of **2**$^{\mathbf{Cl}}$ (left) and NiClTPA (right) in THF (insets show decomposition of λ_{max}).

Given the high affinity of halides to engage in H-bonding interactions to the pendent aniline groups, we sought to investigate dehalogenation reactivity induced by the strongest H-bond acceptor, fluoride. We accessed defluorination reactions using a putative halide-free **[2]**$^{+}$ by adding $TlBAr''_4$ to a solution of **2**$^{\mathbf{Br}}$ at 78 °C, followed by $NaBF_4$. We observed **[1**$^{\mathbf{F}}$**]**$^{+}$ as the only NMR active species. Directed H-bonding interactions to fluoride have been shown to induce E–F bond cleavage from B–F [198] and C–F[199] moieties. The favorability of such reactions may be predicted using fluoride ion affinity values (FIAs). Since fluoride abstraction from BF_4 (FIA of BF_3 = 82.7 kcal/mol^{-1})[200] occurs readily in this system, the FIA value provides insight into the fluorophilicity of the H-bonding pocket of fluoride-free **[1]**$^{2+}$. In contrast to $NaBF_4$, $NaSbF_6$ did not form **[1**$^{\mathbf{F}}$**]**$^{+}$, consistent with a higher fluorophilicity of SbF_5 (118.5 kcal/mol^{-1}) than fluoride-free **[1]**$^{2+}$.

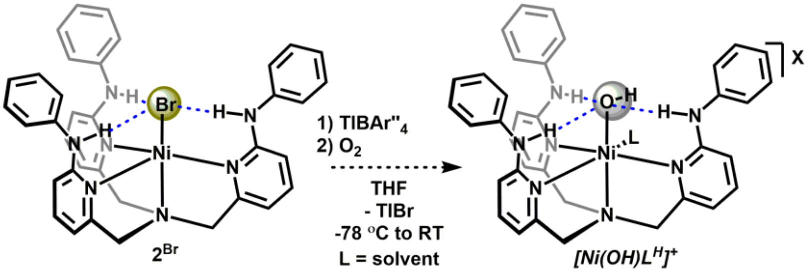

Figure 2.10 Reaction of $\mathbf{2^{Br}}$ with E–F substrates to form $\mathbf{1^F}$**-BAr″**$_4$. Analogous reactions were performed using NiClTPA.

Finally, we evaluated defluorination reactions with organic substrates containing N–F bonds. Using the protocol described above with both neutral N-fluorosulfonimide (BDE = 63.4 kcal/mol^{-1})[201] and ionic 1-fluoro-2,4,6-trimethylpyridnium triflate (BDE = 77.8 kcal/mol^{-1})[202] (see Fig. 2.10), we observed exclusive formation of $\mathbf{[1^F]^+}$.[203] In contrast, reactions using NiCl(TPA) afforded multiple species. The disparate reactivity of otherwise identical complexes containing distinct secondary coordination sphere environments highlights the reactivity controlling role of H-bonding interactions and fluoride ion affinity to bias a defluorination reaction.

We further investigated this route for activation of strong C-F bonds (BDE > 100 kcal/mol). Unfortunately, no C-F bond cleavage reactions were observed for any of the substrates tested. We hypothesize this could be due to two different issues – the geometry/steric bulk of the substrate does not allow for optimal position of the C-F bond within the H-bonding pocket for SET to occur, and/or the C-F BDE is simply too large for the Ni^I complex to access.

2.5 Early investigations of dioxygen activation from Ni^I

This dehalogenation experiment encouraged us to consider this as a route to access activation of dioxygen *via* nickel(I). Both Ni^I and Ni^{II} species as precursors for oxidation using O$_2$ have been reported, with recent examples demonstrating side-on nickel-peroxo complexes that can undergo oxygen atom transfer (OAT) reactions. Inspired by our group's previous work with dimetal-peroxo complexes incorporating L^H for stabilization of the peroxo intermediate of O$_2$

activation, we set out to demonstrate dioxygen coordination to Ni^{I}. Dehalogenation of $\mathbf{2^{Br}}$ with $TlPF_6$ at low temperature followed by addition of O_2 results in the formation of multiple species, including $\mathbf{1^{F}}$, as observed in previous reactions when using $TlPF_6$. The other species we propose is the product O_2 activation. Warming to room temperature results in consumption of the O_2 activation product (Fig. 2.11). Separate synthesis of $Ni^{II}(OH)L^{H}OTf$ (**3**) and comparison to the product from the reaction of dioxygen shows that $\mathbf{2^{Br}}$ is capable of activating O_2 from the dehalogenated low valent state.

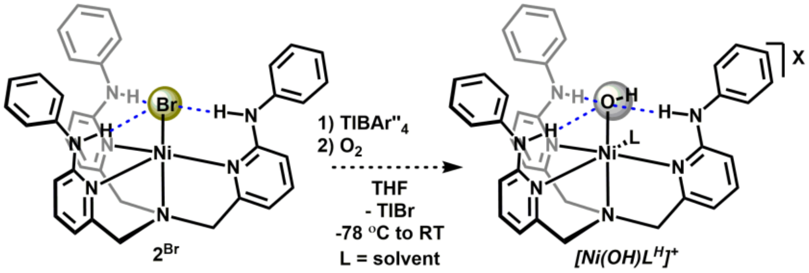

Figure 2.11 Reaction of $\mathbf{2^{Br}}$ with O_2 to form a proposed $Ni^{II}OH$ complex.

2.6 Conclusions

In summary, we prepared a series of nickel complexes featuring H-bonds to halides. These secondary sphere interactions are critical for the isolation and enhanced stability of Ni^{I} complexes, and even enable the isolation and solid state characterization of an unusual Ni^{I} species incorporating H-bonds. The H-bond interactions remain intact, even at -1.8 V (vs. Fc), showcasing the reductive stability of the appended aniline H-bond donors. The H-bond donor/acceptor interactions represent an attractive strategy wherein classically hard ligands, such as fluoride, can be rendered compatible with reduced and soft late metals. The ability to access the more reactive nickel(I) species *via* dehalogenation sets up an interesting route for capturing and activating biologically relevant small molecules, such as dioxygen.

2.7 Acknowledgments

This work was supported by the NIH (1R35GM136360-01), a Rackham Graduate Student Research Grant (J. R. W.), and the NSF (CHE-0840456, and CHE-1625543) for X-ray instrumentation. N. K. S. is a Camille Dreyfus Teacher-Scholar. We thank Dr. Jeff Kampf for X-ray assistance.

2.8 Author Contributions

All synthetic, characterization, and reactivity work was performed by J.R.W. Single crystal experimental data and structure solutions of all complexes except NiFL^{H} (**2^{F}**) were collected by M.Z. The experimental data for **2^{F}** was collected by Dr. Jeff Kampf and solved by J.R.W. The manuscript was written by J.R.W. and N.K.S.

2.9 Supporting Information

2.9.1 Experimental Details

2.9.2 General considerations

All air- and moisture-sensitive manipulations were performed using standard Schlenk techniques or in an inert atmosphere glovebox with an atmosphere of purified nitrogen. The glovebox was equipped with a cold well designed for low temperature experiments as well as a −35 °C freezer for cooling samples and crystallizations. Solvents were purified using a Glass Contour solvent purification system through percolation through a Cu catalyst, molecular sieves, and alumina. Solvents were then stored over sodium and/or molecular sieves. Deuterated solvents were purchased from Cambridge Isotope Laboratories and used as received.

Nickel dichloride hexahydrate and nickel dibromide dimethoxyethane were purchased from commercial vendors and used as received. Cesium fluoride, *N*-fluorobenzenesulfonimide (NFSI), and 1-fluoro-2,4,6-trimethylpyridinium triflate (NFTPT) were purchased from commercial vendors and dried under vacuum before transferring to a nitrogen glovebox. Ferrocene was purchased from a commercial vendor and sublimed prior to use. Potassium graphite,[204] thallium tetrakis[3,5-bis(trifluoromethyl)phenyl]borate ($TlBAr''_4$),[205] tris(6-phenylamino-2-pyridylmethyl)amine (L^H),[22] and tris(2-pyridylmethyl)amine (TPA)[206] were synthesized according to literature procedures. $NiCl_2TPA$ and $NiBr_2TPA$ were synthesized using modified procedure,[176] described below.

Caution! Sodium metal and potassium graphite are potentially pyrophoric and/or explosive materials that should be handled with caution under an inert atmosphere if possible.

NMR spectra were acquired on Varian 400 MHz, 500 MHz, or 600 MHz spectrometers as indicated below. ^1H NMR spectra are referenced to non-deuterated internal solvent residuals and are reported in parts per million (ppm) relative to tetramethylsilane. ^{19}F and ^2H NMR spectra are referenced to their respective ^1H spectra. Multiplicities are reported as follows: singlet (s), doublet (d), triplet (t), quartet (q). The spectra for paramagnetic molecules were obtained by using an acquisition time of 0.5 s, thus the peak widths reported have an error of ±2 Hz.

IR spectra were recorded on a Nicolet iS10 FT-IR spectrometer with an ATR accessory or KBr pellets as specified. Solution IR spectra were recorded on a Nicolet iS50 FT-IR spectrometer using cell equipped with KBr plates and the solvent specified below. Mass spectra were recorded on either a Bruker AutoFlex Speed MALDI-TOF in anthracene matrix or an Agilent 6230 TOF HPLC-MS with a liquid phase of 95% acetonitrile, 5% water, 0.1% formic acid. Electronic absorption spectra were recorded at ambient temperature in sealed 1 cm or 0.1 cm quartz cuvettes (as specified) with a Varian Cary-50 spectrophotometer. EPR spectra were collected on a Bruker EMX electron spin resonance spectrometer, with a Bruker 4102-ST cavity, at liquid N_2 temperatures in frozen solvent (specified below). EPR were modeled using the program WinEPR (Bruker).

Electrochemistry was performed with a Pinewave Wavenow potentiostat under a dinitrogen atmosphere with a glassy carbon working electrode, a platinum counter electrode, and a silver wire pseudo-reference electrode. Measurements were referenced against an internal ferrocene standard. Electrolyte, $[NBu_4][OTf]$, was used in 0.1 M in CH_3CN.

Single crystal data for $\mathbf{1^{F}\text{-}PF_6}$, $\mathbf{1^{Cl}\text{-}PF_6}$, $\mathbf{1^{Br}\text{-}PF_6}$, $NiCl_2L^H$, $NiCl_2TPA$, and $[NiClTPA]PF_6$ collected on a Bruker Quest diffractometer with a fixed chi angle, a Mo Kα wavelength (λ = 0.71073 Å) sealed tube fine focus X-ray tube, single crystal curved graphite incident beam monochromator and a Photon100 area detector equipped with an Oxford Cryosystems low temperature device. Examination and data collection were performed at 150 K. Data were collected, reflections were indexed and processed, and the files scaled and corrected for absorption using APEX3[207] and SADABS.[208]

Single crystal data for $\mathbf{2^F}$ were collected using a Rigaku AFC10K Saturn 944+ CCD-based X-ray diffractometer equipped with a low temperature device and a Micromax-007HF Cu-target microfocus rotating anode (λ = 1.54187 Å) operated at 1.2 kW power (40 kV, 30 mA). The data were collected using CrystalClear 2.016.[209] The X-ray intensities were measured at 85(1) K with the detector placed at a distance 42.00 mm from the crystal. A total of 2028 images were collected with an oscillation width of 1.0° in w. The exposure times were 1 sec. for the low angle images, 3 sec. for high angle. Rigaku d*trek images were exported to *CrysAlisPro* 1.171.40.53 for processing and corrected for absorption.[210] The integration of the data yielded a total of 57192 reflections to a maximum 2θ value of 138.68° of which 6999 were independent and 4293 were greater than 2σ(I). The final cell constants were based on the xyz centroids of 6999 reflections above 10σ(I). Empirical absorption correction was applied using spherical harmonics, as implemented in the SCALE3 ABSPACK scaling algorithm.

For all structures, the space groups were assigned using XPREP within the SHELXTL suite of programs[211-212] and solved by direct methods using ShelXS[107] and refined by full matrix least squares against F^2 with all reflections using Shelxl2018[213] using the graphical interface Shelxle.[214] H atoms attached to carbon atoms were positioned geometrically and constrained to ride on their parent atoms. C-H bond distances were constrained to 0.95 Å for aromatic C-H moieties, and to 0.99 and 0.98 Å for aliphatic CH_2 and CH_3 moieties, respectively. Methyl CH_3 H atoms were allowed to rotate but not to tip to best fit the experimental electron density. $U_{iso}(H)$ values were set to a multiple of $U_{eq}(C)$ with 1.5 for CH_3, NH_3^+ and OH, and 1.2 for C-H, CH_2, B-H, N-H and NH_2 units, respectively. Positions for N-bound H atoms were freely refined. For **1^F-PF_6**, $NiCl_2L^H$, and **1^{Br}-PF_6** N-H distances were restrained to a target value of 0.88(2) Å. Their $U_{iso}(H)$ values were either freely refined or set to 1.2 times $U_{eq}(N)$ (**1^F-PF_6**) or 1.5 times $U_{eq}(N)$ (**2^F**).

2.9.3 Synthesis of compounds

Synthesis of $NiBr_2L^H$: On the benchtop, a 20 mL scintillation vial was charged with $NiBr_2$(DME) (77 mg, 0.2495 mmol), L^H (152 mg, 0.2696 mmol), and 18 mL CH_3CN. The reaction was stirred for 2 hr, then precipitated with 50 mL Et_2O. The solvent was decanted off the resulting green solid, the solids washed with 10 mL Et_2O, and dried to afford a pale green powder (161.8 mg, 83% yield). MALDI-TOF of $C_{36}H_{33}Br_2N_7Ni_1$ – Br: Calc. 700.133; Found 701.814. ^1H NMR (CH_3CN, 25 °C) δ 7.06, 7.26, 7.36, 10.04, 34.92, 62.83. Selected IR data (ATR) ν = 3251, 3228, 3199, 1614, 1593, 1575, 1525, 1470, 1445, 1343, 1165, 994, 782, 747, 699 cm^{-1}.

Synthesis of $NiCl_2L^H$: On the benchtop, a 20 mL scintillation vial was charged with $NiCl_2$•$6H_2O$ (39 mg, 0.1641 mmol), L^H (100 mg, 0.1774 mmol), and 18 mL CH_3CN. The reaction was stirred for 2 hr, then precipitated with 50 mL Et_2O. The resulting green solid was decanted, washed with 10 mL Et_2O, and dried to afford a pale green powder (100.2 mg, 88% yield). Single, X-ray quality crystals were grown by diffusion of Et_2O into a DCM solution of $NiCl_2L^H$ at room temperature. MALDI-TOF of $C_{36}H_{33}Cl_2N_7Ni_1$ – Cl: Calc. 656.184; Found 655.737. ^{1}H NMR (CH_3CN, 25 °C) δ 7.12, 7.33, 9.98, 34.75. Selected IR data (ATR) ν = 3246, 3198, 3106, 3032, 1614, 1592, 1575, 1525, 1469, 1444, 1345, 1170, 995, 781, 751, 699 cm^{-1}.

Synthesis of NiF_2L^H: In the glovebox, a 20 mL scintillation vial was charged with $NiCl_2L^H$ (48 mg, 0.0692 mmol), CsF (24 mg, 0.1580 mmol), and 15 mL CH_3CN. After the reaction was stirred for 24 hr, the solution was filtered and the solvent removed, leaving a blue-green crystalline solid (44 mg, 94% yield). MALDI-TOF of $C_{36}H_{33}F_2N_7Ni_1$ – F: Calc. 640.214; Found 639.733. ^{1}H NMR (CH_3CN, 25 °C) δ 7.10, 7.44, 8.12, 11.47, 39.71, 61.17. Selected IR data (ATR) ν = 3243, 3178, 3035, 2991, 2927, 1613, 1595, 1577, 1498, 1472, 1445, 1355, 1163, 999, 773, 748, 695 cm^{-1}.

Alternate synthesis of NiF_2L^H: In the glovebox, a 20 mL scintillation vial was charged with $NiBr_2L^H$ (26 mg, 0.0332 mmol), CsF (11 mg, 0.0724 mmol), and 6 mL CH_3CN. The reaction was stirred for 48 hr, filtered, and the blue solid extracted with CH_2Cl_2 before volatiles were removed, leaving a blue-green solid (16.2 mg, 74% yield). ^{1}H NMR (CH_3CN, 25 °C) δ 7.11, 7.44, 7.83, 10.60, 38.09, 63.36.

Synthesis of $NiCl_2$TPA: On the benchtop, a 20 mL scintillation vial was charged with $NiCl_2\cdot6H_2O$ (123 mg, 0.5175 mmol), TPA (156 mg, 0.5373 mmol), and 18 mL CH_3CN. The reaction was stirred for 2.5 hr, then precipitated with 50 mL Et_2O. The solvents were decanted off the resulting bright blue solid, which was washed with 10 mL Et_2O, and dried to afford a blue powder (182.5 mg, 85% yield). Single, X-ray quality crystals were grown by diffusion of Et_2O into a CH_3CN solution of $NiCl_2$TPA at room temperature. LC-MS $C_{18}H_{18}Cl_2N_4Ni$ – 2Cl + H: Calc. 349.0963, Found 349.0988. ^{1}H NMR (CH_3CN, 25 °C) δ 13.83, 42.88, 50.19. Selected IR data (ATR) ν = 1603, 1572, 1479, 1439, 1256, 1098, 1050, 1022, 771 cm^{-1}.

Synthesis of $NiBr_2$TPA: On the benchtop, a 20 mL scintillation vial was charged with $NiBr_2$(DME) (40 mg, 0.1296 mmol), TPA (42 mg, 0.1481 mmol), and 5 mL CH_3CN. The reaction was stirred for 2.5 hr, then precipitated with 15 mL Et_2O. The solvent was decanted off the resulting bright blue solid, which was washed with Et_2O (3 x 5 mL), and dried to afford a blue solid (60 mg, 91% yield). LC-MS of $C_{18}H_{18}Br_2N_4Ni$ – 2 Br: Calc. 348.0885. Found 349.0988. ^1H NMR (CH_3CN, 25 °C) δ 14.11, 45.36, 50.97. Selected IR data (ATR) ν = 2895, 1604, 1476, 1432, 1422, 1286, 1099, 1050, 1021, 757 cm^{-1}.

Attempted synthesis of NiF_2TPA: A 20 mL scintillation vial was charged with $NiCl_2$TPA (24.5 mg, 0.0583 mmol), CsF (42 mg, 0.1284 mmol), and 10 mL CH_3CN. The reaction was stirred for 24 hr and the product characterized *in situ* by ^1H NMR spectroscopy. The spectrum shows free ligand and a complex mixture of paramagnetic compounds.

Synthesis of 1^{Br}-PF_6: A 20 mL scintillation vial was charged with $NiBr_2L^H$ (25 mg, 0.0320 mmol) and 5 mL CH_3CN. Separately, $TlPF_6$ (12.2 mg, 0.0349 mmol) was dissolved in 1 mL CH_3CN, and combined with the $NiBr_2L^H$ solution. The solution was mixed and allowed to stand for 10 min for TlBr to precipitate. The green solution was filtered and dried to a green residue that was further washed with pentane to afford a green solid (25 mg, 93% yield). This sample was subjected to elemental analysis: Calc. for $C_{36}H_{33}BrF_6N_7NiP+H_2O$ C, 49.97; H, 4.08; N, 11.33. Found C, 49.58; H, 3.83; N, 11.32. Single, X-ray quality crystals were grown by diffusion of Et_2O into a CH_3CN solution of **1^{Br}-PF_6** at room temperature. MALDI-TOF of $C_{36}H_{33}BrF_6N_7NiP$: Calc. 700.133; Found 701.649. ^1H NMR (CH_3CN, 25 °C) δ 7.06, 7.26, 7.37, 10.07, 35.01, 63.14. ^{19}F NMR (CH_3CN, 25 °C) δ -72.87 (d). Selected IR data (KBr) ν = 3242, 3105, 3035, 1617, 1593, 1576, 1528, 1473, 1456, 1349, 1169, 837 cm^{-1}. μ_{eff} = 2.51 +/- 0.24 (25 °C, CH_3CN).

Synthesis of 1^{Br}-BAr″$_4$: A 20 mL scintillation vial was charged with $NiBr_2L^H$ (39.5 mg, 0.0505 mmol) and 7 mL CH_3CN. Separately, TlBAr'$_4$ (59.7 mg, 0.0559 mmol) was dissolved in 3 mL CH_3CN, and combined with the $NiBr_2L^H$ solution. The solution was mixed and allowed to stand for 10 min for TlBr to precipitate. The green solution was filtered and dried to a green solid (76 mg, 96% yield). MALDI-TOF of $C_{68}H_{45}BBrF_{24}N_7Ni$– BAr′$_4$: Calc. 700.133; Found 699.224. ^1H NMR (CH_3CN, 25 °C) δ 7.05, 7.24, 7.36, 10.09, 35.51, 63.41. ^{19}F NMR (CH_3CN, 25 °C) δ -63.28 (s). Selected IR data (KBr) ν = 3261, 3107, 3040, 1619, 1596, 1578, 1531, 1475, 1460, 1355, 1277, 1124, 996, 887, 838, 785, 747, 714, 682 cm^{-1}. UV-vis (THF, room temperature; λ_{max}, molar absorptivity): 638 nm, 13 $cm^{-1}M^{-1}$; 1075 nm, 20 $cm^{-1}M^{-1}$). μ_{eff} = 2.64 +/- 0.16 (25 °C, CH_3CN).

Synthesis of 1^{Cl}-PF$_6$: A 20 mL scintillation vial was charged with $NiCl_2L^H$ (39.2 mg, 0.0565 mmol) and ~8 mL CH_3CN. Separately, $TlPF_6$ (20.6 mg, 0.0590 mmol) was dissolved in ~1 mL CH_3CN and combined with the $NiCl_2L^H$ solution. The solution was mixed and allowed to stand for 20 min for TlCl to precipitate. The green solution was filtered and dried, then extracted with CH_2Cl_2, filtered, and dried to a bright green residue that was further washed with pentane to afford a green solid (39.9 mg, 88% yield). This sample was subjected to elemental analysis: Calc. for $C_{36}H_{33}ClF_6N_7NiP$ C, 53.86; H, 4.14; N, 12.21. Found C, 53.46; H, 4.34; N, 12.24. Single, X-ray quality crystals were grown by diffusion of Et_2O into a CH_3CN solution of **1^{Cl}-PF$_6$** at room temperature. MALDI-TOF of $C_{36}H_{33}ClF_6N_7NiP$ – PF_6: Calc. 656.184; Found: 655.720. ^1H NMR (CH_3CN, 25 °C) δ 7.09, 7.37, 10.07, 35.98, 63.24. ^{19}F NMR (CH_3CN, 25 °C) δ -72.87 (d). Selected IR data (KBr) ν = 3246, 3104, 3040, 1616, 1593, 1577, 1529, 1474, 1456, 1352, 1277, 1168, 118, 837, 780, 748, 694 cm^{-1}. μ_{eff} = 2.58 +/- 0.11 (25 °C, CH_3CN).

Synthesis of 1^{Cl}-BAr″$_4$: A 20 mL scintillation vial was charged with $NiCl_2L^H$ (19.8 mg, 0.02865 mmol) and ~5 mL CH_3CN. Separately, TlBAr'$_4$ (30.6 mg, 0.0287 mmol) was dissolved in ~1 mL

CH_3CN and combined with the $NiCl_2L^H$ solution. The solution was mixed and allowed to stand for 20 min for TlCl to precipitate. The green solution was filtered and dried to afford a green solid (40.5 mg, 92% yield). MALDI-TOF of $C_{68}H_{45}BClF_{24}N_7Ni$ – BAr′$_4$: Calc. 656.184; Found: 655.357. ^1H NMR (CH_3CN, 25 °C) δ 7.08, 7.36, 10.06, 36.02, 63.41. ^{19}F NMR (CH_3CN, 25 °C) δ -63.27 (s). Selected IR data (KBr) ν = 3368, 3322, 3111, 3041, 2932, 1620, 1596, 1580, 1527, 1477, 1458, 1355, 1278, 1123, 997, 839, 785, 746, 713, 682 cm^{-1}, UV-vis (THF, room temperature; λ_{max}, molar absorptivity): 638 nm, 19 $cm^{-1}M^{-1}$; 1046, 28 $cm^{-1}M^{-1}$. μ_{eff} = 2.22 +/- 0.13 (25°C, CH_3CN). **Synthesis of 1^F-PF_6:** A 20 mL scintillation vial was charged with NiF_2L^H (34.9 mg, 0.0529 mmol) and 5 mL CH_3CN. Separately, $TlPF_6$ (22 mg, 0.0630 mmol) was dissolved in 1 mL CH_3CN, and combined with the NiF_2L^H solution. The solution was stirred for 2 h to allow TlF to precipitate. The blue-green solution was filtered and dried to a blue-green residue solid. The solid was extracted with CH_2Cl_2 and dried, then washed with 5 mL pentane and dried to afford a green solid (30.1 mg, 72% yield). This sample was subjected to elemental analysis: Calc. for $C_{33}H_{36}F_7N_7NiP$ C, 54.99; H, 4.23; N, 12.47. Found C, 54.88; H, 4.25; N, 12.66. Single, X-ray quality crystals were grown by diffusion of Et_2O into a CH_3CN solution of **1^F-PF_6** at room temperature. MALDI-TOF of $C_{33}H_{36}F_7N_7NiP$ – PF_6: Calc. 640.213; Found 639.716. ^1H NMR (CH_3CN, 25 °C) δ 7.12, 7.46, 7.84, 10.45, 38.58, 65.03, 81.50. ^{19}F NMR (CH_3CN, 25 °C) δ -72.31 (d). IR data (KBr) ν = 3247, 3111, 3035, 1616, 1594, 1578, 1533, 1475, 1458, 1352, 1167, 997, 837, 782, 748, 695 cm^{-1}. μ_{eff} = 2.49 +/- 0.05 (25°C, CH_3CN).

Synthesis of 1^F-BAr″$_4$: A 20 mL scintillation vial was charged with NiF_2L^H (18.9 mg, 0.02862 mmol) and 5 mL CH_3CN. Separately, TlBAr'$_4$ (31 mg, 0.02904 mmol) was dissolved in 1 mL CH_3CN, and combined with the NiF_2L^H solution. The solution was stirred for 1 h to allow TlF to precipitate. The blue-green solution was filtered and dried to a blue-green solid (41 mg, 95% yield).

This sample was subjected to elemental analysis: Calc. for C33H36F7N7NiP C, 54.99; H, 4.23; N, 12.47. Found C, 54.88; H, 4.25; N, 12.66. MALDI-TOF of $C_{68}H_{45}BF F_{24}N_7Ni$ – BAr'$_4$: Calc. 640.214; Found 639.926 ^{1}H NMR (CD_3CN, 25 °C) δ 7.12, 7.46, 7.66, 7.84, 10.45, 38.91, 65.25, 81.52. ^{19}F NMR (CH_3CN, 25 °C) δ -63.29 (s). IR data (KBr), ν = 3359, 3108, 3042, 1666, 1620, 1602, 1583, 1479, 1355, 1279, 1124, 888, 839, 786, 745, 713, 682 cm^{-1}. UV-vis (THF, room temperature; λ_{max}, molar absorptivity): 581 nm, 11 cm^{-1}M^{-1}; 937 nm, 15 cm^{-1}M^{-1}.

Synthesis of [NiClTPA]PF$_6$: A 20 mL scintillation vial was charged with $NiCl_2$TPA (19.9 mg, 0.0474 mmol) and ~8 mL CH_3CN. Separately, $TlPF_6$ (18 mg, 0.0515 mmol) was dissolved in ~2 mL CH_3CN and combined with the $NiCl_2$TPA solution. The solution was mixed to allow TlCl to precipitate. The pale blue solution was filtered and dried to afford a pale blue solid (26 mg, quantitative yield). Single, X-ray quality crystals were grown by diffusion of Et_2O into a CH_3CN solution of [NiClTPA]PF$_6$ at room temperature. LC-MS of $C_{50}H_{30}BClF_{24}N_4Ni$ – PF_6 – Cl: Calc. 348.0885; Found 349.1031. ^{1}H NMR (CH_3CN, 25 °C) δ 13.86, 44.63, 52.07. ^{19}F NMR (CH_3CN, 25 °C) δ -72.53 (d). IR data (ATR) ν = 1738, 1608, 1443, 1371, 1287, 1217, 1101, 1054, 1025,831, 763 cm^{-1}.

Synthesis of [NiClTPA]BAr″$_4$: A 20 mL scintillation vial was charged with $NiCl_2$TPA (30 mg, 0.0714 mmol) and ~8 mL CH_3CN. Separately, TlBAr'$_4$ (76.3 mg, 0.0715 mmol) was dissolved in ~2 mL CH_3CN and combined with the $NiCl_2$TPA solution. The solution was mixed to allow TlCl to precipitate. The pale blue solution was filtered and dried to afford a pale blue solid (74 mg, 83% yield). This sample was subjected to elemental analysis: Calc. for $C_{50}H_{30}BClF_{24}N_4Ni+H_2O$ C, 47.45; H, 2.55; N, 4.43. Found C, 47.15; H, 2.55; N, 4.13. Single, X-ray quality crystals were grown by diffusion of Et_2O into a CH_3CN solution of [NiClTPA]PF$_6$ at room temperature. LC-MS of $C_{50}H_{30}BClF_{24}N_4Ni$ – BAr'$_4$ – Cl: Calc. 348.0885; Found 349.0958. ^{1}H NMR (CH_3CN, 25 °C) δ

7.66, 13.88, 44.82, 52.12. ^{19}F NMR (CH_3CN, 25 °C) δ -63.28 (s). IR data (ATR), ν = 1607, 1354, 1274, 1109, 885, 838, 764, 714, 682, 669 cm^{-1}. UV-vis (THF, room temperature; λ_{max}, molar absorptivity): 611 nm, 23 cm^{-1}M^{-1}; 998 nm, 28 cm^{-1}M^{-1}. μ_{eff} = 2.50 +/- 0.16 (25 °C, CH_3CN).

Synthesis of [NiBrTPA]BAr″$_4$: A 20 mL scintillation vial was charged with $NiBr_2TPA$ (30 mg, 0.0590 mmol) and ~8 mL CH_3CN. Separately, $TlBAr'_4$ (63 mg, 0.0590 mmol) was dissolved in ~2 mL CH_3CN and combined with the $NiBr_2TPA$ solution. The solution was mixed to allow TlBr to precipitate. The pale blue solution was filtered and dried to afford a pale blue solid (69 mg, 91% yield). LC-MS of $C_{50}H_{30}BBrF_{24}N_4Ni$ – BAr'_4 – Br: Calc. 348.0885; Found 349.1022. ^{1}H NMR (CH_3CN, 25 °C) δ 7.65, 14.06, 45.91, 51.43. ^{19}F NMR (CH_3CN, 25 °C) δ -63.22 (s). Selected IR data (ATR), ν = 1610, 1440, 1350, 1270, 1120, 886, 838, 763 680 cm^{-1}.

Synthesis of 2^{Br}: A 20 mL scintillation vial was charged with **1^{Br}-PF$_6$** (13.8 mg, 0.0163 mmol) and 3 mL THF. Separately, KC_8 (2.7 mg, 0.0200 mmol) was combined with 2 mL THF in an 8 mL vial, and both solutions were cooled to -78 °C in a cold-well. After 30 minutes, the KC_8 stock solution was added dropwise to the cold solution of **1^{Br}-PF$_6$** with stirring. The pale green solution turned a dark purple upon addition, and was then allowed to stir for ~5 min. This solution was kept in the cold-well at -78°C for 30 minutes before filtering. This solution was dried, extracted with 5 mL toluene, filtered and dried. The residue was redissolved in minimum toluene, filtered, and dried to a dark green solid (4.1 mg, 36% yield). ^{1}H NMR (THF, 25 °C) δ 7.01, 7.24, 15.81, 18.38. IR data (KBr) ν = 3422, 3220, 3103, 3036, 2920, 1612, 1594, 1577, 1498, 1474, 1449, 1355, 1164, 843, 782, 748, 696 cm^{-1}. UV-vis (THF, room temperature; λ_{max}, molar absorptivity): 555 nm, 3030 cm^{-1}M^{-1}.

Alternate synthesis of 2^{Br}: A 20 mL scintillation vial was charged with **1^{Br}-BAr″$_4$** (25.6 mg, 0.0164 mmol) and 3 mL THF. Separately, KC_8 (2.8 mg, 0.0207 mmol) was combined with 2 mL

THF in an 8 mL vial, and both solutions were cooled to -78°C in the cold-well. After 30 minutes, the KC_8 stock solution was added dropwise to the cold solution of **1^{Br}-BAr″$_4$** with stirring. The pale green solution turned a dark purple upon addition, and was then allowed to stir for ~5 min. This solution was kept in the cold-well at -78 °C for 30 minutes before filtering. The product was characterized *in situ* by ^{1}H NMR spectroscopy. ^{1}H NMR (THF, 25 °C) δ 6.72, 6.96, 7.52, 7.74, 15.43, 17.94. EPR (toluene, 110K): $g_x = 2.055$, $g_y = 2.245$, $g_z = 2.265$, linewidth = 18, 60, 60 G (Frequency: 9.258 GHz. Power: 10.28 W. Modulation: 100.00 kHz.). Elemental analysis of **2^{Br}** could not be obtained due to the thermal instability of the complex.

Synthesis of 2^{Cl}: A 20 mL scintillation vial was charged with **1^{Cl}-PF_6** (14.7 mg, 0.0183 mmol) and 3 mL THF. Separately, KC_8 (3.0 mg, 0.0222 mmol) was combined with 2 mL THF in an 8 mL vial, and both solutions were cooled to -78 °C in the cold-well. After 30 minutes, the KC_8 stock solution was added dropwise to the cold solution of **1^{Cl}-PF_6** with stirring. The pale green solution turned a dark blue upon addition, and was then allowed to stir for ~5 min. This solution was kept in the cold-well at -78 °C for 30 minutes before filtering. This solution was dried, extracted with 5 mL toluene, filtered and dried. The residue was redissolved in minimum toluene, filtered, and dried to a dark blue solid (7.1 mg, 59%). ^{1}H NMR (THF, 25 °C) δ 6.78, 7.05, 19.21. IR data (KBr) ν = 3414, 3208, 3104, 3032, 1595, 1577, 1497, 1474, 1448, 1355, 1262, 1164, 997, 844, 779, 749, 696 cm^{-1}. UV-vis (THF, room temperature; λ_{max}, molar absorptivity): 600 nm, 1941 cm^{-1}M^{-1}.

Alternate synthesis of 2^{Cl}: A 20 mL scintillation vial was charged with **1^{Cl}-BAr′″$_4$** (24.0 mg, 0.0158 mmol) and 3 mL THF. Separately, KC_8 (2.6 mg, 0.01923 mmol) was combined with 2 mL THF in an 8 mL vial, and both solutions were cooled to -78 °C in the cold-well. After 30 minutes, the KC_8 stock solution was added dropwise to the cold solution of **1^{Cl}-BAr″$_4$** with stirring. The pale green solution turned a dark blue upon addition, and was then allowed to stir for ~5 min. This solution was kept in the cold-well at -78 °C for 30 minutes before filtering. The product was characterized *in situ* by ^{1}H NMR spectroscopy. ^{1}H NMR (THF, 25 °C) δ 6.77, 7.05, 7.52, 7.74, 12.03, 18.98. EPR (toluene, 110K): g_x = 2.020, g_y = 2.280, g_z = 2.210, linewidth = 50, 20, 90 G (Frequency: 9.229 GHz. Power: 10.28 W. Modulation: 100.00 kHz). $t_{1/2}$ (THF, 25 °C) = 5.1 h. Elemental analysis of **2^{Cl}** could not be obtained due to the thermal instability of the complex.

Synthesis of 2^F: A 20 mL scintillation vial was charged with **1^F-PF_6** (9.9 mg, 0.0126 mmol) and 3 mL THF. Separately, KC_8 (2.2 mg, 0.0163 mmol) was combined with 1 mL THF in an 8 mL vial, and both solutions were cooled to -78°C in the cold-well. After 30 minutes, the KC_8 stock solution was added dropwise to the cold solution of **1^F-PF_6** with stirring. The pale green solution turned a dark blue-green upon addition, and was then allowed to stir for ~5 min. This solution was kept in the cold-well at -78 °C for 30 minutes before filtering. This solution was dried, extracted with 5 mL toluene, filtered and dried. The residue was redissolved in minimum toluene, filtered, and dried to a dark green solid (3.0 mg, 37% yield). Single, X-ray quality crystals were grown by diffusion of pentane into a THF solution of **2^F** at -35 °C. ^{1}H NMR (THF, 25 °C) δ 6.51, 7.03, 7.36, 18.55. IR data (KBr) ν = 3415, 3185, 3037, 2920, 1613, 1597, 1579, 1498, 1476, 1450, 1356, 1278, 1165, 841, 748, 696, 558 cm^{-1}. UV-vis (THF, room temperature; λ_{max}, molar absorptivity): 706 nm, 1444 cm^{-1}M^{-1}. EPR (toluene, 110 K): g_x = 2.270, g_y =2.240, g_z = 2.028, linewidth = 25, 25, 5 G (Frequency: 9.312 GHz. Power: 10.28 W. Modulation: 100.00 kHz). Elemental analysis of **2^F** could not be obtained due to the thermal instability of the complex.

Synthesis of NiClTPA: A 20 mL scintillation vial was charged with [NiClTPA]BAr″$_4$ (20.7 mg, 0.0166 mmol) and 3.0 mL THF. Separately, KC_8 (2.6 mg, 0.0192 mmol) was combined with 2.0 mL THF in an 8 mL vial, and both solutions were cooled to -78°C in the cold-well. After 30 minutes, the KC$_8$ stock solution was added dropwise to the cold solution of [NiClTPA]BAr″$_4$ with stirring. The pale blue solution turned a blue-green upon addition, and was then allowed to stir for ~5 min. This solution was kept in the cold-well at -78 °C for 30 minutes before filtering. This solution was characterized *in situ* by ^{1}H NMR, EPR, and electronic absorption spectroscopies. ^{1}H NMR (THF, 25 °C) δ 7.53, 7.75, 32.18. UV-vis (THF, room temperature; λ_{max}, molar absorptivity) 726 nm, 4245 cm^{-1}M^{-1}. EPR (THF, 110 K): $g_x = 2.10$, $g_y = 2.20$, $g_z = 2.09$, linewidth = 70.0, 20.0, and 70.0 G (Frequency: 9.258 GHz. Power: 10.28 W. Modulation: 100.00 kHz). $t_{1/2}$ (THF, 25 °C) = 0.3 h.

Synthesis of NiBrTPA: A 20 mL scintillation vial was charged with [NiBrTPA]BAr±$_4$ (17 mg, 0.0163 mmol) and 2.0 mL THF. Separately, KC$_8$ (2.2 mg, 0.0185 mmol) was combined with 1.0 mL THF in an 8 mL vial, and both solutions were cooled to -78 °C in the cold-well. After 30 minutes, the KC$_8$ stock solution was added dropwise to the cold solution of [NiBrTPA]BAr'$_4$ with stirring. The pale blue solution turned a blue-green upon addition, and was then allowed to stir for ~5 min. This solution was kept in the cold-well at -78 °C for 30 minutes before filtering. This solution was characterized *in situ* by ^{1}H NMR spectroscopy. ^{1}H NMR (THF, 25 °C) δ 7.54, 7.75.

2.9.4 *in situ* NMR characterization of $\mathbf{1^F}$-PF$_6$

Low temperature ^{1}H NMR study: A screw-cap NMR tube was charged with **1^F-PF$_6$** in THF. The ^{1}H NMR spectrum of **1^F-PF$_6$** was taken at the following temperatures (shown from top to bottom in the stacked spectra): 25, 10, 0, -10, -20, -40, -60, -75°C.

Preparation of 1^F(DMAP)-PF$_6$: A screw-cap NMR tube was charged with **1^F-PF$_6$** (8.9 mg, 0.0113 mmol) and 1.8 mL THF. A stock solution of DMAP was prepared in THF (32.7 mg in 1.0 mL THF, C = 0.2677 M) and 40 μL was delivered to the NMR tube. The tube was capped and inverted to mix and the product characterized *in situ* by ^{1}H NMR spectroscopy. ^{1}H NMR (THF, 25 °C) δ 7.07, 7.33, 7.81, 9.29, 10.33, 28.57, 36.68, 40.36, 60.79, 66.02, 78.17

2.9.5 Half-life determination by UV-vis

General procedure: In the cold well of the glovebox, the procedure for the reduction to Ni^{I} using KC_8 (above) is followed, using an exact amount of THF (5.0 mL). Following filtration of graphite, 0.7 mL of the solution was loaded into a 0.1 cm pathlength quartz UV-vis cuvette. The threads were then taped with Teflon tape, capped, and Teflon tape wrapped around the outside of the cap. This was brought out of the box and equilibrated at ambient temperature for 5 minutes before the kinetics scans on the Cary-50 instrument were started. Absorbance data from 1100 to 200 nm was collected every 2 min for 3.5 h.

For 2^{Cl}**:** $\mathbf{1^{Cl}}$**-BAr″**$_4$ (24 mg, 0.01578 mmol) dissolved in 3.0 mL THF was combined at -78°C with a cold slurry of KC_8 (2.6 mg, 0.01923) in 2.0 mL THF. This solution was filtered before being added to the cuvette for measurement.

*For NiClTPA***:** [NiClTPA]BAr″$_4$ (20.7 mg, 0.01659 mmol) was dissolved in 3.0 mL THF and combined at -78 °C with a cold slurry of KC_8 (2.6 mg, 0.01923 mmol) in 2.0 mL THF. This solution was filtered and transferred to the cuvette for measurement.

2.9.6 Ligand deuteration

A 20 mL scintillation vial was charged with L^{H} (51 mg, 0.0905 mmol), 4.0 mL d_3-MeCN, 1.0 mL D_2O, and 330 μL of a stock solution of DCl in D_2O (0.0063 M). The solution was stirred at 35°C for 1 hr before removing the solvent under vacuum at 40°C and drying for >1h at 40°C. A second iteration used 500 μL of the DCl stock solution and was dried for 1 hr at 40°C. The product was characterized by ^{1}H and ^{2}H NMR spectroscopy in CH_2Cl_2 using C_6D_6 as an internal standard.

Deuterium incorporation was determined by integrating the ^{2}H NMR spectrum against the internal standard (36% incorporation based on relative integration).

2.9.7 Fluoride abstraction reactions:

General procedure: A THF solution of **2^{Br}/NiXTPA (X = Br or Cl)** was added to a vial equipped with a stir bar and chilled in the cold well in the glovebox for at least 15 min. A cold THF solution of $TlBAr''_4$ was added followed by rapid addition of a cold solution of substrate by autopipette. This solution was mixed well and allowed to warm to room temperature. The products were characterized *in situ* by ^{1}H NMR spectroscopy.

$NaBF_4$:

2^{Br}: The stock solutions were chilled prior to use at -78 °C in the cold well. **2^{Br}** (0.75 mL, 0.0026 mmol), $TlBAr''_4$ (119 μL, 0.0033 mmol), and $NaBF_4$/15c5 (140 μL, 0.0028 mmol) were combined according to the general procedure at -78 °C and stirred at room temperature for 30 minutes. The product was characterized *in situ* by ^{1}H NMR spectroscopy. ^{1}H NMR (THF, 25 °C) δ 7.22, 7.53, 7.75, 9.56, 38.90, 63.82.

NiBrTPA: The stock solutions were chilled prior to use at -78 °C in the cold well. NiBrTPA (0.60 mL, 0.0026 mmol), $TlBAr''_4$ (121 μL, 0.0034 mmol), and $NaBF_4$/15c5 (142 μL, 0.0029 mmol) were combined according to the general procedure at -78°C and stirred at room temperature for 30 minutes. The product was characterized *in situ* by ^{1}H NMR spectroscopy. ^{1}H NMR (THF, 25 °C) δ 7.52, 7.74.

$NaSbF_6$:

2^{Br}: The stock solutions were chilled prior to use at -78 °C in the cold well. **2^{Br}** (0.50 mL, 0.0027 mmol), $TlBAr''_4$ (77 μL, 0.0027 mmol), and $NaSbF_6$/15c5 (138 μL, 0.0027 mmol) were combined according to the general procedure at -78 °C and stirred at room temperature for 60

minutes. The product was characterized *in situ* by ^{1}H NMR spectroscopy. ^{1}H NMR (THF, 25 °C) δ 7.09, 7.35, 7.53, 7.74, 9.47, 35.55, 61.66.

NiClTPA: The stock solutions were chilled prior to use at -78 °C in the cold well. NiClTPA (0.50 mL, 0.0027 mmol), TlBAr″$_4$ (77 μL, 0.0027 mmol), and NaSbF$_6$/15c5 (138 μL, 0.0027 mmol) were combined according to the general procedure at -78 °C and stirred at room temperature for 60 minutes. The product was characterized *in situ* by ^{1}H NMR spectroscopy. ^{1}H NMR (THF, 25 °C) δ 7.75, 7.74, 12.88, 43.83, 52.83.

NFSI:

2^{Br}: The stock solutions were chilled prior to use at -98 °C in the cold well. **2^{Br}** (0.50 mL, 0.0027 mmol), TlBAr″$_4$ (155 μL, 0.0027 mmol), and NFSI (83 μL, 0.0027 mmol) were combined according to the general procedure at -98 °C and stirred at room temperature for 45 minutes. The product was characterized *in situ* by ^{1}H NMR spectroscopy. ^{1}H NMR (THF, 25 °C) δ 6.95, 7.17, 7.32, 7.54, 7.72, 7.91, 9.49, 9.74, 34.43, 37.00, 38.72, 40.68, 62.20, 64.08.

NiClTPA: The stock solutions were chilled prior to use at -98 °C in the cold well. **2^{Br}** (0.50 mL, 0.0027 mmol), TlBAr″$_4$ (155 μL, 0.0027 mmol), and NFSI (83 μL, 0.0027 mmol) were combined according to the general procedure at -98 °C and stirred at room temperature for 45 minutes. The product was characterized *in situ* by ^{1}H NMR spectroscopy. ^{1}H NMR (THF, 25 °C) δ 7.53, 7.72, 7.92, 9.43, 12.53, 13.03, 13.63, 14.01, 40.69, 43.61, 47.62, 49.44, 53.02.

NFTPT:

2^{Br}: The stock solutions were chilled prior to use at -98 °C in the cold well. **2^{Br}** (0.50 mL, 0.0027 mmol), TlBAr″$_4$ (155 μL, 0.0027 mmol), and NFTPT (76 μL, 0.0027 mmol) were combined according to the general procedure at -98 °C and stirred at room temperature for 45

minutes. The product was characterized *in situ* by ^{1}H NMR spectroscopy. ^{1}H NMR (THF, 25 °C) δ 7.18, 7.46, 7.54, 7.73, 7.97, 9.52, 9.74, 35.54, 38.88, 40.73, 62.12, 64.09, 84.95.

NiClTPA: The stock solutions were chilled prior to use at -98 °C in the cold well. NiClTPA (0.50 mL, 0.0027 mmol), TlBAr″$_4$ (155 μL, 0.0027 mmol), and NFTPT (76 μL, 0.0027 mmol) were combined according to the general procedure at -98 °C and stirred at room temperature for 45 minutes. The product was characterized *in situ* by ^{1}H NMR spectroscopy. ^{1}H NMR (THF, 25 °C) δ -24.92, 6.77, 7.54, 7.73, 12.56, 13.00, 14.04, 40.77, 43.82, 46.96, 49.30, 52.33.

2.9.8 Dioxygen activation

O_2 reaction with Ni^I

Following the same dehalogenation procedure described for the fluoride abstraction reactions above, **2^{Br}** (500 μL of 0.0047 M stock solution in THF) was added to a J. Young tube, frozen in liquid N_2, then layered with TlBAr″$_4$ (54 μL, 50 mg, 0.0123 mmol, in 1.0 mL THF) and again. The tube was evacuated and refilled with O_2 and thawed at -78 °C. The reaction was observed by ^{1}H NMR spectroscopy after it was brought to room temperature slowly over an hour. New paramagnetic peaks formed within 1 h upon addition of O_2, with complete consumption of the starting material. We have identified this as a [Ni(OH)L^H]$^+$ species (see synthesis below).

Synthesis of Ni(OH)L^{H}OTf (3). In a 20 mL vial, Ni(OTf)$_2$ (75 mg, 0.210 mmol), L^H (123 mg, 0.218 mmol), and NaOH (9 mg, 0.225 mmol) were combined in CH_3CN (18 mL) and stirred overnight at room temperature. The reaction was filtered, dried, extracted in CH_2Cl_2, filtered and dried. The solid was rinsed with THF and dried to yield a pale blue solid (68 mg, 49 %). Single crystals suitable for x-ray crystallography were grown from Et_2O/CH_3CN. ^{1}H NMR (400 MHz, CH_3CN) δ 7.13, 7.43, 7.88, 10.00, 40.63, 61.87. Selected IR (KBr) ν = 3548, 3185, 3035, 2751, 1617, 1594, 1579, 1498, 1479, 1455, 1361, 1296, 1267, 1229, 1213, 1166, 1024, 1005, 907, 782, 750, 700, 634, 517 cm^{-1}. μ_{eff} = 3.24 (25 °C, CH_3CN).

Chapter 3 Activation of O_2 by an Iron(II) Complex Featuring Secondary Sphere Hydrogen Bonds

Portions of this chapter are in manuscript for publication:

Wilson, J. R; Zeller, M.; Szymczak, N. K.; Hydrogen bonds enable activation of dioxygen at iron: observation of intermediates and subsequent reactivity. *In manuscript.*

3.1 Introduction

Activation of dioxygen in biological systems is critical for oxidation of substrates, specifically incorporation of O_2 directing into C-H bonds.[215] A wide range of enzymes incorporate heme and non-heme iron-containing active sites for the reduction of O_2 using iron.[11, 51] The reduction of O_2 progresses through several high valent intermediates before ultimately reacting with the organic substrate. These intermediates include superoxo and peroxo species, and in a proposed mechanism of activation, high valent mononuclear or bridging Fe-oxo units are implicated as the active species for substrate oxidation.[13, 61] Many routes to access the Fe^{III}-OH arise from the Fe^{II}-OH precursor through chemical oxidation,[56, 216-217] or through OAT reaction,[79, 218] rather than via O_2 activation. Accessing the highly reactive superoxo and peroxo complexes is even more challenging.[76, 85-87] Characterization of these intermediates, particularly the proposed catalytically active high valent oxo species, is of broad interest towards developing synthetic systems which can use O_2 rather than chemical oxidants to access oxidized substrates.

Enzymatic systems typically incorporate acidic residues from nearby amino acids in the secondary coordination sphere of the active sites,[3, 8, 219] which can allow for capture of dioxygen and positioning of the substrates for oxidation, as well as stabilization of key intermediates. In model systems for non-heme iron complexes, such secondary sphere H-bonding moieties are less common, and there are relatively few well characterized iron(III)-hydroxo complexes derived from O_2 that also feature H-bonds. Recent reports from the Fout[220] and Goldberg[162] groups have demonstrated the ability to capture and activate O_2 using Fe^{II} precursors with H-bonding groups. However, one of the key challenges remaining is the identification and characterization of the intermediates of the dioxygen activation to form the terminal Fe^{III}-OH complexes.

There has been extensive work from the Que group using TPA ligands to characterize high-valent intermediates implicated in O_2 activation. One of the early reports of an Fe^{IV}TPA oxo complex was synthesized at low temperature using *m*-chloroperbenzoic acid.[79] More recent work used a soluble iodosoarene variant to generate Fe^{IV}-oxo, which is a proposed intermediates in hydrogen peroxide oxidation reactions of cyclohexene.[55] Importantly, the high valent iron oxo alone was found to be active for HAT of the allyl position over OAT to the C=C bond, while addition of H_2O_2 shifts the product distribution to favor OAT (Fig. 3.1), suggesting a different mechanism of oxidation (i.e. the Fe-oxo is not the species directly responsible for oxidation of cyclohexene). Efforts to access these high valent intermediates directly from O_2 require bridging $Fe_2(OH)_2$ precursors or result only in the formation of a bridging Fe^{III}-O-Fe^{III} terminal product with no observable intermediates – typically dinuclear species are observed.[87]

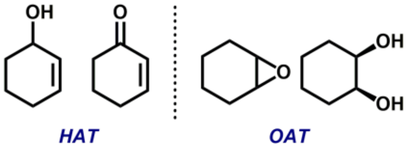

Figure 3.1 Products of cyclohexene oxidation *via* HAT or OAT mechanisms with Fe^{IV}-oxo species.

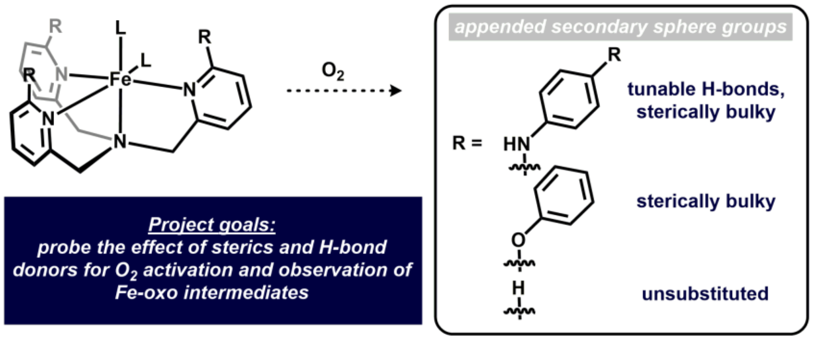

Figure 3.2 Project overview for activation of O_2 with Fe complexes featuring H-bonds

Prior work in our group targeted using the aniline substituted tris(2-pyridyl)amine ligand, L^R (R = *p*-OMe, H, CF_3) to target bridging dimetal peroxo complexes with copper and zinc.[18, 22] The isolated peroxo adducts engaged in H-bonding interactions with the -NHPh moieties, which was proposed as the reason for their stability and isolation. We also reported a phenolic variant of the same ligand, tpa^{OPh}, which provided steric bulk, but lacked H-bond donors. The addition of steric bulk as well as the H-bonds in L^R provides an interesting route to study the effect the secondary sphere coordination environment has on synthetic systems for O_2 activation (Fig 3.2). Based on these studies, we set out to use the L^R platform as a route to access the high valent intermediates of O_2 activation with iron.

3.2 Synthesis and Characterization of a Terminal Fe^{III}-Hydroxo Complex

We began our investigation into the reaction of O_2 with iron complexes by first establishing that a terminal Fe^{III}-OH complex would be compatible with our existing H-bonding ligand, L^H. Stirring $Fe(OTf)_2$, L^H, and NaOH in acetonitrile at room temperature overnight resulted in the formation of $[Fe(OH)L^H]OTf$ (**1**). The Fe^{II}-OH complex was isolated a bright yellow solid following recrystallization from acetonitrile/ether. This complex was characterized by ^1H NMR, IR, electronic, and EPR spectroscopies, as well as by X-ray crystallography. The paramagnetic complex appears symmetric on the ^1H NMR timescale, reminiscent of our previously reported $[Ni(X)L^H]^+$ complexes (X = Br, Cl, F).[125] Infrared spectroscopy clearly shows both N-H and O-H stretches, and electronic absorption spectroscopy reveals strong absorbances in the visible region (404 nm (ε = 1689 $M^{-1}cm^{-1}$), and weak d-d transitions in the near-visible region 803 nm (ε = 17 $M^{-1}cm^{-1}$). The EPR spectrum shows no signals which is consistent with a high spin S = 2 iron center. These data support a formulation of a monomeric Fe(OH) complex as described, and suggest the $^{-}$OTf anion can weakly coordinate to the Fe^{II} center (as observed in the crystal structure, see Fig. 3.4).

The solid state structure of **1** shows trifurcated H-bonds from the -NH groups of the ligand to the bound -OH (Fig. 3.4). The average N…O distance is 2.874 Å, which is within the range of moderately strong H-bonds.[181] The sixth coordination site of the Fe^{II} complex is occupied by the OTf anion, with one of the triflate oxygen atoms engaging in a H-bonding interaction with the Fe-bound -OH ligand (2.958 Å).

The redox capabilities of **1** were evaluated using cyclic voltammetry. This complex displays an irreversible Fe^{II}/Fe^{I} reduction at -2.45 V vs Fc in CH_3CN/[Bu_4N][OTf] electrolyte solution. When scanned oxidatively, complex **1** has a fully reversible Fe^{II}/Fe^{III} oxidation event at 0.04 V, with reversibility maintained over three orders of magnitude of scan rate. This led us to investigate chemical oxidation reactions of **1** to identify and isolate the Fe^{III}-OH complex.

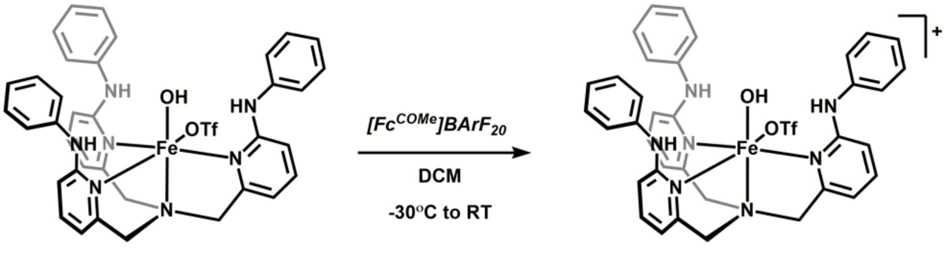

Figure 3.3 Synthesis of Fe^{III}-OH complex, **2**.

Complex **1** was oxidized with one equivalent of acetylferrocenium tetrakis-(pentafluorophenyl) borate ([Fe^{COMe}]BAr'_4) to yield [Fe(OH)L^H(OTf)]BAr'_4 (**2**) (Fig. 3.3). The complex is readily isolated as a deep blue solid following extraction of the acetylferrocene byproduct. NMR characterization of this complex shows complete consumption of **1** and formation of a new complex, with incorporation of the BAr′$_4$ anion. Electronic absorption spectroscopy shows a new absorbance at 640 nm (ε = 990 M^{-1}cm^{-1}). The EPR spectrum is a rhombic high-spin species, with *g* values of ~ 2.9, 2.55, 1.95 (E/D ~ 0.28, *D* = 2). Other Fe^{III}-OH complexes report similar *E/D* values (~ 0.33; ~0.26) and highly shifted effective *g* values (4.3; 5.0, 3.7).[220]

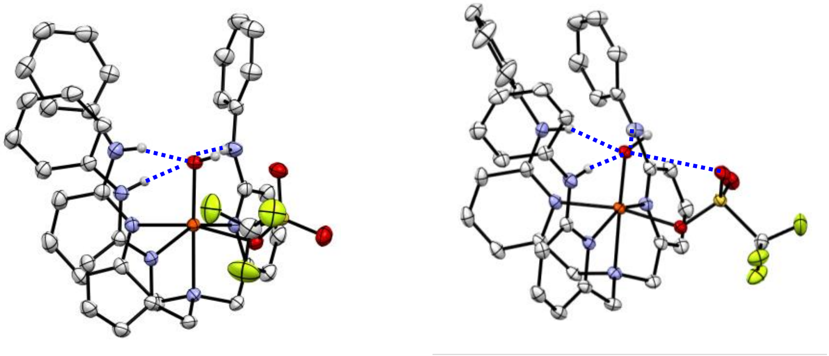

Figure 3.4 Crystal structures of complexes **1** (left) and **2** (right). BAr′$_4$ anion associated with complex **2** not shown. H-bonds shown as blue dashed lines.

X-ray crystallography of a single crystal grown form dichloromethane/ether solution at room temperature give an octahedral complex which is isostructural with complex **1**, with the addition of an outer-sphere BAr′$_4$ anion (Fig. 3.4). The Fe^{III}-OH distance is contracted in **2** (1.850(1) Å) compared to **1** (1.959(1) Å) as is expected upon a one electron oxidation. The H-bonding interactions to the -OH group are maintained and in fact do not significantly change in distance (avg. O…NH distance for **2**: 2.873 Å; for **1**: 2.874 Å), suggesting the H-bond strength in the Fe^{II} to Fe^{III} species are of similar, moderate strength. In the solid state, complex **2** also exhibits intermolecular H-bonding to the bound $^{-}$OTf ligand on second molecule of the complex. With the Fe^{II}-OH and Fe^{III}-OH complex well characterized, demonstrating the ability of this system to stabilize Fe-oxygen complexes, we turned to investigations of dioxygen activation.

3.3 Synthesis of Fe(III)-OH from O_2.

Recent reports from both Goldberg and Fout have detailed the synthesis of Fe^{III}-OH complexes derived from O_2. After establishing a route to the authentic Fe^{III}-OH complex **2**, and based on prior work in our group that showed we could use H-bonding ligand, L^H, to capture O_2,[18, 22] we set out to determine if we could synthesize **2** via activation of dioxygen. Previous work with TPA-derived ligands have identified high valent Fe^{IV}-oxo species as a relatively stable intermediate of dioxygen activation at low temperatures in acetonitrile. In an $[Fe(OH)_2Fe](TPA)_2^+$ complex, a superoxo intermediate is proposed prior to formation of an Fe(O)(OO)Fe core.[87] With this precedent, we investigated O_2 activation by an iron(II) complex with H-bonding ligand L^H.

Based on prior work that demonstrated a high affinity for X-type ligands in the secondary sphere H-bonding pocket, we determined we would need to start from a coordinatively unsaturated Fe^{II} complex. We initially synthesized $Fe(OTf)_2L^H$ (**3**) as a precursor for O_2 activation. Stirring a solution of L^H and $Fe(OTf)_2$ in acetonitrile readily yielded the bis-triflate complex **3** in high yields, which was characterized by ^1H NMR. The asymmetric NMR spectrum indicates the complex is octahedral, with two triflate ions coordinated. When complex **3** was subjected to atmospheric pressure of O_2 in dichloromethane, a color change from bright yellow to pale green was observed. After 3 days, the color darkened to a deeper green, and a single new broad paramagnetic peak was observed, although complex **3** is not significantly consumed, and no other peaks shifted. This data suggests that the bis-triflate complex is relatively stable, and the exchange for O_2 is not readily favored at room temperature for complex **3**.

As an alternate route to dioxygen activation with Fe^{II}, we instead targeted a complex with bulky, non-coordinating counter anions. Iron(II) hexakis-acetonitrile bis-(tetrakis(bis-3,5-trifluoromethylphenyl) borate ($Fe(MeCN)_4(BAr''_4)_2$) was combined with an acetonitrile solution of ligand, L^H, and stirred for 10 min. at room temperature to yield complex **4**, which was isolated as a pale yellow solid. Complex **4** was subjected to an atmosphere of O_2 at -78 °C, and upon warming to room temperature, the yellow solution turned green. After 5 min, a new species was observed by ^{1}H NMR with complete conversion of the Fe^{II} precursor. After 5 hours at room temperature, this intermediate had been completely consumed. To identify the product of this reaction, complex **4** was reacted with O_2 at -45 °C and the electronic absorption spectrum was monitored. A broad peak at 700 nm grew in over the course of 1 h as the solution turned green in color and a new species (**5**) was formed. Addition of 5 equivalents of dihydroanthracene (DHA) at -45 °C did not result in an immediate reaction, however, after bringing the reaction to room temperature over 24 h, the peak at 705 nm underwent a hyposchromic shift to 685 nm. When excess $[NBu_4][OTf]$ is added to this species, the maximum absorbance shifts to 645 nm, consistent with the authentic Fe^{III}-OH(OTf) complex, **2**. We thus propose that the absorbance at 700 nm is consistent with an Fe^{IV}-oxo species (**5**), and the species at 685 nm is the corresponding 5-coordinate Fe^{III}-OH complex (**2a**) (Fig. 3.5).

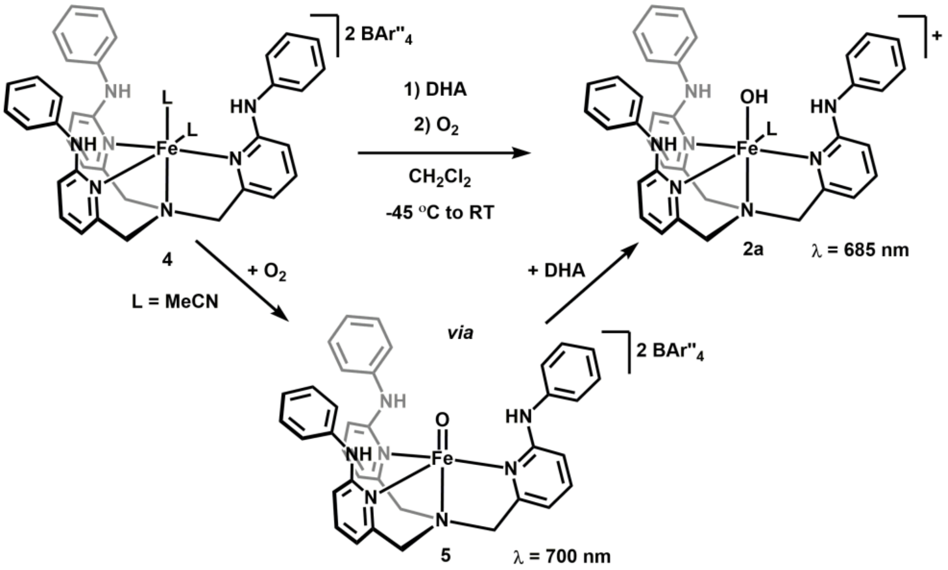

Figure 3.5 O_2 activation by complex **4** as observed by UV-vis spectroscopy.

3.4 Identification of Intermediates in O_2 Activation Route

The intermediates described above from the activation of O_2 by complex **4** at low temperature exhibits a LMCT at 700 nm in CH_2Cl_2. This absorbance is similar to the intermediate (724 nm) observed in the reaction of Fe^{II}(MeCN)TPA with O_2, which leads us to propose complex **5** is an Fe^{IV}-oxo species. In order to better establish this, we subjected complex **4** to 1 equiv. of iodosobenzene (PhIO) while monitoring the electronic absorption spectrum. After 30 min at -45 °C, no reaction had occurred. Allowing the reaction to warm to 0 °C over 1 h resulted in the growth of a peak at 705 nm (Fig. 3.6), along with a shoulder peak at 490 nm. This species decayed over 2 h at -10 °C to a species with an absorbance at 680 nm. When this reaction was allowed to react at -45 °C in the presence of DHA, the species at 685 nm begins to form immediately. We propose that this product at 685 nm is the Fe^{III}-OH species, $[Fe(OH)L^{H}](BAr''_4)_2$ (**3**).

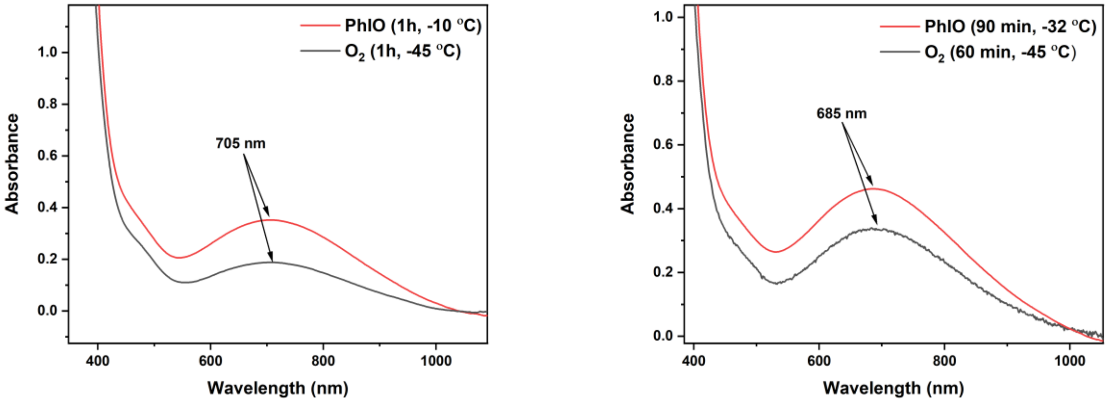

.

Figure 3.6 Left: Overlay of UV-vis spectra from reaction of complex **4** with O_2 (black) or PhIO (red). Right: Overlay of UV-vis spectra from reaction of complex **4** and DHA with O_2 (black) or PhIO (red).

Due to the insolubility of PhIO in CH_2Cl_2, both at room temperature and low temperature, we switched to a more soluble variant, 2-(*tert*-butylsulfonyl)iodosylbenzene, ^{S}PhIO.[221] When ^{S}PhIO is added to complex 4 at -45 °C in CH_2Cl_2, no intermediate species at 700 nm is observed, and instead the solution immediately turns dark blue-green with the growth of a peak at 640 nm within < 10 min. Repeating this reaction at -78 °C slows this reaction down slightly, but still no peak at 700 nm is observed. When performed at -90 °C with slow addition of a cold solution of ^{S}PhIO, we observe the peak at 705 nm form after 2 min and addition of ~ 0.5 eq ^{S}PhIO. Within another 10 min, the maximum peak shifts to 635 nm, consistent with the previously observed product. We attribute the shift from 685 nm to 635 nm for the Fe^{III}-OH to the presence of the sulfone, which could act as a weakly binding ligand, which forms a similar six-coordinate Fe^{III}-OH species, similar to that of the Fe^{III}-OH(OTf) complex (λ_{max} = 640 nm). This has been reported with the related Fe(O)TPA complex, and the increased activity of the complex was also observed.[222] Importantly, the formation of the same intermediate at 705 nm at low temperature as observed in the reaction of **4** and O_2 supports our assignment of this species as the high-valent Fe^{IV}-oxo complex.

In order to establish the necessity of secondary sphere H-bonds in the activation of O_2, we synthesized control complexes $[Fe^{II}(MeCN)_2tpa^{OPh}]BAr''_4$ (**6**) and $[Fe^{II}(MeCN)_2TPA]BAr''_4$ (**7**) in the same manner as complex **4b** (Fig. 3.7). When control complexes **6** and **7** are subjected to O_2 in CH_2Cl_2 at -45 °C, no reaction occurs. No new peaks are observed over the course of several hours, and even warming the reaction solutions to room temperature overnight resulted in no new absorbances. The lack of reactivity of both control complexes provides us with valuable information regarding complex **4**, with its secondary sphere H-bonds. Prior reactions of $FeTPA(OTf)_2$ with O_2 in CH_2Cl_2 only yielded the terminal Fe^{III}-O-Fe^{III} species after 3 days at room temperate,[223] so our observations with complex **7** in this shorter time frame (24 h) is not surprising.

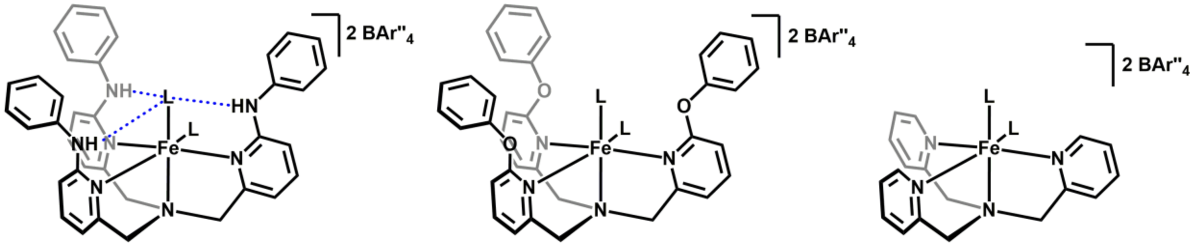

4 6 7

Figure 3.7 Molecular structures of Fe^{II} complexes used to study O_2 activation as an effect of H-bonding and steric bulk. H-bonds shown as blue dashed lines.

We turned to electrochemistry to establish if the variance in reactivity is due to differences in electronics of the different ligands. Cyclic voltammetry experiments were run using $[Bu_4N][BAr''_4]$ in MeCN (0.1 M) as the electrolyte, scanning oxidatively from the open circuit potential, and referenced to ferrocene at the end of the data collection. For all three complexes, no significant signals were observed in a 4 V window; the small irreversible peaks which could be identified were centered near zero, indicating all three complexes should be capable of reduction O_2 ($E°$ in MeCN = +1.21 V vs Fc).[224-225] With the addition of excess $[Bu_4N][Cl]$, clear redox events were observable (Fig. 3.8). For complexes **6** and **7**, a clearly reversible oxidation event is observed ($E_{1/2}$ = -0.47 and -0.31 V at 100 mV/s, respectively). Complex **4** exhibits an irreversible event with a peak oxidative current at -0.38 V, which is within 0.14 V of the oxidation peak currents for the other iron(II) complexes (**6**: -0.36 V; **7**: -0.24 V). We note that the irreversibility of complex **4** is reminiscent of the quasi-reversible nature of the Ni^{II}/Ni^{I} reduction events for the Ni-F species we previously reported.[125] We attribute this to a slower process of $^-$Cl ion exchange at the metal center due to the H-bonding moieties in the complex. Indeed, when the scan rate is changed to slower scan rate (10 mV/s), the event remains irreversible. However, at faster scan rates (1000 mV/s), the reductive wave of the event is observed as the scan rate outpaces the chemical dissociation event. This allows us to obtain an $E_{1/2}$ value of -0.37 V, which is intermediate to complexes **6** and **7**. The more positive oxidation potential of **7** indicates it is less likely to react with O_2 but with such similar potentials across the series (Δ = ~ 150 mV), it is unlikely that the electronic effect plays a significant role in the binding and activation of O_2.

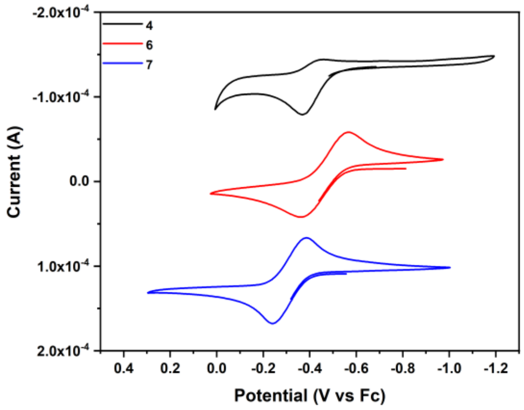

Figure 3.8 Comparison of cyclic voltammetry for complex **4**, **6**, and **7** in the presence of excess $[Bu_4N][Cl]$ in 0.1 M $[Bu_4N][BAr'_4]$ in CH_3CN.

If the activation of O_2 was only related to secondary sphere steric bulk, we would expect to see a reaction with complex **6**, which contains bulky secondary sphere -OPh groups, analogous to the -NHPh groups on complex **4**, but lacks the ability to form H-bonding interactions. However, neither complex **6** nor complex **7** react with dioxygen under our standard conditions. These results suggest that steric bulk alone is not sufficient for dioxygen activation, but that incorporation of secondary sphere H-bonds is necessary enable the activation of O_2. We propose that the interaction of the oxygen atom with the H-bonds provides a kinetic stabilization of the intermediates of O_2 activation (as indicated by our observation of the Fe^{IV}-oxo intermediate), which enables the reaction to proceed where similar complexes without H-bonds do not.

3.5 Reactivity Studies

A recent report from the Goldberg group reported Fe^{III}-OH complexes derived from O_2 that were capable of undergoing a hydroxyl radical rebound to trityl radical.[105] At the same time, the Fout group demonstrated the same reactivity with a different Fe^{III}-OH complex. With our established Fe^{III}-OH complex **2** in hand, as well as a route to access the related species **3** *via* O_2 activation, we evaluated this system for its rebound hydroxylation ability. At room temperature under N_2 atmosphere, [Fe^{COMe}]BAr′$_4$ was added to a solution of complex **1** to generate **2** *in situ*. Subsequent addition of excess Gomberg's dimer yielded trityl alcohol in 62**%** yield (by ^{1}H NMR) after 1 hr (Fig. 3.9). Performing the same reaction using [Fe(OH)TPA]$_2$(OTf)$_2$ as the precursor results in only 13% yield after 24 h. In order to establish the same reactivity as the Goldberg group, we subjected complex **4** to an O_2 atmosphere at -45 °C in the presence of DHA and Gomberg's dimer for 2 h to yield trityl alcohol in 42% yield (by GC). These results are consistent with the reports from Goldberg and Fout and establish the hydroxyl radical rebound reactivity of this Fe^{III}-OH complex.

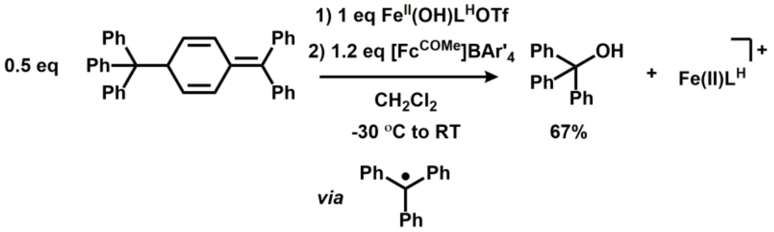

Figure 3.9 Rebound hydroxylation reaction from **2**, generated *in situ*, to Gomberg's dimer.

In addition to the reactivity of the Fe^{III}-OH complex, we were interested in testing the reactivity of the high-valent intermediate. Following the reaction of **4** with O_2 at -45 °C in CH_2Cl_2 for 3 h to generate **5** and warming to room temperature, 30 eq. of cyclohexene (BDE = 81 kcal/mol, DMSO; 109.4 [vinyl], 83.9 [allyl] kcal/mol, gas phase)[226-227] were added to the reaction (Fig. 3.10), at which time the absorbance corresponding to **5** began to immediately decrease. After reacting for 22 h, GC-MS analysis of the solution shows the formation of cyclohexenone, 2-cyclohexen-1-ol, and 2-cyclohexen-1-ol as the major products of the reaction (Table 3.1). All three of these products are the products of hydrogen atom transfer (HAT), as opposed to oxygen atom transfer. There is no evidence of cyclohexene oxide, the product of oxygen atom transfer (OAT), which is the major product of Fe(OTf)$_2$TPA and cyclooctene with O_2 in MeCN.[79] Favoring HAT over OAT is consistent with other work from the Que group that showed the HAT products of cyclohexene with a high-valent Fe^{IV}(O)TPA complex can be favored over OAT products.[55] Additionally, high-spin Fe^{IV}-oxo complexes have been shown to follow a similar pattern of HAT reactivity over OAT into the C=C bond.[228]

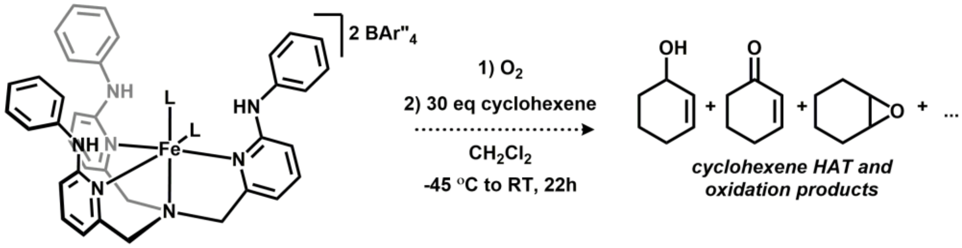

Figure 3.10 Reaction of cyclohexene with the product of O_2 activation by complex **4**. Products detected in the reaction are outlined in Table 3.1.

Table 3.1 Products of cyclohexene oxidation *via* **5** as identified by GCMS.

product	*ratio (% yield)*	*product*	*ratio (% yield)*
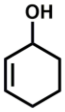	0.1069 (2.06%)	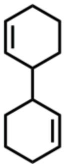	0.1629 (3.15%)
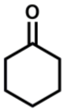	0.0340 (0.65%)		
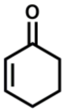	0.1149 (2.22%)	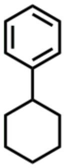	0.0494 (0.95%)
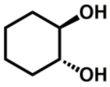	0.0274 (0.53%)	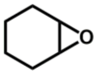	*not observed*

* ratio is vs. GCMS internal standard, % yield calculated from mmol complex 4 used in reation

The products from the reaction with **5** are interesting – while the -enone and -enol products are observed with the high valent Fe(O)TPA complex, the C-C coupled was not reported. This suggests that the rate of HAT is significantly faster than the subsequent OAT and/or hydroxyl group to the carbon radical to form the oxygenated HAT products. This decrease in rate, along with the low conversions for all compounds (no other species observed besides unreacted cyclohexene), is likely due to the H-bonding interactions with the oxygen atom, which enables the carbon radical coupling reaction to form competitively. We acknowledge that the lengthy reaction time with the substrate at warmer temperature may mean that some of these products could be formed as a result of cyclohexene reacting with the iron species formed from HAT (likely complex 2a). There is an ongoing investigation in our group to determine the products derived directly from the high valent Fe^{IV}-oxo intermediate, **5**, and from the Fe(III)-OH product, **2a**.

In order to show divergent reactivity between the Fe(III)-OH complex **2** and proposed Fe^{IV}-oxo complex **5**, we stirred a solution of complex **2** with 10 eq. of cyclohexene for 6 h at room temperature. The solution remained a deep blue color, and the GC-MS analysis showed only trace cyclohexanol and no other products from reactivity with the Fe^{III}-OH. Additionally, reactions of **2** with excess of DHA (BDE: 78 kcal/mol, DMSO)[229] were unproductive, with no reaction observed after a day at room temperature. Complex **2** was only capable of performing HAT reactions with TEMPO-H (BDE: 67.5 kcal/mol, DMSO),[230] forming a new Fe^{II} species we tentatively assign as the Fe^{II}-OH_2. This, along with the product distribution from the reaction with cyclohexene, indicates that the high-valent intermediate **5** is likely responsible for the oxidation products of cyclohexene, and that complex **5** is best characterized as a Fe^{IV}-oxo species. This provides a starting point for determining the O-H BDE of the Fe^{III}-OH species (> 82 kcal/mol). Furthermore, the reactivity of complex **2** for hydroxyl radical transfer makes this system comparable to those reported by Fout from a chemically oxidized Fe^{III}-OH and Goldberg's Fe^{III}-OH derived from O_2.

3.6 Conclusions

We have demonstrated the use of a coordinatively unsaturated $Fe^{II}L^{H}$ precursor featuring secondary sphere H-bonds for the activation of dioxygen to form the Fe^{III}-OH as the terminal product. We have independently synthesized and fully characterized this Fe^{III}-OH complex which can readily undergo hydroxyl radical transfer to Gomberg's dimer. More importantly, we have shown this system is able to capture one of the intermediates of O_2 activation, a high-valent Fe^{IV}-oxo species, which we have compared to relevant known complexes, and with which we can also perform oxidation of cyclohexene. The oxidation products are consistent with HAT reactions, rather than direct OAT, and product distribution is distinct compared to Fe^{II}TPA, which we specifically attribute to the engagement of the oxygen atom in H-bonding interactions with L^H, which slows OAT reactivity. In comparison to reported iron complexes capable of activating dioxygen, our observation of the intermediates of O_2 activation in a complex featuring secondary sphere H-bonds is, to the best of our knowledge, quite unusual. The high-valent Fe-oxo intermediate warrants further study, as does the O_2 activation pathway that results in the formation of the high-valent oxo species. These and related studies will inform us on the interactions of H-bonds to capture and reduce dioxygen and other oxygen-containing species.

3.7 Acknowledgments

We graciously acknowledge Prof. John Anderson and Norman Zhao at the University of Chicago for providing us with the compound ^{S}PhIO. We thank Dr. Jeff Kampf for X-ray crystallography data collection. We thank the members of the Lehnert lab for helpful discussions about EPR, and the Lehnert lab for the use of SpinCount.

3.8 Author Contributions

All synthetic, characterization, and reactivity work was performed by J.R.W. Single crystal X-ray experimental data and structure solution of complex **1** (Fe(OH)L^HOTf) was collected by M.Z. The single crystal X-ray experimental data for **2** ([Fe(OH)LHOTf]BAr′$_4$)was collected by Dr. Jeff Kampf and the structure solved by J.R.W. The manuscript was written by J.R.W.

3.9 Supporting Information

3.9.1 Experimental Details

3.9.2 General considerations:

All air- and moisture-sensitive manipulations were performed using standard Schlenk techniques or in an inert atmosphere glovebox with an atmosphere of purified nitrogen. The glovebox was equipped with a cold well designed for low temperature experiments as well as a −30 °C freezer for cooling samples and crystallizations. Solvents were purified using a Glass Contour solvent purification system through percolation through a Cu catalyst, molecular sieves, and alumina. Solvents were then stored over sodium and/or molecular sieves. Deuterated solvents were purchased from Cambridge Isotope Laboratories and used as received.

Iron(II) trifluoromethanesulfonate, iron(II) bromide, sodium hydroxide, acetylferrocene, silver tetrafluorborate, lithium tetrakis(pentafluorophenyl)borate ethyl etherate, dihydroanthracene, and hexamethylbenzene were purchased from commercial vendors and dried under vacuum before transferring to a nitrogen glovebox. Ferrocene was purchased from a commercial vendor and sublimed prior to use. Thallium tetrakis[3,5-bis(trifluoromethyl)phenyl]borate ($TlBAr''_4$),[205] tris(6-phenylamino-2-pyridylmethyl)-amine (L^H),[22] tris(6-phenoxy-2-pyridylmethyl)amine (tpa^{OPh}),[22] tris(2-pyridylmethyl)amine (TPA),[206] and acetylferrocenium tetrafluoroborate ($[Fc^{COMe}]BF_4$) [231] were synthesized according to literature procedures. $Fe(OTf)_2TPA$,[223] $[Fe_2(OH)_2(TPA)_2](OTf)_2$,[68] and acetylferrocenium tetrakis(pentafluorophenyl) borate ($[Fc^{COMe}]BAr'_4$)[232] were synthesized using modified literature procedures, described below.

NMR spectra were acquired on Varian 400 MHz, 500 MHz, or 600 MHz spectrometers as indicated below. ^{1}H NMR spectra are referenced to non-deuterated internal solvent residuals and are reported in parts per million (ppm) relative to tetramethylsilane. ^{19}F NMR spectra are referenced to their respective ^{1}H spectra. The spectra for paramagnetic molecules were obtained by using an acquisition time of 0.5 s and a relaxation delay of 0.05 s, thus the peak widths reported have an error of ±2 Hz.

IR spectra were recorded on a Nicolet iS10 FT-IR spectrometer with an ATR accessory or KBr pellets as specified. Mass spectra were recorded on an Agilent 6230 TOF HPLC-MS with a liquid phase of 95% acetonitrile, 5% water, 0.1% formic acid. Electronic absorption spectra were recorded at ambient temperature in sealed 1 cm quartz cuvettes (as specified) or with a Hellma Analytics 661.200-QX quartz probe (0.5 cm pathlength) with a Varian Cary-50 spectrophotometer (resolution: <1.5 nm). EPR spectra were collected on a Bruker EMX electron spin resonance spectrometer, with a Bruker 4102-ST cavity, at liquid N_2 temperatures in frozen solvent (specified below). The program SpinCount was used to model EPR spectra (using the Lehnert lab license).

Electrochemistry was performed with a Pinewave Wavenow potentiostat under a dinitrogen atmosphere with a glassy carbon working electrode, a platinum counter electrode, and a silver wire pseudo-reference electrode. Measurements were referenced against an internal ferrocene standard. Electrolyte, $[NBu_4][OTf]$ or $[NBu_4][BAr''_4]$, was used in 0.1 M in CH_3CN or CH_2Cl_2 as specified.

Single crystals of complex **1** were coated with a trace of Fomblin oil and were transferred to the goniometer head of a Bruker Quest diffractometer with kappa geometry, a Cu Kα wavelength (λ = 1.54178 Å) I-μ-S microsource X-ray tube, laterally graded multilayer (Goebel) mirror for monochromatization, and a Photon III C14 area detector. The instrument was equipped with an Oxford Cryosystems low temperature device and examination and data collection were performed at 150 K. Data were collected, reflections were indexed and processed, and the files scaled and corrected for absorption using APEX3[233] and SADABS.[234] The space groups were assigned using XPREP within the SHELXTL suite of programs[235] and solved by direct methods using ShelXS[236] or dual methods using ShelXT[237] and refined by full matrix least squares against F2 with all reflections using Shelxl2018[238] using the graphical interface Shelxle.[239]

H atoms attached to carbon were positioned geometrically and constrained to ride on their parent atoms. C-H bond distances were constrained to 0.95 Å for aromatic and alkene C-H moieties, and to 0.99 and 0.98 Å for aliphatic CH_2 and CH_3 moieties, respectively. Methyl CH_3 were allowed to rotate but not to tip to best fit the experimental electron density. H atoms of pyramidalized R_2NH and of hydroxyl units were refined. N-H distances were restrained to 0.88(2) Å. In the final refinement cycles the damping factor was removed and disordered amine H atoms were set to ride on their carrying N atom. The O-H distances were restrained to 0.84(2) Å. $U_{iso}(H)$ values were set to a multiple of $U_{eq}(C)$ with 1.5 for CH_3 and OH, and 1.2 for C-H, CH_2 and N-H units, respectively.

Single crystal data for **2** were collected using a Rigaku AFC10K Saturn 944+ CCD-based X-ray diffractometer equipped with a low temperature device and a Micromax-007HF Cu-target microfocus rotating anode ($\lambda = 1.54187$ Å) operated at 1.2 kW power (40 kV, 30 mA). The data were collected using CrystalClear 2.016.[240] The X-ray intensities were measured at 293(2) K with the detector placed at a distance 42.00 mm from the crystal. A total of 2028 images were collected with an oscillation width of 1.0° in w. The exposure times were 1 sec. for the low angle images, 3 sec. for high angle. Rigaku d*trek images were exported to *CrysAlisPro* 1.171.40.53 for processing and corrected for absorption.[241] The integration of the data yielded a total of 44977 reflections to a maximum 2θ value of 69.4220° of which 10828 were independent and 10466 were greater than 2σ(I). The final cell constants were based on the xyz centroids of 10828 reflections above 10σ(I). Reflections were merged by SHELXL[242] and the structure solved using the Olex[243] refinement program.

3.9.3 Synthesis of Compounds

Synthesis of [Fe(OH)L^H]OTf (1). Fe(OTf)$_2$ (34 mg, 0.0961 mmol) and L^H (55 mg, 0.098 mmol) were combined in a 20 mL vial with acetonitrile (12 mL). A slurry of NaOH (3.8 mg, 0.095 mmol) in 2 mL acetonitrile was added and the reaction was stirred overnight at room temperature. The resulting orange solution was filtered and dried. The resulting yellow solid was recrystallized from layered acetonitrile/diethyl ether at room temperature to yield a yellow crystalline solid which was decanted, washed with ether, and dried (50 mg, 67%). A single crystal suitable for x-ray crystallography was grown from vapor deposition of Et$_2$O into acetonitrile at room temperature. ESI HPLC-MS of Fe(COO$^-$)L^H: Calc. 664.2123, Found 664.2309; Fe(OH)L^H-H$^+$ Calc. 635.2096, Found 635.2079. Elemental analysis: $C_{37}H_{34}F_3FeN_7O_4S$ calculated C 56.57, H 4.36, N 12.48; found C 55.50, H 4.46, N 11.88. ^{1}H NMR (400 MHz, CH$_3$CN, 25 °C) δ 16, 6.26, 6.48, 19.22, 40.48, 60.71, 64.59. ^{19}F NMR (400 MHz, CH$_3$CN, 25 °C) δ -79.14 ppm. Selected IR data (KBr) ν = 3541, 3235, 3185, 3035, 2618, 1616, 1595, 1578, 1498, 1474, 1455, 1355, 1297, 1272, 1230, 1166, 1024, 1001, 784, 749, 697, 634, 518 cm^{-1}. UV-vis (CH$_2$Cl$_2$): 404 nm (1689 M^{-1}cm^{-1}). $E_{1/2}$ (CH$_3$CN): +0.04 V. $\mu_{eff} = 5.15 \pm 0.17$ (CH$_3$CN, 25 °C).

Synthesis of [Fe^{COMe}]BAr′$_4$. A slurry of [Fc^{COMe}]BF$_4$ (103 mg, 0.327 mmol) in CH$_2$Cl$_2$ was stirred with LiBAr′$_4$•Et$_2$O (284 mg, 0.326 mmol) at room temperature for 4 h. The dark blue solution was then filtered through Celite and the filtrate dried under vacuum. The blue solid was washed with pentane (3 x 5 mL) and dried (275 mg, 93 %). ^{1}H NMR (400 MHz, CH_2Cl_2, 25 °C) δ -12.60, 30.44, 31.58, 36.51 ppm. ^{19}F NMR (400 MHz, CH_2Cl_2, 25 °C) δ -169.05, -164.24, -135.20 ppm.

Synthesis of [Fe(OH)(OTf)L^H]BAr′$_4$ (2). A solution of [Fc^{COMe}]BAr′$_4$ (41.5 mg, 0.0446 mmol) in CH_2Cl_2 (2 mL) was added to a solution of **1** (35 mg, 0.0457 mmol) in CH_2Cl_2 (8 mL) at -30 °C and warmed to room temperature with stirring over 1 h. A stark, rapid color change of the Fe complex from bright yellow to deep blue was observed. The blue solution was filtered and dried. The residue was dissolved in Et_2O (2 mL), then pentane (10 mL) was added, and the solution was triturated to precipitate a blue solid. The orange Fc^{COMe} solution was decanted, and the precipitation was repeated twice. The resulting dark blue solid was dried (57.7 mg, 89%). A single crystal suitable for x-ray crystallography was grown from layered pentane and CH_2Cl_2 at room temperature. ^{1}H NMR (600 MHz, CH_2Cl_2, 25 °C) δ -11.05, -3.71, 8.88, 80.76 ppm. ^{19}F NMR (400 MHz, CH_2Cl_2, 25 °C) δ -164.97, -161.93, -130.51 ppm. Elemental analysis: $C_{61}H_{34}BF_{23}FeN_7O_4S$ + 2 CH_2Cl_2 calculated C 46.29, H 2.34, N 6.00; found C 45.85, H 2.48, N 6.10. IR (KBr) ν = 3448, 3265, 3125, 2923, 2853, 1642, 1624, 1601, 1579, 1514, 1463, 1384, 1271, 1232, 1204, 1173, 1091, 980, 774, 755, 661 cm^{-1}. UV-vis (CH_2Cl_2): 264 nm (2,3966 M^{-1}cm^{-1}), 312 nm (12,532 M^{-1}cm^{-1}), 642 nm (990 M^{-1}cm^{-1}). EPR (CH_2Cl_2/toluene, 130 K, freq. 9.258): g = 2.9, 2.55, 1.95 (*E/D* ~ 0.28, *D* = 2). μ_{eff} = 6.09 ± 0.01 (CH_2Cl_2, 25 °C).

Synthesis of Fe(OTf)$_2$L^H (3). We used a modified preparation of this complex from a prior report.[223] Fe(OTf)$_2$ (37.5 mg, 0.106 mmol) and L^H (62 mg, 0.110 mmol) were stirred in acetonitrile for 4 h at room temperature. The solution was dried, redissolved in a minimum amount of acetonitrile, filtered, and layered with Et_2O. The resulting residue was dried and redissolved in CH_2Cl_2, the precipitated with Et_2O, then pentane, washed with pentane and dried to an off-white solid (38 mg, 39%). ^{1}H NMR (400 MHz, CH_3CN, 25 °C) δ -25.68, -3.95, -3.51, -1.74, 2.81, 2.95, 3.52, 4.45, 6.36, 7.54, 8.00, 11.29, 12.00, 14.92, 16.79, 19.61, 30.65, 34.10, 42.84, 56.54, 60.11, 61.34, 65.83, 67.13, 77.90 ppm. Elemental analysis: $C_{38}H_{33}F_6FeN_7O_6S_2$ calculated C 49.74, H 3.62, N 10.68; found C 48.00, H 3.92, N 10.60.

Synthesis of [Fe(MeCN)$_2$L^H]BAr″$_4$ (4). $FeBr_2$ (19.5 mg, 0.0904 mmol) was dissolved in CH_3CN (2 mL) and a solution of TlBAr″$_4$ (204 mg, 0.1911 mmol) in CH_3CN (3 mL) was added. A white precipitate immediately formed as TlBr was formed. The solution was mixed for 5 min and allowed to settle. The solution was filtered and a solution of L^H (53.5 mg, 0.0949 mmol) in CH_3CN (5 mL) was added. The pale yellow solution became a deeper yellow as the L^H solution was combined. This solution was stirred for 10 min at room temperature, then filtered and dried under vacuum. The residue was redissolved in Et_2O (3 mL) and pentane (6 mL) added to help precipitate the product, then the mixture was dried. The pale yellow solid was washed with additional pentane (4 mL) and dried (195 mg, 95%). ^{1}H NMR (400 MHz, CH_3CN, 25 °C) δ -8.55, 4.86, 7.63, 7.66, 49.55, 64.65, 91.87. ^{19}F NMR (400 MHz, CH_3CN, 25 °C) δ -63.29 ppm. Elemental analysis: $C_{104}H_{63}B_2F_{48}FeN_9 + C_5H_{12}$ calculated C 52.55, H 3.09, 5.01; found C 53.55, H 2.89, N 5.32.

Synthesis of [Fe(MeCN)$_2$tpa^{OPh}] BAr″$_4$ (6). The same procedure as for complex **5** was used with the following reagents: $FeBr_2$ (10.5 mg, 0.0487 mmol), TlBAr″$_4$ (107 mg, 0.1002 mmol), and tpa^{OPh} (27 mg, 0.0476 mmol). Desired compound was obtained as an off-white solid (80 mg, 68%). ^{1}H NMR (600 MHz, CH_3CN, 25 °C) δ -1.92, -1.07, 4.16, 4.74, 7.64, 7.66, 46.99, 55.58, 69.52 ppm. ^{1}H NMR (500 MHz, CH_2Cl_2, 25 °C) δ -11.72, 0.14, 2.52, 6.67, 7.55, 7.74, 47.12, 71.58, 85.86 ppm. ^{19}F NMR (500 MHz, CH_2Cl_2, 25 °C) δ -61.99 ppm.

Synthesis of [Fe(MeCN)$_2$TPA] BAr″$_4$ (7). The same procedure as for complex **5** was used with the following reagents: $FeBr_2$ (9.7 mg, 0.0450 mmol), TlBAr″$_4$ (107 mg, 0.1002 mmol), and TPA (13.9 mg, 0.0479 mmol). Desired compound was obtained as a pale red solid (92.5 mg, 93%). ^{1}H

NMR (500 MHz, CH_3CN, 25 °C) δ 6.48, 7.24, 7.62, 7.65, 8.50, 8.59, 11.10 ppm. ^{19}F NMR (500 MHz, CH_3CN, 25 °C) δ -62.70 ppm. Elemental analysis: $C_{86}H_{48}B_2F_{48}FeN_6$ + CH_3CN calculated C 48.14, H 2.34, N 4.47; found C 48.83, H 2.58, N 4.08.

Synthesis of $[Fe_2(OH)_2TPA_2](OTf)_2$. We used a modified preparation of this complex based on a prior report.[68] TPA (51 mg, 0.1756 mmol) was dissolved in CH_3CN (2 mL) and added to $Fe(OTF)_2$ (58.5 mg, 0.1653 mmol) in CH_3CN (5 mL) followed by addition of NaOH (7.5 mg, 0.1900 mmol) in CH_3CN (3 mL). This solution was stirred overnight at room temperature, then filtered and dried under vacuum. Redissolved in CH_3CN and layered with Et_2O to precipitate a red-brown solid. This was extracted with CH_2Cl_2, filtered, and dried to a red solid (58 mg, 69 %). ^1H NMR (400 MHz, CH_3CN, 25 °C) δ 7.05, 7.16, 8.90, 9.01, 12.32 ppm. ^{19}F NMR (400 MHz, CH_3CN, 25 °C) δ -78.75 ppm.

3.9.4 Reactivity Studies

Reaction of 3 with O_2. A J. Young NMR tube was charged with a solution of complex **3** (10.3 mg, 0.0112 mmol) in CH_2Cl_2 (1 mL), then subjected to freeze/pump/thaw cycles and thawed to -78 °C. The tube was backfilled with O_2 at -78 °C and the tube was inverted to mix and thawed to room temperature. The reaction was monitored by ^1H NMR at room temperature over a week.

Reaction of 3 and $NaBAr''_4$ with O_2. A J. Young NMR tube was charged with a solution of complex **3** (10.5 mg, 0.0114 mmol) and $NaBAr''_4$ (21 mg, 0.0237 mmol) in CH_2Cl_2 (1 mL), then subjected to freeze/pump/thaw cycles and thawed to -78 °C. The tube was backfilled with O_2 at -78 °C and the tube was inverted to mix and thawed to room temperature. The solution turned from yellow to dark green after 2 h. The reaction was monitored by ^1H NMR at room temperature over a week.

Reaction of 3 (generated *in situ*) with Gomberg's dimer. Complex **2** (10.1 mg, 0.0129 mmol) was added to a tared vial with a stir bar, along with [Fc^{COMe}][BAr′$_4$] (13.7 mg, 0.0151 mmol) in a separate vial. Each was dissolved in 2.0 mL CH_2Cl_2, and cooled to -30 °C for 1.5 h. The solutions were combined and allowed to stir at room temperature for 1 h to form complex **3** *in situ* as a dark blue solution. Separately, Gomberg's dimer (4.6 mg, 0.0082 mmol) was dissolved in 1.0 mL CH_2Cl_2 and cooled at -30 °C for 1.5 h. This was added to the stirring solution of 3 and stirred for 1 h at room tempearture. After about 5 minutes, the solution turned a deep emerald green color. Hexamethylbenzene was added as an internal standard. A 600 μL aliquot was removed and put in an NMR tube for quantitative ^{1}H NMR analysis (600 MHz. 25 °C). The product, Ph_3COH, was identified and integrated to 1 H, corresponding to the -OH proton (2.85 ppm).

NMR reaction of 4 with O_2.

^{1}H NMR: A J. Young NMR tube was charged with a solution of complex **4** (8 mg, 0.0033 mmol) in CH_2Cl_2, then subjected to freeze/pump/thaw cycles and thawed to -78 °C. The tube was backfilled with O_2 at -78 °C and the tube was inverted to mix and thawed to room temperature. The reaction was monitored by ^{1}H NMR at room temperature overnight.

NMR reaction of 4 with DHA and O_2.

^{1}H NMR: A J. Young NMR tube was charged with a solution of complex **4** (10 mg, 0.0041 mmol), DHA (0.05 mL of a 0.0577 M solution in CH_2Cl_2) and Me_6Ph (0.05 mL of a 0.0524 M solution in CH_2Cl_2) in CH_2Cl_2 (1 mL). The sample was subjected to freeze/pump/thaw cycles and thawed to -78 °C. The tube was backfilled with O_2 at -78 °C and the tube was inverted to mix and thawed to room temperature. The reaction was monitored by ^{1}H NMR at room temperature overnight.

General Procedure for UV-vis experiments:

The 0.5 cm pathlength dip-probe was assembled with the solution cell and cooled under a flow of N_2. CH_2Cl_2 (3.0 mL) was added via syringe transfer, and the solution cooled to the desired temperature. After equilibrating at temperature, a baseline/zero was collected. Then a background scan of the solution was obtained. A solution of Fe^{II} starting material in CH_2Cl_2 was injected via syringe and allowed to equilibrate to temperature. An initial scan of the Fe^{II} starting material was taken before O_2 or the iodosoarene (with or without DHA) was introduced into the reaction and reaction monitoring began.

Reactions with O_2.

In the UV-vis cell, the Fe^{II} complex was stirred in CH_2Cl_2 was sparged with O_2 for 5 min, then the headspace of the reaction flask purged with O_2 for 15-20 min before the flask was sealed. Kinetic scans were taken every 2 min for the first 3 hr, then switched to longer scan times to observe the reaction with O_2 overtime.

Complex **4**: 0.0048 mmol in 0.5 mL CH_2Cl_2; formation of species **5** was observed with a λ_{max} at 700 nm over an hour.

Complex **6**: 0.007 mmol in 0.5 mL CH_2Cl_2; no new absorbances were observed.

Complex **7**: 0.007 mmol in 0.5 mL CH_2Cl_2; no new absorbances were observed.

Reaction of 4 with DHA and O_2.

Complex **4**: 0.0427 mmol in 0.5 mL CH_2Cl_2. DHA: 0.0427 mmol in 0.5 mL CH_2Cl_2. After reacting for 1.5 h, λ_{max} was observed at 685 nm. Then TBAOTf (0.0097 mmol in 0.5 mL CH_2Cl_2) was added, and the λ_{max} shifted to show the formation of complex **2** at λ_{max} 645 nm.

Reaction of 4 with PhIO.

Complex **4**: 0.007 mmol in 0.45 mL CH_2Cl_2. PhIO: Added 0.5 mL of a slurry in CH_2Cl_2 (3.2 mg, 0.0145 mmol in 1.0 mL). With warming to -10 °C over 1h, λ_{max} forms at 700 nm.

Reaction of 4 with DHA and PhIO.

Complex **4**: 0.006 mmol in 0.4 mL CH_2Cl_2. DHA: 0.0297 mmol in 0.4 mL CH_2Cl_2. PhIO: Added 0.7 mL of a slurry in CH_2Cl_2 (2.7 mg, 0.0123 mmol in 1.0 mL). With warming to -10 °C over 1h, λ_{max} is 685 nm.

Reaction of 4 with ^{S}PhIO at -45 °C.

Complex **4**: 0.004 mmol in 0.5 mL CH_2Cl_2. ^{S}PhIO: 0.005 mmol in 0.55 mL CH_2Cl_2. Scan started within 30s of addition of ^{S}PhIO. Immediate formation of λ_{max} at 656 nm, with the reaction complete after 5 min (λ_{max} 638 nm). No λ_{max} at 700 nm was observed.

Reaction of 4 with ^{S}PhIO at -75 °C.

Complex **4**: 0.004 mmol in 0.5 mL CH_2Cl_2. ^{S}PhIO: 0.005 mmol in 0.5 mL CH_2Cl_2.Start scan within 30s of addition of ^{S}PhIO. Formation of λ_{max} at 656 nm occurred within 4 min, with the reaction complete after 10 min (λ_{max} 645 nm). No λ_{max} at 700 nm was observed.

Reaction of 4 with ^{S}PhIO at -90 °C.

Complex **4**: 0.004 mmol in 0.5 mL CH_2Cl_2. ^{S}PhIO: 0.005 mmol in 0.5 mL CH_2Cl_2. ^{S}PhIO was added dropwise slowly (100 μL/2 min) over 10 min. Formation of λ_{max} at 700 nm occurred within 4 min. After 10 min, the λ_{max} shifted to 645 nm with the full addition of ^{S}PhIO.

Chapter 4 Secondary Sphere Hydrogen Bonds for Reduction of Nitrite with Copper(I)

4.1 Introduction

The activation of dinitrogen, N_2, is critical for biological processes.[148, 244] The global nitrogen cycle consists of the uptake of nitrogen by plants and bacteria for use in converting it to NH_3 and NO_x species, which are later used in the formation of amino acids and promoting biological growth and processes. Some of these NO_x species are involved in denitrification, which converts higher order NO_x compounds back to N_2 for reuse in the global cycle. The intermediates of denitrification, nitric and nitrous oxides, are noxious gases, and nitrous oxide is a potent greenhouse gas. Establishing routes for the reduction of the intermediates in NO_x conversion to N_2 is thus a broad challenge within the larger scientific community.[106]

One of the key steps in the denitrification route is the reduction of nitrite to nitric oxide. This reduction can be mediated by copper nitrite reductases (CuNiRs), which incorporate two copper sites: the T1 center provides the electron for reduction, and the catalytically active T2 site binds $^-NO_2$.[110] Protein crystallography studies capture a side-on Cu-NO_2 species,[245] which should be quite reactive for the nitrosylation of surrounding amino acid residues. Indeed, studies of a synthetic model for CuNiR demonstrate that a κ^2-O,O bound $^-NO_2$ ligand is capable of nitrosylation of nucleophiles leading credence to this mechanism.[246] A different proposed mechanism involves protonation of $^-NO_2$ at the copper active site prior to reduction, after which NO (g) is released to form a Cu^{II}-OH species which can be turned over in the catalytic reaction.[107]

In both cases, secondary sphere H-bonding interactions are crucial for the positioning and binding of $^{-}NO_2$ in the active site.

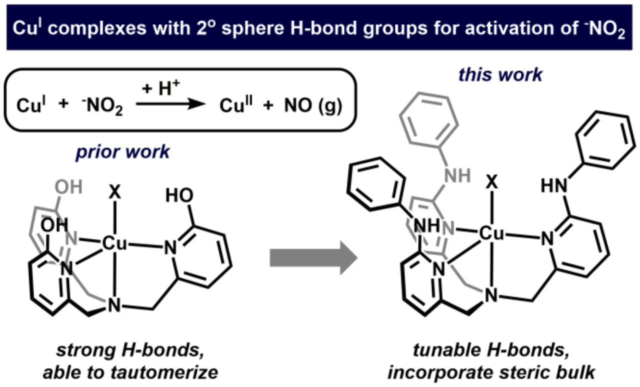

Figure 4.1 Redesigned H-bonding ligand for nitrite reduction with Cu^I complexes.

Prior work in our group demonstrated reduction of $^{-}NO_2$ *via* a copper(I) complex with secondary sphere H-bonds, which are capable of tautomerization (Fig. 4.1). This reaction resulted in immediate reduction of nitrite, and no intermediates of the reduction were observed.[117] Our redesigned ligand featuring tunable -NHPh H-bond donors (L^R) is poised to aid in the capture and observation of the intermediates of nitrite reduction using copper(I).

4.2 Synthesis of $Cu^I(NO_2)L^R$ complexes

4.2.1 Stable complexes: R = *p*-CF_3, *p*-H, *p*-OCH_3

In order to better understand the requirements of H-bond strength for stabilizing the intermediates of $^{-}NO_2$ reduction, we thought we could utilize our modular -$HNPh^R$ appended ligand, L^R, for the synthesis of Cu^I complexes. When a solution of L^R (R = *p*-CF_3, H, OMe) in acetonitrile was combined with copper tetrakisacetonitrile tetrakis(3,5-bistrifluoromethylphenyl)-borate ($Cu(MeCN)_4BAr'_4$) in the presence of tetrabutylammonium nitirite ($TBANO_2$), we obtained $Cu^I(NO_2)$ complexes $\mathbf{1^{CF3}}$, $\mathbf{1^{H}}$ and $\mathbf{1^{OMe}}$ (Fig. 4.2). Characterization by ^1H NMR spectroscopy showed coordination of the L^R ligand, with the -NH proton shifted downfield of the aromatic protons, indicative of H-bonding interactions (L^{CF3}:9.32 ppm, L^H: 9.05 ppm, L^{OMe}: 8.67 ppm) with a Cu-coordinated X-type ligand. Analysis of these complexes by vibrational spectroscopy indicated weak NH-X interactions compared to the free ligand (~ 3200 cm^{-1}). Of the two expected frequencies for the asymmetric $^{-}NO_2$ stretches, only one could be identified due to overlapping with ligand frequencies (*L^{CF3}: 1322, L^{H}: 1328, L^{OMe}: 1339 cm^{-1}). These fall within the same range of frequencies as previously reported copper-nitrite complexes.[247-248]

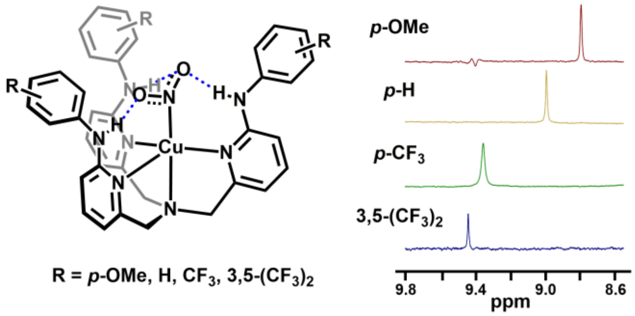

Figure 4.2 Structure of $Cu^{I}(NO_2)L^{R}$ complexes, $\mathbf{1^{R}}$ (left), and associated N-H resonances in the ^{1}H NMR spectrum (right). H-bonds shown as blue dashed lines.

We were able to obtain solid state crystal structures of both $\mathbf{1^{H}}$ and $\mathbf{1^{OMe}}$ (Fig.4.3). Both exhibit η^{1}-N bound $^{-}NO_2$ with H-bonding from two of the -NHPh arms to one O-atom (O1), and the third -NHPh arm H-bonding to the second O-atom (O2, Fig. xx). The distances between the two heavy atoms (N and O) range from 2.825-3.036 Å ($\mathbf{1^{H}}$) and 2.875-3.004 Å ($\mathbf{1^{OMe}}$); these distances are well within the sum of the Van der Waals radii of N and O, consistent with H-bonding interactions.[249] Further, these distances are consistent with moderately strong NH–O bonds. While the nitrite group is formally η^{1}-N bound in both cases, short contact distances (2.723 and 2.781 Å for $\mathbf{1^{H}}$ and $\mathbf{1^{OMe}}$, respectively) between the Cu and O1 atom are observed in both structures. This could be an effect of having two H-bonding interactions to the same O-atom that pull it closer into the same plane as the -NH groups.

Closer inspection of the N-O bond lengths in $\mathbf{1^{H}}$ and $\mathbf{1^{OMe}}$ show slight contraction of one N-O bond, interestingly, the one engaged in a direct 1:1 H-bond contact. We would expect that H-bonding would weaken the N-O bond, but rather the contraction of the bond suggests a larger electronic effect from the Cu^I center, rather than the H-bonding interaction. The bond lengths (1.196(3), 1.267(2) Å for $\mathbf{1}^{\mathbf{OMe}}$ and 1.238(2), 1.273(3) Å for $\mathbf{1}^{\mathbf{H}}$) are comparable to other Cu^I-NO_2 complexes,[248] suggesting that binding to copper(I) and crystal packing dictate these bond lengths of the $^-NO_2$ ligand more than H-bonding interactions.

Another interesting feature of the solid state structures of $\mathbf{1}^{\mathbf{H}}$ and $\mathbf{1}^{\mathbf{OMe}}$ is the pyridine of the ligand arm engaged in only one O–HN interaction is not bound to copper. The ^{1}H NMR spectrum does not indicate an asymmetric binding of the three arms, suggesting that in solution, on the NMR time scale, these molecules are C_3-symmetric. The -NH proton resonance is also symmetric, suggesting equivalent the O–HN interactions are also symmetric on the NMR timescale. Even at low temperature (-80 °C), the -NH resonance of $\mathbf{1}^{\mathbf{H}}$ is not split, suggesting the molecule retains its symmetry in solution. This suggests that the asymmetry observed in the solid state structures are likely an effect of crystal packing.

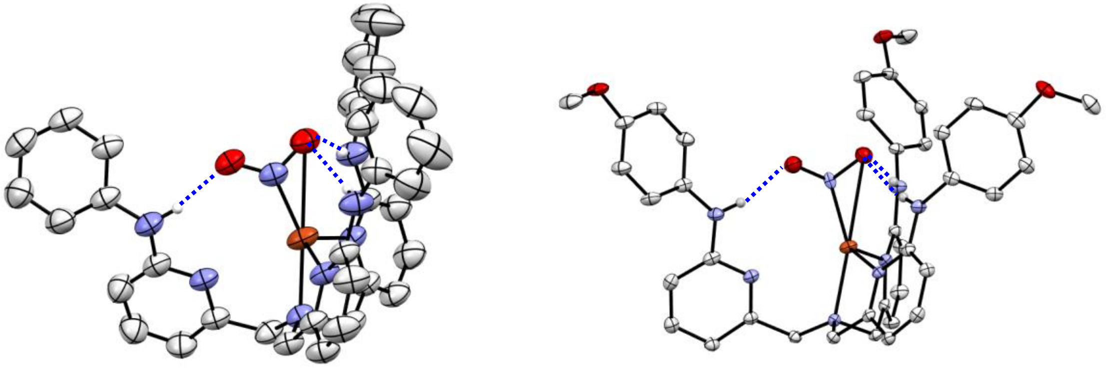

Figure 4.3 Crystal structures of $\mathbf{1}^{\mathbf{H}}$ and $\mathbf{1}^{\mathbf{OMe}}$ (50% ellipsoids). H-bonds shown as blue dashed lines.

The H-bonding to the $^-NO_2$ ligand in these complexes is reminiscent of the secondary sphere amino acid residues in CuNiR. We were interested in investigating the reduction of $^-NO_2$ to NO (g) using these complexes and proposed that due to the H-bonding interactions, weak acids should be able to induce the reduction to NO (g). Addition of pyridinium chloride (PyHCl) to a DCM/EtOH solution of $\mathbf{1^H}$ for 1h at room temperature resulted in a color change from bright yellow to dark green. Analysis of the headspace by gas IR revealed frequencies at 1904 and 1855 cm^{-1}, consistent with NO (g) evolution. EPR spectroscopy of the green solution from the reaction with $\mathbf{1^H}$ reveals a slightly distorted axial structure consistent with Cu^{II}. These results indicate to us that we have successfully reduced the nitrite *via* proton-couple electron transfer from the Cu^{I} and exogenous acid source. It is worth noting that a Cu^{II}-NO species is a possible product of this reaction, however this complex has not been synthesized to date; future exploration of this species may yield insight into the product of this protonation reaction.

4.2.2 Reactive complex: R = 3,5-$(CF_3)_2$

We concurrently attempted to synthesize a variant of **1** using ligand $L^{(CF3)2}$ – where the aniline variant forming the secondary sphere H-bonds has a 3,5-bis(trifluoromethyl) substitution pattern. The additional CF_3 group makes this variant a particularly strong H-bond donor, but the difference in substitution pattern makes comparing pK_a/H-bond strength by traditional methods (i.e. σ Hammet parameter) difficult. To better compare the H-bond donor strength of these complexes, we calculated the pK_a of the substituted anilines using density functional theory (B3LYP/6-31g). These values give us an idea of the degree of H-bond donor ability for the four substitute complexes compared to the unsubstituted -HNPh. We also must consider that as the N-H group becomes more acidic, it inherently changes the bond dissociation energy (BDE), resulting in stronger H-bond donors which can more readily transfer an H-atom (Table 4.1). We have previously observed this type of reactivity with the H_3tpa ligand which was deprotonated upon coordination and reduction of nitrite.

Table 4.1 Calculated p*K*$_a$ and experimental BDE values for substituted anilines

Aniline Substitution	**Calculated Relative p*K*$_a$***	**BDE (kcal/mol)**[†]
p-OMe	6.99	90.4
p-H	0.0	92.3
p-CF_3	-10.44	96.5
3,5-$(CF_3)_2$	-17.09	--

* DFT: B3LYP/6-31g, set *p*-H equal to 0.0. † Experimental values.[250]

Synthesis of $\mathbf{1}^{\mathbf{(CF3)2}}$ proceeded similarly to complexes $\mathbf{1}^{\mathbf{R}}$ (R = *p*-CF_3, H, OMe), however, this complex was particularly difficult to isolate in comparison. Upon isolation of the complex, it exhibited similar spectroscopic signatures, with the -NH resonance in the ^{1}H NMR shifted slightly more upfield from that in $\mathbf{1}^{\mathbf{CF3}}$, and similar N-H stretches in the IR spectrum. The $^-NO_2$ stretch is partially buried by large resonances but a weak resonance at 1317 cn^{-1} could be attributed to the antisymmetric $^-NO_2$ stretch and falls in line with the trend observed for the other three nitrite complexes.

This complex was observed to decompose in solutions at room temperature to a bright green species that was NMR silent. EPR spectroscopy clearly shows a copper(II) complex, and the corresponding ^{1}H NMR shows almost no diamagnetic material, suggesting the majority of the reaction has been oxidized. While no oxidant or exogenous acid was specifically added to this reaction, it is possible that weakly acidic residues could be responsible for inducing this reaction (which most likely proceeds through reduction of the $^-NO_2$ with evolution of NO. Such residues could be either water (trace, in solvent) or from dichloromethane. Switching from CH_2Cl_2 to non-polar solvents (benzene, toluene) and working at reduced temperatures enabled easier identification and solution characterization of the Cu^I(NO_2) complex, although we did continue to observe decomposition of this complex far more readily than the corresponding $\mathbf{1}^{\mathbf{H}}$ and $\mathbf{1}^{\mathbf{OMe}}$ complexes. While $\mathbf{1}^{\mathbf{CF3}}$ was not nearly as stable as $\mathbf{1}^{\mathbf{H}}$ or $\mathbf{1}^{\mathbf{OMe}}$, and would occasionally decompose in solution, once isolated, it was stable enough to work with, and obtain characterization and reactivity data. $\mathbf{1^{(CF3)2}}$ was far less stable, leading us to conclude that the strong H-bonds enabled even weakly acidic residues to act as a proton source for PCET reaction. This is reminiscent of the reactions observed by Moore et al. in our prior report[117] and suggests that H-bonding for stabilization of the Cu-NO_2 intermediate is sensitive to the H-bond strength: stronger H-bonds assist in the reduction of $^{-}NO_2$ and weaker H-bonds enable capture and stabilization of a η^1 N-bound NO_2.

4.3 Nitrite reduction from stable Cu^I-F complexes

4.3.1 Stable Cu^{I}FL^R complexes

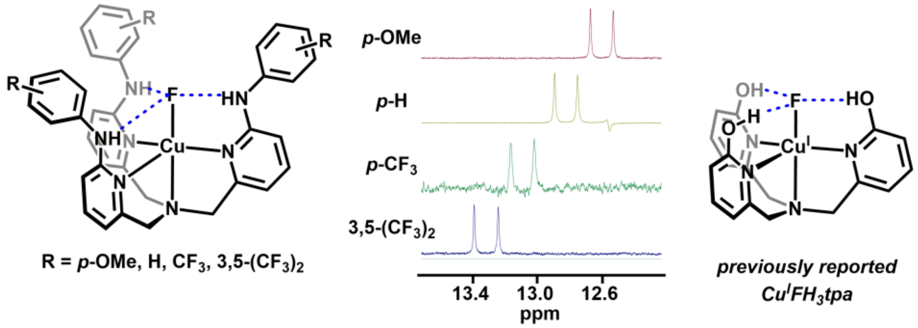

Figure 4.4 Structure of CuFL^R complexes, $\mathbf{2^R}$ (left), associated N-H resonances in the ^{1}H NMR spectra (center), and the previously reported Cu^{I}F complex (left, ref. 117). H-bonds shown as blue dashed lines.

In an effort to relate these studies to the prior work for nitrite reduction at Cu^I, we synthesized the analogous Cu(I)-F complexes, $\mathbf{2^R}$ (R = $(CF_3)_2$, CF_3, H, OMe) (Fig 4.4).[117] Stirring copper(I) iodide and L^R in acetonitrile followed by addition of cesium fluoride resulted in the formation of a new Cu^I complex. Analysis of complex $\mathbf{2^H}$ by ^{1}H NMR shows a symmetric, diamagnetic copper(I) complex. The upfield N-H resonance exhibits F-H coupling (CH_2Cl_2: 12.82 ppm, J = 57.0 Hz) due to the though-space interaction of the H-bond to fluoride. This same phenomenon is observed with the other three Cu^I-F complexes (Fig. 4.4 and Table 4.2). The ^{19}F NMR spectrum also reflects the changes in the ligands. A small, broad peak corresponding to the

Cu^{I}-F shifts downfield as the ligand becomes more electron-withdrawing; in the case of $\mathbf{2^{CF3}}$ and $\mathbf{2^{(CF3)2}}$, the broad peak is split due to interactions with the strong H-bonding with the L^{R} ligand. With this series of Cu^{I}FL^{R} complexes in hand, we proceeded to investigate the reaction with a previously developed silylnitrite compound.

Table 4.2 Key NMR resonances for complexes $\mathbf{2^{R}}$

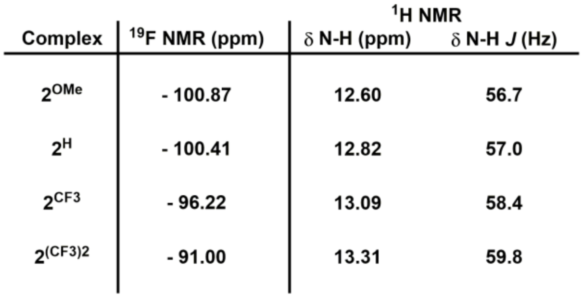

Complex	^{19}F NMR (ppm)	^{1}H NMR δ N-H (ppm)	 δ N-H *J* (Hz)
2^{OMe}	- 100.87	12.60	56.7
2^{H}	- 100.41	12.82	57.0
2^{CF3}	- 96.22	13.09	58.4
$2^{(CF3)2}$	- 91.00	13.31	59.8

4.3.2 Reactions with Ph_3Si-ONO

Prior work in our group with a Cu^{I}-F complex featuring strong secondary sphere H-bonds used a silyl reagent, triphenylsiliylnitrite (Ph_3Si-ONO), for the reduction of nitrite to NO (g). The reaction of Ph_3Si-ONO with $\mathbf{2^{H}}$ in CH_2Cl_2 resulted in the rapid formation Ph_3Si-F, confirmed by ^{19}F NMR, and a paramagnetic copper(II) species, which exhibited no ^{1}H NMR signals. Analogous reactions run in toluene with an internal standard revealed Ph_3Si-F was formed in 72% yield, and headspace analysis by gas IR spectroscopy revealed NO (g) was evolved. No other Cu^{I} species were observed in the reaction mixture.

An EPR spectrum of the Cu^{II} containing product from the reaction of $\mathbf{2^{F}}$ and Ph_3Si-ONO in CH_2Cl_2 exhibits a slightly distorted axial signal. When fit as a single species, the *g* values (2.16, 2.2, 2.01) are similar to the product from the reaction of $\mathbf{1^{H}}$ and H^{+} (g = 2.16, 2.18, 2.025), suggesting the same product results from the reduction of $^{-}NO_2$ at copper, which we would predict to be a Cu^{II}-OH species (Fig. 4.5).[117] However, it’s possible it could be overlapping from two species. To test this theory, we summed the fitted EPR spectra of the product of $\mathbf{1^{H}}$ + H^{+} and the oxidized Cu^{II}-F complex (**3^{H}**). The oxidized Cu^{II}-F species would be an unusual side product in this reaction but could feasibly be accessed by a disproportionation reaction of Cu^{I} to Cu^{II} and Cu^{0}. However, when the summed spectra of these two species are compared against the product of **2^{H}** and Ph_3Si-ONO in CH_2Cl_2, it is clear they are not the same species, suggesting that a single Cu^{II} species forms as the product, as observed in the reduction induced by addition of a proton source.

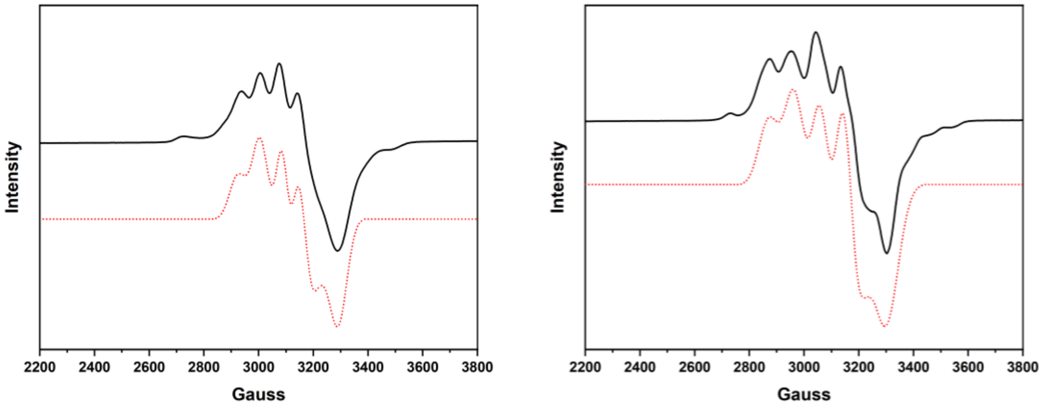

Figure 4.5 EPR spectra of reactions of Cu^{I} with $^{-}NO_2$, experimental (black) and fitted (red). Left: **1^{H}** + H^+ (CH_2Cl_2, 110 K); fitted parameters: g = 2.16, 2.18, 2.025; A = 120, 260, 30; freq. = 9.292. Right: **2^{H}** + Ph_3Si-ONO (CH_2Cl_2, 105 K); fitted parameters: g = 2.61, 2.2, 2.01; A = 180, 300, 20; freq. = 9.258.

The EPR spectrum from the reaction of **2^{H}** and Ph_3Si-ONO in toluene exhibits an axial signal (g values = 2.05, 2.24), which is consistent with a Cu^{II} species. The difference in g-values compared to the reaction in CH_2Cl_2 could be due to the presence of weakly acidic protons in the CH_2Cl_2, that enable formation of a Cu^{II}-OH, or the presence of $^{-}$Cl from pyrCl, which could form a Cu^{II}-Cl species *via* ligand exchange. In toluene, these species are not available, and so the slight changes in Cu^{II} signal could be due to the change in solvent. The geometry of the Cu^{II} species while frozen in solution should also be considered – in toluene, we would expect a fully trigonal pyramidal species, which would give rise to the axial species observed. In CH_2Cl_2, the presence of the weakly acidic -CH_2 or even the C-Cl group could be causing a slight distortion from the fully axial species, leading to differences in the spectra. We attempted to crystalize the products of both synthetic routes to better characterize the paramagnetic products but were unsuccessful.

Taken together, these results indicate that the $Cu^{I}FL^{H}$ complex is capable of reducing $^{-}NO_2$ from the silyl compound to NO (g) and oxidizing the copper center. The lack of observation of any other Cu^{I} species (i.e., $\mathbf{1^{H}}$) in solution suggests that this reduction proceeds through a different mechanism. Rather than a simple ligand exchange of ^{-}F and $^{-}NO_2$, followed by protonation to induce nitrite reduction, the data suggest a concerted proton coupled electron transfer (PCET) process takes place, with the proton source coming from either the -NH ligand or the surrounding solvent (Fig. 4.6) This is consistent with the prior report using this method for $^{-}NO_2$ reduction and indicates that the H-bond strength may be independent of the nitrite activation reaction.

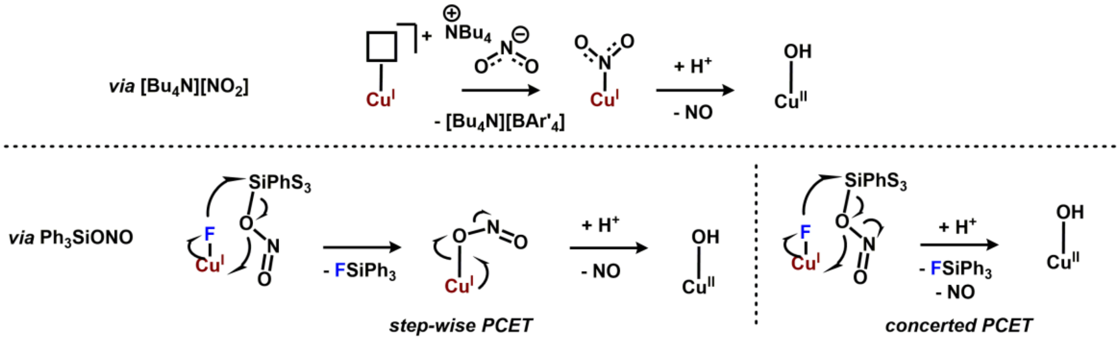

Figure 4.6 Proposed mechanisms for reduction of $^{-}NO_2$ with $Cu^{I}L^{H}$ precursors.

4.4 Electrochemical nitrite reduction

During the course of these studies, an in depth study was published on a related $Cu^{I}(NO_2)$TPA complex with an appended proton-responsive carboxylic acid group. This complex was capable of catalytically reducing $^{-}NO_2$ under electrochemical conditions in the presence of a proton source with a high Faradaic yield of NO (97.3%) and ~ 6 turnovers per hour. The initial studies showed a cathodic shift of the copper complex upon addition of excess $-NO_2$ and a catalytic wave in the CV upon addition of benzoic acid.[114] Intrigued by these results, we decided to test our H-bonding $Cu^{I}(NO_2)L^{H}$ complex for electrochemical reduction of nitrite (Fig. 4.7).

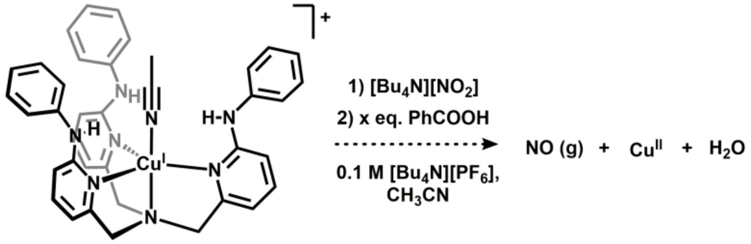

Figure 4.7 Reaction scheme for electrochemical reduction of $^{-}NO_2$ with $Cu^{I}(MeCN)L^{H}$ in the presence of benzoic acid.

When the $Cu^{I}L^{H}$ precursor is subjected to a cyclic voltammetry experiment in the presence of 45 eq. of $[NBu_4][NO_2]$ a reversible redox event is observed at (-0.67 V vs Fc). Addition of 5 equivalents of benzoic acid results in the growth of an anodic peak with an onset potential of -1.60 V and a maximum current at -2.17 V. Additional equivalents of benzoic acid (10 and 20 eq. total) resulted in enhancement of the peak at -2.17 V (Fig.4.8). The anodic peak shift to more reductive potentials by almost -1.35 V while the cathodic peak only shifts anodically by -0.18 V. This could be caused by coordination of the benzoic acid to the copper complex to form an octahedral species. The observed feature is likely proton reduction of the coordinated benzoic acid, which is shifted catholically from free benzoic acid due to coordination to copper. This feature was inconsistent with the background reaction of benzoic acid and $^{-}NO_2$, leading us to the conclusion that the electrochemical event is not nitrite reduction. When the copper-based redox event is isolated, it becomes reversible at -0.55 V and additional equivalents of benzoic acid do not result in a catalytic peak for nitrite associated with the copper, but only a slight anodic shift by 200 mV to -0.75 V in the reversible redox event. Compared to the obvious catalytic reduction of $^{-}NO_2$ the Symes group observed in their proton-responsive CuTPA system, our H-bonding complex does not seem to have similar capability for the electrocatalytic nitrite reduction.

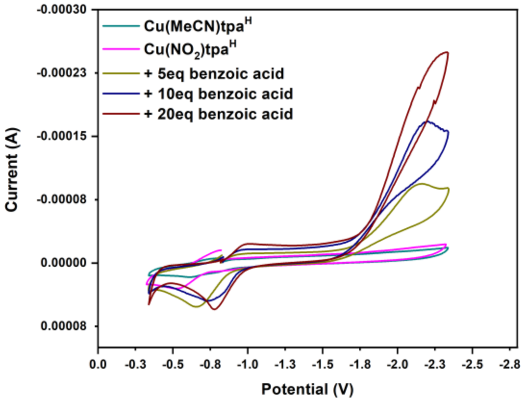

Figure 4.8 Cyclic voltammetry experiment with CuL^H and 50 eq. $^-NO_2$, with increasing benzoic acid concentration (0.1 M $[Bu_4N][PF_6]$ in CH_3CN).

4.5 Binding studies

In an effort to better understand the binding of nitrite to Cu^IL^H, especially in comparison to our prior work, where $^-NO_2$ binding was not observed, we investigated the binding affinity of nitrite, along with nitrate, triflate, and iodide (Fig. 4.9). Proton NMR experiments with **1^H** in the presence of 1-50 equivalents of the anion in question were run in acetonitrile at room temperature. The integration values obtained from each were used in the Thoradarson fitting program, which can be used to calculate association constants, K_a. For the purposes of these studies, and based on prior work with **1^H**, we used a 1:1 fitting model for the anions in question, using the C5 pyridine C-H doublet in the spectrum for the integrations.

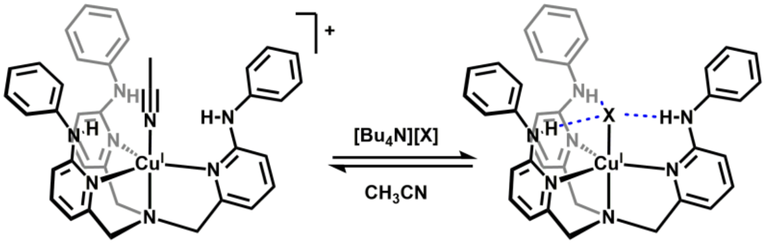

Figure 4.9 Binding equilibrium for Cu^IL^H with anionic ligands (X = $^-ClO_4$, ^-OTf, $^-NO_2$, $^-NO_3$, ^-I).

The calculated Ka values are displayed in Table 4.3. These values corroborate the very weak binding affinity of non-coordinating ions (^-OTf, $^-ClO_4$) as well as the strong binding affinity for halogens ($^-$I). Nitrate and nitrite for **1^H** both fall between these two extremes. When compared to the Ka value for Cu^ITPA with $^-NO_3$ acquired using the same experimental and calculation methods, we clearly see a drastic difference in the binding affinity for nitrate between **1^H** and Cu^ITPA, on the order of five orders of magnitude. The larger ΔG values for CuTPA vs. CuL^H indicates binding is disfavored without H-bonds. This direct comparison provides us with excellent calculated evidence of the influence the appended -HNPh groups in L^H have on the increasing binding affinity of ions to copper(I).

Table 4.3 Experimentally determined associations for anions with CuL^H in CH_3CN at room temperature.

Anion	**K_a**	**ΔG (kcal/mol)**
$^-ClO_4$	0.002	+3.48
$^-$OTf	0.653	+0.23
$^-NO_2$	1.780	-0.31
$^-NO_3$	**14.690**	**-1.46**
$^-$I	69.608	-2.30
$^-NO_3$ (TPA)	**0.001**	**+17.30**

* Final entry is for CuTPA for comparison.

4.6 Conclusions

We have shown that tunable, bulky secondary sphere H-bonding groups can enable capture of nitrite at copper(I). The H-bond strength directly influences the stability of the Cu^I-NO_2 complexes, with stronger H-bonds creating more reactive complexes which can decompose readily at room temperature due to their weak BDFE and subsequent PCET, and weaker H-bonds providing sufficient stabilization for crystallization. Addition of weak acids induces reduction of nitrite to NO (g), even in the stable complex **1^H**, which is detected by gas IR. Accessing $^-NO_2$ reduction *via* a Cu^I-F and a silylnitrite source results in immediate formation of a new Cu^{II} species and evolution of NO (g), similar to prior results in our group. Since we again do not observe any intermediates in this reaction, it suggests that the route mode of $^-NO_2$ binding to Cu^I in this system

(O-bound vs N-bound) directly effects the mechanism of nitrite reduction. Our attempts to electrocatalytically reduce nitrite using complex $\mathbf{1^{H}}$ were unsuccessful, pointing to the chemical stability of the nitrite complex imparted by the trifurcated H-bonds. Binding of $^{-}NO_2$ is energetically favorable based on the calculated K_a and G values, comparable to $^{-}NO_3$, which helps explain the stability of the complexes and the lack of electrocatalytic reduction.

Moving forward there are several directions this project could take. Based on the difference in stability of the Cu^{I}-NO_2 complexes based on H-bond strength, we are interested in probing the effect of pK_a on the reduction of nitrite. Based on the evidence of reactivity with the strong H-bonds in $\mathbf{1^{(CF3)2}}$ that led to decomposition over time in solution, we hypothesize that the strength of the acid necessary to induce the reduction of $^{-}NO_2$ should be lower for the complexes with stronger H-bonds. However, it's possible that the electronic effect the ligand substitution has on the complex (-OMe being more electron donating, $-CF_3$ being more electron withdrawing) could complicate the proposed trend in pK_a vs H-bond strength. Additional studies should also be performed using the Cu-F route for nitrite reduction as well. We did not investigate the solid state of the products of this reaction, and it would be helpful to perform additional low temperature UV-vis studies to interrogate any intermediates in the reduction of $^{-}NO_2$ to help us better identify the mechanism of nitrite reduction.

4.7 Acknowledgments

We thank the members of the Lehnert lab for helpful discussions about EPR, and the Lehnert lab for the use of SpinCount.

4.8 Experimental Details

4.8.1 General considerations:

All air- and moisture-sensitive manipulations were performed using standard Schlenk techniques or in an inert atmosphere glovebox with an atmosphere of purified nitrogen. The glovebox was equipped with a cold well designed for low temperature experiments as well as a −30 °C freezer for cooling samples and crystallizations. Solvents were purified using a Glass Contour solvent purification system through percolation through a Cu catalyst, molecular sieves, and alumina. Solvents were then stored over sodium and/or molecular sieves. Deuterated solvents were purchased from Cambridge Isotope Laboratories and used as received.

Caution! Perchlorates are potentially explosive and should be handled with care and on small scales.

Copper tetrakis(acetonitrile) perchlorate ($[Cu(MeCN)_4]ClO_4$), copper(I) iodide, cesium fluoride, tetrabutylammonium nitrite ($TBANO_2$), $Pd(OAc)_2$, 2,2′-Bis(diphenylphosphino)-1,1′-binaphthalene (BINAP), Cs_2CO_3, benzoic acid, tetrabutylammonium nitrate ($TBANO_3$), tetrabutylammonium perchlorate ($TBAClO_4$), tetrabutylammonium triflate (TBAOTf), and tetrabutylammonium iodide (TBAI) were purchased from commercial vendors and dried under vacuum before transferring to a nitrogen glovebox. Ferrocene was purchased from a commercial vendor and sublimed prior to use. Phenyltrimethylsilane and 3,5-bis(trifluoromethyl)aniline were dried, distilled, and stored over sieved prior to use. Copper tetrakis(acetonitrile) tetrakis(pentafluorophenyl) borate ($[Cu(MeCN)_4]BAr'_4$),[251] tris(6-phenylamino-2-pyridylmethyl)-amine (L^H),[22] tris(6-(4-trifluoromethylphenyl)amino-2-pyridylmethyl)amine (L^{CF3}),[22] tris(6-(4-methoxyphenyl)amino-2-pyridylmethyl)amine (L^{OMe}),[22] tribromo-tris(2pyridiylmethyl)amine (Br_3tpa), triphenyl silylnitrite (Ph_3Si-ONO),[117] and ferrocenium hexafluorophosphate ($FcPF_6$)[231] were synthesized according to literature procedures. Pyridine hydrochloride was prepared by adding a solution of HCl in Et_2O to pyridine in Et_2O at room temperature.

NMR spectra were acquired on Varian 400 MHz or 500 MHz spectrometers as indicated below. ^{1}H NMR spectra are referenced to non-deuterated internal solvent residuals and are reported in parts per million (ppm) relative to tetramethylsilane. ^{19}F NMR spectra are referenced to their respective ^{1}H spectra. Multiplicities are reported as follows: singlet (s), doublet (d), triplet (t), quartet (q). Coupling constants (*J*) are reported in Hz.

IR spectra were recorded on a Nicolet iS10 FT-IR spectrometer with an ATR accessory or KBr pellets as specified. Gas-phase IR spectra were collected using a Perkin-Elmer Spectrum BX spectrometer using a custom gas cell with an 11 cm path length and BaF_2 windows. Mass spectra were recorded on an Agilent 6230 TOF HPLC-MS with a liquid phase of 95% acetonitrile, 5% water, 0.1% formic acid. Electronic absorption spectra were recorded at ambient temperature in sealed 1 cm quartz cuvettes (as specified) or with a Hellma Analytics 661.200-QX quartz probe (0.5 cm pathlength) with a Varian Cary-50 spectrophotometer (resolution: <1.5 nm). Flash chromatography was performed on a Biotage Isolera One automated system using self-packed 25g columns. EPR spectra were collected on a Bruker EMX electron spin resonance spectrometer, with a Bruker 4102-ST cavity, at liquid N_2 temperatures in frozen solvent (specified below). The program SpinCount was used to model EPR spectra (using the Lehnert lab license).

Electrochemistry was performed with a Pinewave Wavenow potentiostat under a dinitrogen atmosphere with a glassy carbon working electrode, a platinum counter electrode, and a silver wire pseudo-reference electrode. Measurements were referenced against an internal ferrocene standard. Electrolyte, $[NBu_4][PF_6]$, was used in 0.1 M in CH_3CN or CH_2Cl_2 as indicated.

Single crystal data for **1^{H} and 1^{OMe}** were collected using a Rigaku AFC10K Saturn 944+ CCD-based X-ray diffractometer equipped with a low temperature device and a Micromax-007HF Cu-target microfocus rotating anode (λ = 1.54184 Å) operated at 1.2 kW power (40 kV, 30 mA).

The data were collected using CrystalClear 2.016.[252] The X-ray intensities were measured at 293(2) K (**1^{H}**) or (**1^{OMe}**) or with the detector placed at a distance 42.00 mm from the crystal. A total of 2800 images were collected with an oscillation width of 1.0° in w. The exposure times were 1 sec. for the low angle images, 3 sec. for high angle. Rigaku d*trek images were exported to *CrysAlisPro* 1.171.40.53 for processing and corrected for absorption.[253] The integration of the data yielded a total of 63736 (**1^{H}**) reflections to a maximum 2θ value of 69.353° (**1^{H}**) of which 7693 (**1^{H}**) were independent and 6534 (**1^{H}**) were greater than 2σ(I). The final cell constants were based on the xyz centroids of 7693 (**1^{H}**) reflections above 10σ(I). For **1^{OMe}**, the integration of the data yielded a total of 19670 (**1^{OMe}**) reflections to a maximum 2θ value of 68.923° (**1^{OMe}**) of which 6837 (**1^{OMe}**) were independent and 6619 (**1^{OMe}**) were greater than 2σ(I). The final cell constants were based on the xyz centroids of 6837(**1^{OMe}**) reflections above 10σ(I). Empirical absorption correction was applied using spherical harmonics, as implemented in the SCALE3 ABSPACK scaling algorithm. Refinement was performed using Olex[243] and the XL[242] refinement program. A Squeeze method was used on **1^{H}**, and Superflip applied to **1^{OMe}**.

4.8.2 Synthesis of $Cu(NO_2)L^R$ complexes (1^R)

Synthesis of 1^{H}. Ligand L^H (25.5 mg, 0.045 mmol) and $Cu(MeCN)_4BAr'_4$ (35.9 mg, 0.040 mmol) were combined CH_3CN (7 mL), and stirred at room temperature for 30 min. A solution of $TBANO_2$ (11.3 mg, 0.0146 mmol) in CH_3CN (2 mL) was added to the stirring copper solution. The dark yellow solution was stirred at room temperature for 30 min and was then dried under vacuum. The orange residue was washed with Et_2O, then extracted with CH_2Cl_2, filtered, and dried as a yellow-orange solid (22.8 mg, 92%). ^1H NMR (400 MHz, CD_2Cl_2, 25 °C) δ 9.02 (s, 3H), 7.42 (dd, *J* = 8.4, 7.2 Hz, 3H), 7.30 (m, *J* = 6.4 Hz, 12H), 7.04 (tt, *J* = 6.7, 2.0 Hz, 3H), 6.96 (d, *J* = 8.4 Hz, 3H), 6.64 (d, *J* = 7.2 Hz, 3H), 3.79 (s, 6H).

Synthesis of 1^{OMe}. Ligand L^{OMe} (10.4 mg, 0.0107 mmol) and $Cu(MeCN)_4BAr'_4$ (13.2 mg, 0.040 mmol) were combined CH_3CN (7 mL) and stirred overnight. A solution of $TBANO_2$ (4.2 mg, 0.0147 mmol) in CH_3CN (2 mL) was added and the reaction solution stirred for 1 hr. The solution was dried, washed with Et_2O and dried, then extracted with CH_2Cl_2 and dried as a yellow solid. ^1H NMR (400 MHz, CH_2Cl_2, 25 °C) δ 8.79 (s, 3H), 7.36 (t, *J* = 8.1 Hz, 3H), 7.18 (m, 6H), 6.85 (m, 6H), 6.72 (d, *J* = 8.5 Hz, 3H), 6.57 (d, *J* = 7.1 Hz, 3H), 3.75-3.77 (overlapping singlets, 15H).

Synthesis of 1^{CF3}. Ligand L^{CF3} (10.1 mg, 0.0132 mmol) and $Cu(MeCN)_4BAr'_4$ (11.4 mg, 0.0384 mmol) were combined in toluene (3 mL), stirred and frozen for 30 min. A solution of $TBANO_2$ (3.6 mg, 0.0125 mmol) in toluene (2 mL) was added and the yellow solution was stirred, then frozen for 1h. The solution was then thawed to room temperature, stirred 1 h, then dried under vacuum. The residue was dissolved in Et_2O, triturated with pentane, decanted, and the yellow oily solid was dried. ^1H NMR (400 MHz, CH_2Cl_2, 25 °C) δ 9.34 (s, 3H), 7.50 (overlapping d/t, 12H), 7.31 (d, *J* = 8.3 Hz, 6H), 7.05 (d, *J* = 8.4 Hz, 3H), 6.71 (d, *J* = 7.3 Hz, 3H), 3.83 (s, 6H). ^{19}F NMR (400 MHz, CH_2Cl_2, 25 °C) δ -62.16 (CF_3), -132.97, -163.68, -167.46 (trace BAr'_4).

Synthesis of $L^{(CF3)2}$. Br_3tpa (202 mg, 0.4760 mmol), $Pd(OAc)_2$ (20 mg, 0.0437 mmol), BINAP (30 mg, 0.0644 mmol), and Cs_2CO_3 (747 mg, 2.8485 mmol) were combined in a 20 mL vial equipped with a stir bar. Toluene (20 mL) and 3,5-bis(trifluoromethyl)aniline (539 μL, 4.2706 mmol) were sparged with N_2, then transferred quickly to the vial, which was capped and stirred overnight at 100 °C. The solution turned a bright red solution as the reaction proceeded. After 18 h, the solution was removed from heat, cooled, filtered through Celite, and extracted with CH_sCl_2 (10 mL). The solution was dried to a red-brown oil which was dry loaded on a silica gel column, and a flash column was run on the Biotage (9 CV 6% EtOAc/DCM, ramp to 100% EtOAc over 7 CV). Fractions 6-16 were combined, and the solvent removed to leave an orange oil. The oil was dissolved in hox hexanes and recrystallized at -30 °C in the freezer overnight. The mother liquor was decanted and the off-white solid dried (119 mg, %). ^{1}H NMR (400 MHz, CD_2Cl_2, 25 °C) δ 8.12 (s, 6H), 7.55 (t, *J* = 7.8 Hz, 3H), 7.42 (s, 3H), 7.19 (d, *J* = 7.5 Hz, 3H), 6.74 (s, 3H), 6.65 (d, *J* = 8.2 Hz, 3H), 3.87 (s, 6H). ^{19}F NMR (400 MHz, CH_2Cl_2, 25 °C) δ -63.43.

Synthesis of $\mathbf{1^{(CF3)2}}$. $L^{(CF3)2}$ (9.9 mg, 0.0102 mmol) was stirred with $Cu(MeCN)_4BAr'_4$ (17.5 mg, 0.0193 mmol) were stirred in C_6H_6 (5 mL) for 2 min at room temperature before being frozen at -30 °C. A solution of $TBANO_2$ (6.3 mg, 0.0218 mmol) in C_6H_6 (2 mL) was frozen at -30 C. The two solutions were combined after just thawing, stirred for 1 min, then frozen for 30 min. The solution was then thawed to room temperature and stirred for 1.5 h. The solvent was removed by vacuum, leaving a yellow residue, which was then redissolved in CH_2Cl_2, and dried to a yellow solid (a mix of $\mathbf{1^{(CF3)2}}$ and $TBABAr'_4$). ^{1}H NMR (400 MHz, CH_2Cl_2, 25 °C) δ 9.449 (s, 3H), 7.69 (s, 6H), 7.55 (t, *J* = 7.8 Hz, 3H), 7.45 (s, 3H), 6.99 (d, *J* = 8.4 Hz, 3H), 6.80 (d, *J* = 7.4 Hz, 3H), 3.88 (s, 6H). ^{19}F NMR (400 MHz, CH_2Cl_2, 25 °C) δ -63.58 (3,5-$(CF_3)_2$).

4.8.3 Synthesis of $CuFL^R$ complexes (2^R)

Synthesis of $\mathbf{2^H}$. A solution of L^H (10.2 mg, 0.0461 mmol) and CuI (3.8 mg, 0.0404 mmol) was stirred in CH_3CN (5 mL) for 30 min. CsF (3.5 mg, 0.0231 mmol) was added and the solution was stirred an additional 5 h. An orange solid precipitated, the reaction solution was filtered, and the solid was extracted with CH_2Cl_2 and dried to obtain a yellow solid (8.8 mg, 78%). ^{1}H NMR (400 MHz, CH_2Cl_2) δ 12.82 (d, *J* = 57.0 Hz, 3H), 7.37 – 7.31 (m, 9H), 7.28 (t, *J* = 7.7 Hz, 6H), 6.99 (dd, *J* = 8.1, 4.8 Hz, 6H), 6.47 (d, *J* = 7.1 Hz, 3H), 3.81 (s, 6H). ^{19}F NMR (400 MHz, CH_2Cl_2) δ -100. 14 (Cu-F).

Synthesis of $\mathbf{2^{OMe}}$. A solution of L^{OMe} (12.2 mg, 0.0187 mmol) and CuI (3.0 mg, 0.0158 mmol) was stirred in CH_3CN (5 mL) for 30 min. CsF (3.5 mg, 0.0231 mmol) was added and the solution was stirred overnight. A yellow solid precipitated, the reaction solution was filtered, and the solid was extracted with CH_2Cl_2 and dried to obtain a yellow solid (5.9 mg, 51%). ^{1}H NMR (400 MHz, CH_2Cl_2) δ 12.60 (d, *J* = 56.7 Hz, 3H), 7.29 (dd, *J* = 8.5, 7.1 Hz, 3H), 7.22 (d, *J* = 6.6 Hz, 3H), 6.90 – 6.73 (m, 9H), 6.40 (d, *J* = 7.1 Hz, 3H), 3.78 (s, 6H), 3.76 (s, 9H). ^{19}F NMR (400 MHz, CH_2Cl_2) δ -100.81 (Cu-F).

Synthesis of 2^{CF3}. A solution of L^{CF3} (10.9 mg, 0.0142 mmol) and CuI (2.3 mg, 0.0121 mmol) was stirred in CH_3CN (5 mL) for 1 h. CsF (2.0 mg, 0.0132 mmol) was added, and the solution was stirred overnight. A yellow solid precipitated, the reaction solution was filtered, and the solid was extracted with CH_2Cl_2 and dried to obtain a yellow solid (8.8 mg, 85%). ^{1}H NMR (400 MHz, CH_2Cl_2) δ 13.09 (d, *J* = 58.4 Hz, 3H), 7.48 (q, *J* = 10.3, 9.3 Hz, 15H), 7.1363 (d, *J* = 8.5 Hz, 3H), 6.59 (d, *J* = 7.1 Hz, 3H), 3.87 (s, 6H). ^{19}F NMR (400 MHz, CH_2Cl_2) δ -62.01 (CF_3), -96.22 (Cu-F).

Synthesis of $2^{(CF3)2}$. A solution of $L^{(CF3)2}$ (10.0 mg, 0.0103 mmol) and CuI (1.9 mg, 0.0100 mmol) was stirred in CH_3CN (5 mL) for 1 h. CsF (2.2 mg, 0.0145 mmol) was added and the solution was stirred an additional 1 h. The solution was dried, solid was extracted with CH_2Cl_2, filtered, and dried to obtain a yellow solid (14.9 mg). ^{1}H NMR (400 MHz, CH_2Cl_2) δ 13.31 (d, *J* = 59.8 Hz, 3H), 7.83 (d, *J* = 1.5 Hz, 6H), 7.57 – 7.49 (m, 3H), 7.39 (d, *J* = 1.9 Hz, 3H), 7.12 (d, *J* = 8.4 Hz, 3H), 6.67 (d, *J* = 7.3 Hz, 3H), 3.92 (s, 6H). ^{19}F NMR (400 MHz, CH_2Cl_2) δ -63.79 (3,5-$(CF_3)_2$), -91.08 (Cu-F).

Synthesis of 3^H. A solution of 2^H (8.2 mg, 0.0127 mmol) was dissolved in CH_2Cl_2 (5 mL) and a solution of $FcPF_6$ (4.5 mg, 0.0136 mmol) in CH_2Cl_2 (1 mL) were combined at room temperature and stirred for 10 min. EPR (CH_2Cl_2, 110 K, Freq. = 9.336) g = 2, 2.2, 2.24. A = 220, 300, 280.

4.8.4 Reactivity Studies

Reactions of 1^{R} with H^{+}.

1^{H}: In a 20 mL vial sealed with a septum, complex **1^{H}** (18.6 mg, 0.0276 mmol) was dissolved in a 50/50 solution of EtOH/CH_2Cl_2 and stirred for 20 min. Pyridine hydrochloride (3.3 mg, 0.0286 mmol) was dissolved in EtOH and injected into the copper solution via syringe and the reaction stirred for 1 h at room temperature. The solution changed from bright yellow to brown to green. The headspace of the vessel was evacuated into a gas IR cell *via* a needle and analyzed. EPR spectra of the green solution were obtained in frozen CH_2Cl_2. IR (gas). 1904, 1851 cm^{-1}. EPR (CH_2Cl_2, 110 K, freq. = 9.292) g = 2.16, 2.18, 2.025 A = 120, 260, 30.

1^{OMe}: In a 20 mL vial sealed with a septum, complex **1^{OMe}** (4.8 mg, 0.006 mmol) was dissolved in a 50/50 solution of EtOH/CH_2Cl_2 and stirred for 20 min. Pyridine hydrochloride (0.9 mg, 0.008 mmol) was dissolved in EtOH and injected into the copper solution via syringe and the reaction stirred for 1 h at room temperature. The solution changed from bright yellow to brown to green. The headspace of the vessel was evacuated into a gas IR cell *via* a needle and analyzed. EPR spectra of the green solution was obtained in frozen CH_2Cl_2. IR (gas). 1910, 1853 cm^{-1}.

Reactions of 2^{R} with Ph_3Si-ONO.

In CH_2Cl_2: Complex **2^{H}** (8.1 mg, 0.0108 mmol) was stirred in CH_2Cl_2 (5 mL) in a 20 mL vial sealed with a septum. A solution of Ph_3Si-ONO (3.8 mg, 0.0124 mmol) in CH_2Cl_2 (1 mL) was added via syringe and stirred for 1 h at room temperature. At this time a sample was taken from the headspace for IR analysis. The solvent was then removed under vacuum and the residue was redissolved in 3.0 mL to acquire a UV-vis spectrum. ^{19}F NMR (CH_2Cl_2): δ -170.08 ppm (Ph_3Si-F). IR (gas): 1905, 1850 cm^{-1}. EPR (CH_2Cl_2, 105 K, Freq. = 9.258) g = 2.16, 2.2, 2.01. A = 180, 300, 20.

In toluene: Complex $\mathbf{2^H}$ (6.8 mg, 0.0105 mmol) was stirred in toluene (8 mL, passed through alumina) in a 20 mL vial. A solution of Ph_3Si-ONO (3.5 mg, 0.0115 mmol) in toluene (2 mL, passed through alumina) was added and the solution stirred at room temperature for 1 h. ^{19}F NMR was taken with an internal standard (PhF, 10 eq), with formation of Ph_3Si-F in 94% yield. ^{19}F NMR (CH_2Cl_2): δ -170.08 ppm (Ph_3Si-F). EPR (toluene, 120 K, freq. = 9.272) g = 2.05, 2.24 A = 50, 480.

4.8.5 Attempted electrocatalytic reduction of $^-NO_2$

With L^H: L^H (2.2 mg, 0.0039 mmol) and $Cu(MeCN)_4BAr'_4$ (3.2 mg, 0.0035 mmol) were stirred in electrolyte (5.0 mL, 0.1 M $TBAPF_6$, CH_3CN) and an initial CV scan obtained. $TBANO_2$ (51 mg, 0.1789 mmol, 21 eq) was added and another CV taken. Benzoic acid was added in portions to the solution and a CV was taken after each addition (5 eq: 2.9 eq; 10 eq: 3.3; 20 eq: 5.8 mg).

With L^{CF3}: L^{CF3} (2.0 mg, 0.0026 mmol) and $Cu(MeCN)_4BAr'_4$ (2.6 mg, 0.0029 mmol) were stirred in electrolyte (5.0 mL, 0.1 M $TBAPF_6$, CH_3CN) and an initial CV scan obtained. $TBANO_2$ (37 mg, 0.1283 mmol, 19 eq) was added and another CV taken. Benzoic acid was added to the solution in portions and a CV was taken after each addition (5 eq: 1.5 eq; 10 eq: 1.7; 20 eq: 3.2 mg).

With L^{OM3}: L^{OMe} (2.3 mg, 0.0035 mmol) and $Cu(MeCN)_4BAr'_4$ (2.8 mg, 0.0031 mmol) was stirred in electrolyte (5.0 mL, 0.1 M $TBAPF_6$, CH_3CN) and an initial CV scan obtained. $TBANO_2$ (43 mg, 0.1491 mmol, 20 eq) was added and another CV taken. Benzoic acid was added to the solution in portions and a CV was taken after each addition (5 eq: 1.8 eq; 10 eq: 1.7; 20 eq: 3.8 mg).

4.8.6 CuL^HX Binding Studies

General procedure: A CuL^H stock solution was prepared: L^H (1 eq) and $Cu(MeCN)_4BAr'_4$ (2 eq) in 7.0 mL CH_3CN, stirred for 20 min (CuL^H C = 0.005 M). Speraately, a $TBANO_2$ stock solution was prepared: $TBANO_2$ (0.50 M in CH_3CN). Use autopipette to dispense CuL^H and $TBANO_2$ into a screwcap NMR tube, along with 5.0 µL (0.029 mmol) PhTMS as an internal standard. See table below for ratios of CuL^H stock and TBANO$_2$ stock (total volume for each: 600 µL). ^{1}H NMR data was collected for each sample at room temperature (25 °C). A spectrum of CuL^H with PhTMS internal standard was used to obtain a 0 eq point.

Table 4.4 Sample dilution of Cu^{I}L^H and TBAX for binding coefficient experiment

Eq. $^-NO_2$	**Vol. (µL) $^-NO_2$ stock**	**Vol. (µL) CuL^H stock**
50	300 (0.15 mmol)	100
30	150 (0.075 mmol)	450 (0.0025 mmol)
23	120 (0.06 mmol)	480 (0.0026 mmol)
16	90 (0.045 mmol)	510 (0.0028 mmol)
10	60 (0.03 mmol)	540 (0.0029 mmol)
5	30 (0.015 mmol)	570 (0.0031 mmol)
4	24 (0.024 mmol)	576 (0.0031 mmol)
3	18 (0.009 mmol)	582 (0.0032 mmol)
2	12 (0.006 mmol)	588 (0.0032 mmol)
1	6 (0.003 mmol)	594 (0.0032 mmol)

This procedure was repeated for each of the following anions using the listed concentrations of TBAX solution in CH$_3$CN.

TBAClO$_4$: 0.51 M; TBAOTf: 0.52 M; TBANO$_3$: 0.50 M; TBAI: 0.51 M

For the control complex CuTPA, the same procedure was performed using TBANO$_3$ (0.51 M) for comparison of K_a values.

Calculations for K_a. The Thordarson fitting program[254] was used to calculate K_a. Fitting1to1nmr2 was used for all analyses.

4.8.7 DFT calculations

Calculations were performed using the Gaussian 09 suite.[255] Calculations of all compounds were performed using the B3LYP functional and an ultrafine integration grid for all atoms. Optimizations were performed in the solvent phase (CH$_2$Cl$_2$) with the 6-31g(d) basis set for all atoms followed by vibrational frequency analysis to confirm that local minima were obtained through the absence of imaginary vibrational frequency modes.[256] The dissociation constants for H-NHPhR (R = p-OMe, p-H, p-CF_3, and 3,5-$(CF_3)_2$) were calculated using the following equation:

$$\text{NH disso.} = (\text{NH} + Et_2OH^+) - (NH_2^+\ Et_2O)$$

The values were then converted to kcal/mol to give a normalized difference in the dissociation compared to the control, protonated Et_2O. The values were normalized relative to one another, with p-H as the zero point, for comparison of the electronic effects on the N–H bond strength, and the subsequent strength of -NH…X H-bonding interactions.

-

Chapter 5 Conclusions

5.1 Summary and conclusions

This thesis has investigated the effects of secondary sphere H-bonding interactions on the stability and reactivity of transition metal complexes across multiple oxidation states and small molecules. Broadly, the synthesis and characterization of these complexes, as well as the accompanying reactivity studies help inform us on the influence sterically bulky H-bonding groups such as -NHPh can have for small molecule activation. By taking cues from enzyme active sites, including lipoxygenase and copper nitrite reductase, and incorporating tunable H-bonding groups in our ligand platform, we have pushed the field forward in regard to using reductively stable H-bond donors to capture, reduce, and stabilize key intermediates in biologically relevant small molecules. By understanding the limits of this ligand platform's tolerance for oxidation state changes and preferences for substrate interactions and binding/reduction events, we can better tune these or related transition metal complexes for productive reactivity of small molecules.

In Chapter 2, we investigated a series of Ni complexes featuring ligand L^H, which was established to be reductively stable at low potentials. Chemical reduction yielded the low valent nickel(I) halide complexes which were adequately stable for isolation and characterization, including the first crystal structure of a Ni^I complex featuring intramolecular H-bonding interactions (Fig. 5.1). Subsequent studies found that the low valent species was adept at fluoride atom abstraction and could undergo fluoride transfer reactions to a range of fluorine containing substrates. Compared against an analogous Ni^ITPA complex without H-bonds, the stability and selective reactivity of the H-bonding complexes is significantly improved. This study gives important insight into the stability of the -NHPh H-bonding group, even under strongly reducing conditions, and its utility for the stabilization of otherwise reactive species.

The results of our syntheses and experiments in Chapter 2 suggest that secondary sphere H-bonding groups could be more broadly useful in the isolation of a range of oxidation states, including low-valent complexes. Importantly, we note that the highly sensitive nature of the Ni^{I} complexes (to temperature, solvent, and oxygen) is suggestive of why such monomeric low valent nickel species have been notoriously difficult to isolate.[155] We suggest that the isolation of these complexes is enabled in two ways: (1) the halide is trapped close to the metal by the H-bonding groups, preventing it from dissociating or otherwise decomposing, and (2) the pre-organization of the -NH groups in H-bonding interactions with the halide prevents decomposition of the ligand. Such secondary sphere H-bonds can pull electron density away from the metal center, allowing for addition of electrons *via* reduction, however without that interaction to alleviate the potency of the reduction, we propose such reduction would be unsuccessful. Based on these conclusions, and the short lifetime of the dehalogenated species even at low temperatures, we hypothesize that isolation of other low-valent species may require pre-organization in order to prevent decomposition.

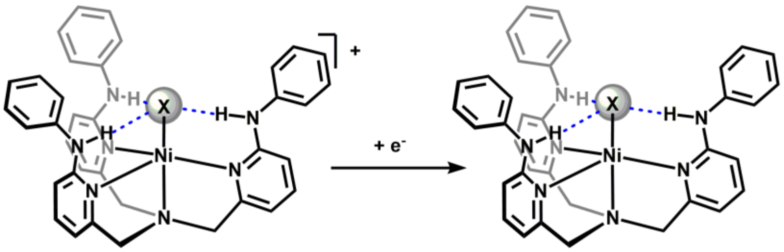

Figure 5.1 Reductively stable L^{H} supports formation of new H-bonded nickel(I) complexes.

Ongoing work in the literature has yet to support other examples of similar low-valent nickel complexes featuring H-bond donors. The current literature is still mainly focused on tuning the electronic properties of the supporting ligand scaffold to characterize and/or isolate nickel(I) species. Recently, a new nickel(I) bis-NHC complex was reported for its unusual insensitivity to geometric distortions, of which there had only been one other similar example.[257-258] Other groups have reported new ligands featuring strong σ donor groups for stabilization of the low valent species,[259] including a system that uses a redox-active ligand to access a Ni^{I}-Br species which is active for C-C bond forming reactions *via* SET.[260] A nickel(I) complex supported by a PNP-type pincer ligand was recently reported for its HAT reactivity *via* a cooperative ligand backbone (de)protonation pathway. Investigation into the effect of solvation of these systems suggests the Ni^{II} species is more stable, although the Ni^{I} should be stable enough for other reactivity.[261] Based on our work and that of the most current literature, using electron rich, proton- or redox-responsive, and/or weak H-bond containing ligands with nickel(I) complexes may be the most advantageous for the characterization and study of reactivity with these compounds.

In Chapter 3, we established that the same L^{H} could be used to access high valent intermediates in dioxygen activation using a coordinatively unsaturated iron(II) precursor, $[Fe(MeCN)_2L^{H}](BAr''_4)_2$ (**3.4**). We established that we could cleanly synthesize and characterize the product of O_2 activation, the Fe^{III}-OH species. Reactions with O_2 and **3.4** resulted in the formation of an intermediate which we have identified as an Fe^{IV}-oxo species by UV-vis spectroscopy (Fig. 5.2), parallel synthesis with an OAT reagent, and reactivity studies. The terminal Fe^{III}-OH is capable of hydroxyl radical rebound reactions. Reactions of Fe^{II}TPA complexes with O_2 do not form any high-valent intermediates on the same time scale as our FeL^{H} system. Additionally, the authentic unsubstituted Fe^{II}(OH)TPA system does not perform hydroxyl radical transfer reactions at a similar rate to $Fe^{II}(OH)LH$. The necessity of H-bonds, as opposed to steric congestion, for the activation of O_2 was supported by reactions using a related $Fe^{II}TPA^{OPh}$ complex, which showed no evidence of high valent intermediates or any reactivity with dioxygen. We've gained insight into the necessity of H-bonding for the activation of O_2; the stabilization of the intermediates lowers the kinetic barrier for bond cleavage, enabling reduction and subsequent reactivity. This should enable us to further this study by performing kinetics studies to determine how H-bonding directly affects the HAT reaction in comparison to other species without H-bonds; rates of the subsequent transfer steps will also be evaluated, as our early results suggest that rather than enhancing reactivity, the H-bonds slow the –OH transfer reactivity once the Fe^{III}-OH is formed. Together, this data will help us better understand the mechanism of oxidation reactions in this system.

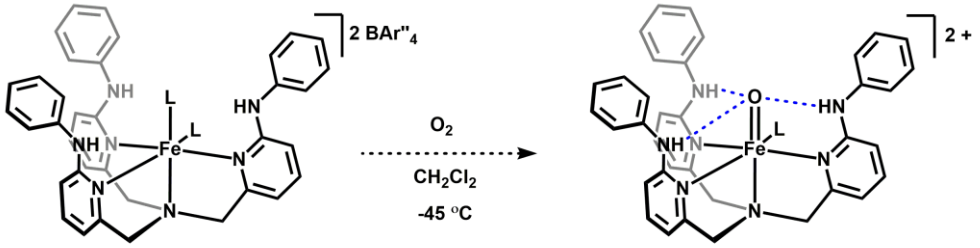

Figure 5.2 Proposed iron(IV)-oxo intermediate observed from O_2 activation.

High valent oxygen-containing iron complexes continue to be prevalent in the literature for their implications as models for a variety of non-heme iron enzymes including α-ketoglutarate and mono- and dioxygenases. Iron-oxo complexes are typically derived from chemical reagents (i.e., PyO, NMO, PhIO, etc), rather than O_2. Much of the current literature is focused on characterization of high valent iron-oxo species using new ligand frameworks or on HAT reactivity and understanding the mechanisms of known Fe^{IV}-oxo species. A recent report from 2021 introduced a new ligand platform for the isolation and characterization of iron-oxo species, specifically an Fe^{III}-oxo supported on with a bulky tris(carbene)borate ligand capable of HAT from toluene and hydrocarbon dehydrogenation.[262] Another recent paper reported on the ability to direct selectivity of C-H activation by an iron-oxo by adding a radical mediator.[263] Finally, another recent report of a series of sterically bulky pentadentate ligand included the solid state structure of a high-valent iron-oxo; the bulky ligand was deemed critically important for the formation and stability of the oxo species, although the differences in electronic properties of the ligands studied were implicated as the reason for divergent reactivity for HAT.[264] This small sampling of the current scope of high valent iron-oxo literature gives insight into areas of focus for the future of this project. The electronic properties of the ligand may influence the reactivity of the complexes, particularly when comparing high and low spin systems; the steric protection around the iron-oxo group can play an important role in enabling the isolation of these high valent species; and the reactivity of O_2 activation for the direct formation of iron-oxos is still under development and worth deeper investigation. Of note, only a handful of other groups have recently reported new iron-oxos or related species with secondary sphere H-bonding groups, suggesting that we may be able to access new studies for O_2 activation with the system reported here.

Finally, in Chapter 4, we examined the effect of changing H-bond strength on the reduction of nitrite using a series of copper(I) complexes. Changing the substitution of the-NHPh group of L^R from electron donating (low pK_a, higher BDFE) to electron withdrawing (high pK_a, lower BDFE) results in a change in the stability of the corresponding Cu^I-NO_2 complexes: using L^{OMe} and L^H results in stable complexes, which can be easily isolated and characterized. More electron withdrawing complexes with ligands L^{CF3} and $L^{(CF3)2}$ are much more difficult to synthesize and isolation is difficult, likely due to the smaller BDFE, which enables intramolecular PCET to the bound nitrite. Reactions of the stable nitrite complexes with H^+ induced NO (g) release and oxidation to Cu^{II}, as expected for the reduction of nitrite. We switched to more stable Cu^I-F precursors, which reactivity studies showed were also capable of rapidly reducing nitrite without proceeding through an observable intermediate (Fig. 5.3). This reactivity agrees with prior work in our group that used a Cu^{I}-F precursor with strong H-bond donor groups which could reduce $^{-}NO_2$, with no intermediates observed. The changes in the $^{-}NO_2$ interactions with the H-bonding complexes demonstrate the stark differences in reactivity afforded by changing the H-bond strength of in the secondary coordination sphere, as well as the source of small molecules for activation and give us insight into the effects the variation in H-bond strength may have on the stabilization and subsequent reactivity of other ML^{H} complexes.

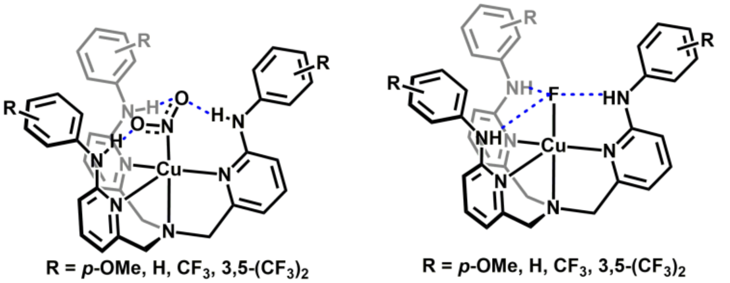

Figure 5.3 Copper(I) complexes featuring L^{R} ligands with vary H-bond strength.

The field of nitrite reduction chemistry is still of broad scientific interest, with a variety of different methods for inducing the formation of NO (g) currently being explored. Multiple reports in recent years have used electrochemical methods for the reduction.[113-114] Parallels can be drawn between these studies and the injection of an electron in to the catalytically active Cu^{II} center from the distant Cu^{I} electron donor site. Other work has focused on secondary sphere effects, including both H-bond donors[265] and exogenous Lewis acids.[266-267] Notably, other groups are moving to use iron in these model systems due to the activity of cytochromes and other non-heme iron enzymes for nitrite reduction. As is, the work in Chapter 4 remains relevant in the broader literature for the characterization of copper-nitrite complexes, while also offering potentially interesting routes for study regarding the mechanism of nitrite reduction. Switching to the related iron(II) complexes may offer a new route towards better understanding the effect of the tunable H-bond donors on the reduction of nitrite.

Figure 5.4 Summary of advantages of using complexes with L^H for small molecule activation.

Collectively, the results of experiments using Ni, Cu, and Fe provide a new approach to the use of the L^H ligand – accessing not just stable low-valent complexes but also high-valent species as well. This work has highlighted the key role H-bonding can play in the capture of intermediates and activation of a variety small molecules (Fig. 5.4). Moving into the future, we hope to expand on the work already described to help further inform the scientific community of the importance of H-bonding in synthetic inorganic systems.

5.2 Future directions and outlook

The work in this thesis has demonstrated the importance of H-bonds for activation of biologically relevant small molecules, including O_2 and $^-NO_2$. The use of these L^R ligands, with their modular construction, allows us to change the pK_a/BDFE of the H-bond donors and thus interrogate the effect the H-bond strength has on stability and subsequent reactivity. To date, we have been able to work with the "Goldilocks" of this ligand set, L^H, wherein we observe both reductive and oxidative stability of the ligand and reap the benefits of intramolecular -NH…X H-bonds, while still observing reactivity of the resulting complexes. We have observed that by tuning the ligand to provide stronger H-bonds, we enter a regime where PCET is possible, and actually so rapid that it prevents detailed studies of the resultant complexes. On the other hand, switching the -NH group for an -O group without H-bond donor capability, but an otherwise identical ligand, results in lack of reactivity for small molecule activation. While we envision continued efforts to use the established systems reported here with changes in H-bond donor strength to interrogate changes in complex stability and reactivity, we also recognize that such studies maybe complicated by the ability for PCET to occur.

Results from the Ni-F experiments suggest that SET reactions are induced by the low-valent nickel(I) complexes. However, the dehalogenation route to access the coordinatively unsaturated species did not result in C-F bond cleavage in benzylic or aromatic systems. We attributed this to the strong BDEs of these bonds (> 100 kcal/mol), one way to bias this reaction might be to switch to stronger H-bond donor ligands (L^{CF3}, perhaps). However, this could present two separate issues: the ligand itself, with weaker N-H bonds, might undergo reduction/decomposition in the presence of the strong reductant, and any $-CF_3$ substituents could compete with the C-F substrates for defluorination. It's also possible that this system is simply not reducing enough to access the potentials required for C-F activation. Prior work using reducing metals for benzylic C-F bond cleavage uses excess of Mg^0 in the presence of a F-atom acceptor to induce the SET and fluoride transfer.[268] Attempts to use a Ni^0 precursor to access even lower oxidation states were unsuccessful, which may mean a new route to access C-F bond cleavage may be necessary.

The results of the substrate oxidation reactions with the Fe^{IV}-oxo species are curious, as they not only show bias towards HAT reactions, but the transfer of the oxygen atom to the H-abstracted species appears hindered by the H-bonding groups (the C-C coupled product is excellent evidence of this). Tuning the H-bond strength of complex by modulating L^R substitution should enable us to probe the effect on the HAT reactivity. We would hypothesize that weaker H-bonds to the Fe-oxo intermediate would more readily transfer the O atom, while stronger H-bonds would slow that transfer even further, and thus the product distribution of cyclohexene oxidation would change as a function of H-bond strength. The issue of H-bond strength compared to BDFE may once again come into play if the N-H bond is weak enough to induce PCET reactions to the high valent intermediates of O_2 activation and outcompete the substrate. Investigating the rate of HAT versus subsequent OAT/hydroxyl radical transfer can further inform us of the role the H-bond donors play in stabilizing the intermediates of O_2 activation and substrate oxidation. Our current results suggest that the rate of HAT is far faster than subsequent reactions, due to the strong H-bonds to the resultant -OH ligand. We anticipate that a study focused on comparing rates of HAT to high-valent Fe^{IV}-oxo complexes with varied H-bond strength and to known values for the parent TPA ligand with no H-bonds will help us to understand the effects of H-bonding in this system.

While our work has shown the Fe^{IV}-oxo is able to facilitate oxidation reactions without additional oxidant besides O_2, there is a dearth of literature that used H_2O_2 as the oxidant in related iron systems. Current work, which we hope to investigate further, is examining the FeL^H system for oxidation of organic substrates, including cyclohexene, using a mixed O_2/H_2O_2/H_2O system. Work by other groups has suggested that this combination of oxidants can change the mechanism of the oxidation, enabling access to an iron(V) species, which is attributed to additional binding of the H_2O_2 or H_2O to the Fe center.[55, 269] A comparison of the product distribution of these oxidation reactions under various oxidizing conditions (Fig. 5.5), especially in parallel with the related non-H-bonding TPA complexes, should give us valuable insight into the role H-bonds play in the mechanism of cyclohexene oxidation.

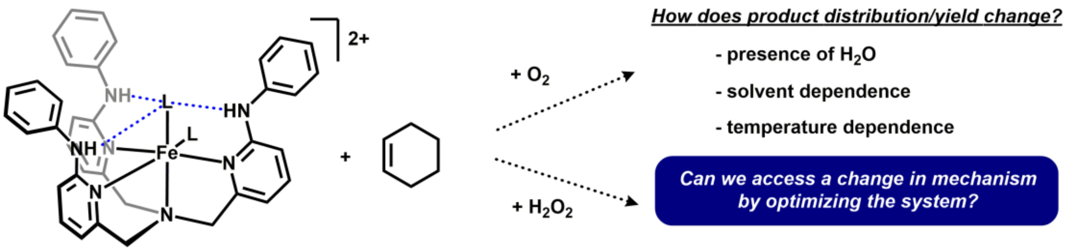

Figure 5.5 Optimization for cyclohexene oxidation with high valent iron species

In looking to future studies with the FeL^H system, we are interested in probing reactivity with oxyanions such as nitrate, nitrite, and perchlorate. Preliminary reactions of complex **3.4** with [NBu_4][ClO_4] resulted in formation of a green paramagnetic species, rather than a simple anion exchange. This suggests a reaction with the perchlorate anion, which could be forming the high-valent Fe^{IV}-oxo and an Fe^{II}-Cl species as the end products, although the messy ^{1}H NMR spectrum will require further investigation. This reaction mirrors the perchlorate reduction by Fe^{II} reported by the Fout group and suggests our complex may be capable of other oxyanion reductions.[38] Probing the effect of the H-bond strength using our tunable L^R ligands on the stability and reactivity of the high-valent oxo intermediates and on oxyanion reduction will be relevant in future studies for the stabilization and isolation of high-valent oxo intermediates.

While H-bond strength can be easily modified by tuning the electronics of the appended aniline group, we must consider the effect that this has on the complex as well. The small electronic change in the aniline may not have a significant effect on the reactivity of the complex, but it is impossible to decouple the change in H-bond strength and complex electronics when we tune electronics of L^R. To circumvent this, and probe only the electronics of the metal complexes, it may be time to return to making modifications in the primary sphere: in theory, a tunable 4th arm could be incorporated into the L^H ligand, one that does not influence the H-bond strength. Alternatively, we could simply synthesize complexes which have a tunable ligand separate from L^R in the 6th coordination site. Studies with both the nickel and iron L^H complexes showed they can adopt an octahedral geometry. Using an anionic ligand, such as a phenoxide, which could be electronically tuned by varying its substituents (Fig. 5.6), to occupy the sixth site, could allow us to interrogate the effect of the changes in the electronics of these complexes for small molecule activation, without inherently effecting the strength of the H-bonds (or perhaps moving into a regime where PCET is accessible). This, in turn, could help inform us of the effect primary sphere ligand have on the O_2 reduction reaction, and help us better understand the specific role H-bonding plays in enabling substrate activation.

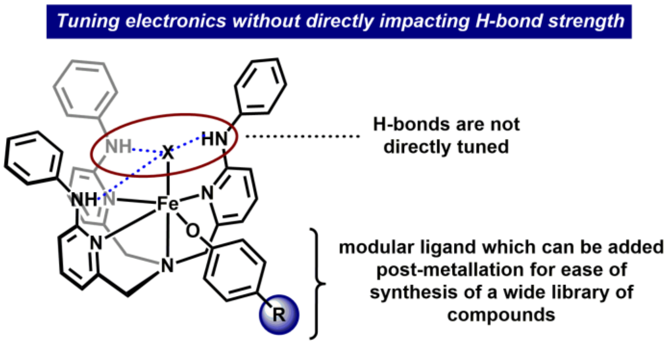

Figure 5.6 Modifying the primary sphere in the presence of reductively stable H-bonds may enable new routes of complex reactivit

Appendix A Initial Studies of a Tripodal Ligand for Bifurcated Hydrogen Bonding

A.1 Introduction

In much of our group's previous work, we have used H-bond donors that are co-planar with the open coordination site for binding small molecules of interest. We have also incorporated tetradentate amine-based ligand frameworks, specifically modified TPA derivatives, in part because of the ease for modifying the secondary sphere but also because of the well-developed systems without H-bonds. Many biological systems have tetrahedral active sites, not octahedral or trigonal pyramidal, and H-bonds are not typically coplanar with the substrate.[53, 270-271] Often, H-bond residues are further from the binding site and may only interact one or two at a time. This led us to consider the construction of our model complexes and reexamine our efforts to model biologically relevant small molecule binding and activation.

Tripodal ligands are well documented, particularly the anionic tripyrazolylborate (Tp) variants, which have served to coordinate just about every first row and many second and third row transition metals for a multitude of reactions. These "scorpionate" ligands are considered tetrahedral enforcers, although distorted octahedral bis-ligand complexes have been reported.[272-273] The neutral variants (Tpm) have also been reported for a variety of reactions, however, because they are neutral, they tend to bind less tightly to metal complexes and/or change the reactivity.[274] These complexes are active for small molecule activation (N_2,[275] O_2,[276] NO_2[277]), catalysis (silylation,[278] C-H activation[279]), and organometallic reactions.[280-281] The modification of the Tp ligands is rather limited by the pyrazolate groups. Steric incorporation has been shown to prevent bis-ligand complex formation or to bias reactions, but asymmetric substitutions can be difficult, and the anionic ligands have not been substituted with H-bond groups, to the best of our knowledge.

In order for us to better model biological active sites, we turned to the investigation of a neutral tripodal ligand framework, tris(2-pyridyl)ethane (TPE), which we proposed we could modify to form an asymmetric ligand with H-bond donor groups. The asymmetric precursor TPE^{Br} could be formed by modifying the final step of the ligand synthesis to incorporate a brominated pyridine.[282] We hypothesized that using this ligand would enable us to vary the H-bond donors in the secondary coordination field, much like we have with the TPA[18, 22, 45, 173] and tpy[44, 283] variants we've already reported.

We are interested in incorporating a bifurcated H-bonding moiety in the secondary sphere of this ligand. Urea groups are prevalent in protein structures as they form the core of many peptide sequences and can act as dual H-bond donors. The insolubility of urea itself makes it a difficult synthetic reagent to work with, however slightly more soluble squaramide compounds have been shown to perform similarly to or better than urea for H-bond catalysis and anion binding.[284-287] We thus sought to incorporate a squaramide bifurcated H-bond donor in the secondary coordination sphere of our tripodal ligand, hypothesizing that the bifurcating nature would allow us to trap intermediates and stabilize products of small molecule activation with the correspond metal complexes. Work in this Appendix describes our early work towards the synthesis of the bifurcated H-bonding ligand TPE^{NHsqam}, synthesis of a control ligand, TPE^{pip}, and the synthesis and reactivity of first row transition metal complexes with the control ligand, with an eye toward evaluating what reactivity may be of interest to further investigate using TPE^{NHsqam} (Fig. A.1).

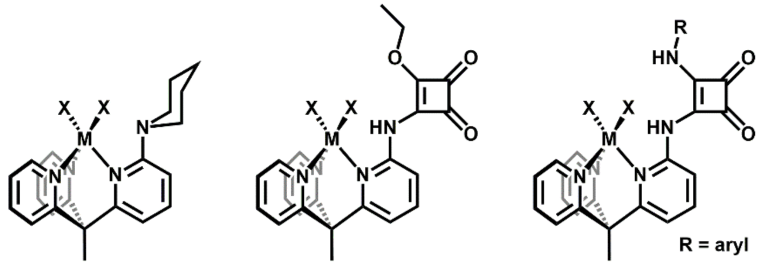

Figure A.1 Tripodal complexes proposed for the activation of small molecules; TPE^{pip} (left), TPE^{NHsq} (center), TPE^{NHsqam} (right) on a M^{+2} core.

A.2 Progress on the synthesis of a bifurcated H-bonding ligand

We began our efforts to synthesize a new neutral tripodal ligand by modifying an existing route for the synthesis of tris(2-pyridyl)ethane. In a step-wise synthesis, we introduced 2, 6-dibromopyrdine in the final step to yield a monobrominated ligand, TPE^{Br}. We set out to use this ligand as a platform to incorporate a substituted squaramide as a bifurcated H-bond donor (Fig. A.1). A trityl-amine protected TPE variant, TPE^{NTr}, was deprotected to give TPE^{NH2} in 70% yield. Two routes were explored for the formation of the bifurcated H-bond ligand TPE^{NHsqam}. A converging synthesis was explored (Fig. A.2), where in the first step, diethyl squarate was reacted with one equivalent of 3,5-bis(trifluoromethyl)aniline to form the 3,5-bis(trifluoromethyl) squaramide (sqam). This was combined with TPE^{NH2} in the second step to form the squaramide TPE ligand (TPE^{sqam}). However, this step has proven difficult, as several different sets of conditions provided either no reaction or a mixture of species. In a linear synthesis (Fig. A.3), we first substituted TPE^{NH2} with diethyl squarate to form TPE^{NHsq}. The crude product of this reaction was combined with 3,5-bis(trifluoromethyl)aniline in ethanol for 2 days at 80 °C. This yielded a new compound, which we tentatively propose is the desired product (TPE^{NHsqam}), although the product has not been purified or fully characterized. We can track the formation of these complexes by the aryl C-H groups of the aniline moiety, as well as the TPE-NH group. We did note the appearance of additional alkyl multiplets in the aliphatic region, different than those from the crude material we started with, which we were not expecting; these results are as yet unconfirmed, and we anticipate the potential need for optimization for the synthesis of TPE^{NHsqam}.

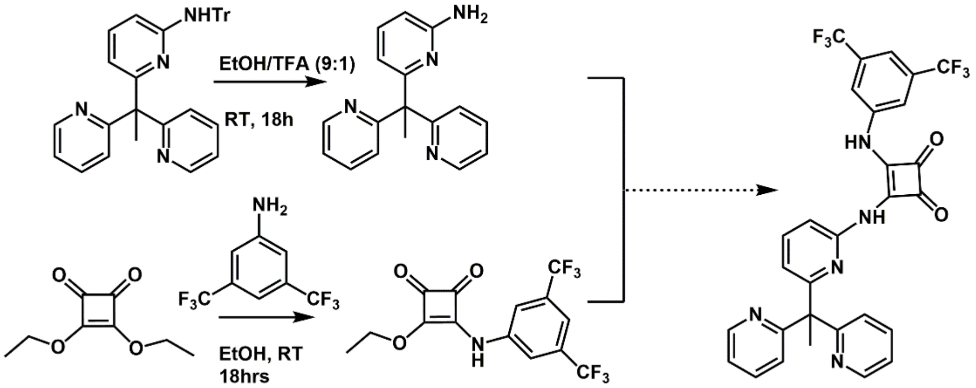

Figure A.2 Scheme for the converging synthetic route to TPE^{NHsqam}.

One reason we may be having difficulties installing the second aryl/heterocyclic group on the squaramide may be due to electronics. Reports of squaramide molecules substituted with asymmetric aryl and heterocycle groups are rare, with only five patents published to date. These compounds require both long reaction times and high temperature to obtain the desired product, and in the case of a 2-amino pyridine variant, require oxidation of the pyridine for the successful synthesis of the desired squaramide.[288] A wider literature search for asymmetric squaramides reveals they typically incorporate one aryl group and one benzylic or alkyl group. Symmetric aryl substitution of squaramides is reported more frequently, likely due to the ease of their synthesis. [284-287, 289-292] This leads us to consider that we simply need to better optimize the coupling for the asymmetric TPE squaramide ligand, utilizing additives like $Zn(OTf)_2$, higher temperatures, and longer reaction times (see supporting information for details).

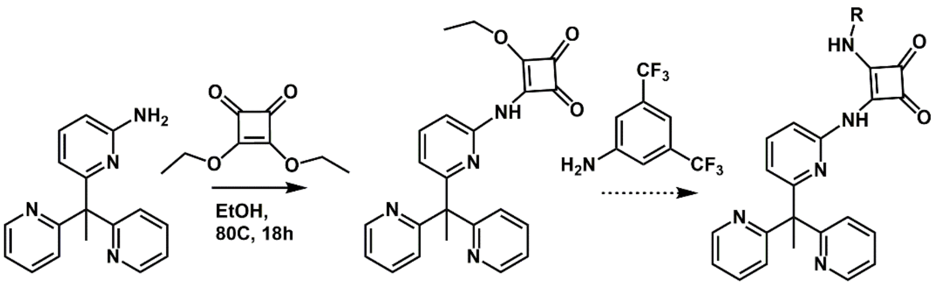

Figure A.3 Scheme for the linear synthesis of TPE^{NHsqam}

In parallel to the work on the synthesis of the bifurcated H-bond ligand, we anticipated the need for a ligand that could act as a H-bond acceptor on the same TPE framework. Starting from TPE^{Br}, we initially used a method previously described by our group to install a morpholine group in place of the bromine (Fig. A.4). Switching to piperidine instead of morpholine, and running it neat conditions improved this synthesis, with an easier purification and decent yield of the ligand TPE^{pip} (55%). We characterized this complex by ^{1}H NMR and mass spectrometry. This ligand was used for the synthesis of a series of transition metal complexes, described below.

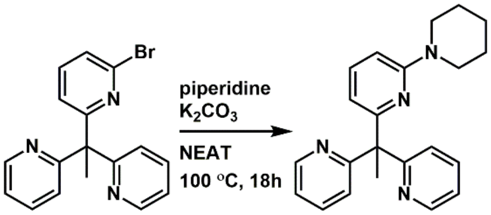

Figure A.4 Scheme for the synthesis of TPE^{pip}

A.3 Synthesis of tripodal transition metal complexes

We explored the synthesis of a series of first row transition metal complexes with TPE^{pip}. Iron, cobalt, and zinc were used, and clean reproducible syntheses using FeX$_2$, CoX$_2$, and ZnX$_2$ (X = Cl, Br, OTf) formed the MX$_2$TPE^{pip} complexes. Generally, these complexes were synthesized by stirring 1 eq. of TPE^{pip} with 1 eq. MX$_2$ in solvent for 5-18 h, yielding monomeric complexes obtained in good yield. The ^{1}H NMR spectra indicate that both the Fe and Co complexes are paramagnetic, high spin species; in CH$_2$Cl$_2$; the Co complex exhibits 11 resonances, corresponding to the asymmetric arms of the ligand. Using the $ZnBr_2$ analogue, we can assign the resonances of the ligand and confirm it has a monomeric structure. Interestingly, one arm of the complex is significantly broadened, which we attribute to its fluxional binding to or even dissociation from zinc.

We were able to grow single crystals of the Co and Zn bromide derivatives and obtained solid state structures (Fig. A.5). The Co complex is best described as a distorted trigonal bipyramidal geometry ($\tau_5 = 0.29$),[191] with the three pyridine nitrogen atoms coordinated, and no interaction between the cobalt and piperidine nitrogen. The Zn complex is a slightly distorted tetrahedral ($\tau_4 = 0.80$),[293] with the substituted pyridine arm dissociated in solution, with the pyridine twisted away from the zinc center, preventing any interaction. Our hypothesis of the fluxional arm is supported by this structure. The M-N and M-Br bonds are tabulated in Table A.1 for both complexes and are within the expected range of Co-N and Zn-N bonds for similar structures. Neither structure exhibits short contacts between the piperidine nitrogen and another molecule, only weak CH…Br interactions.

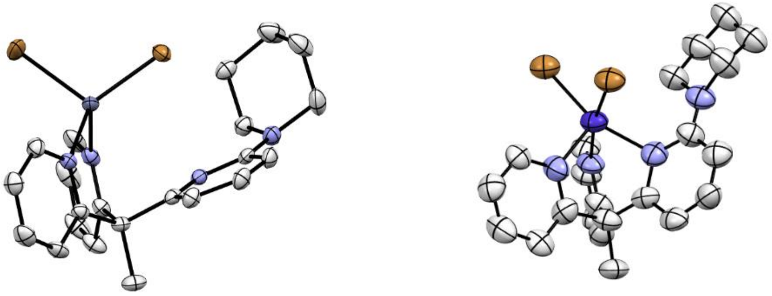

Figure A.5 Crystal structures of $ZnBr_2TPE^{pip}$ and $CoBr_2TPE^{pip}$.

Table A.1 Selected bond lengths and distances in Co and Zn TPE^{pip} crystal structures

Bond/Contact	$CoBr_2TPE^{pip}$ Distance (Å)	$ZnBr_2TPE^{pip}$ Distance (Å)
M-N_1 (pyr)	2.06(2)	3.425(2)*
M-N_3 (pyr)	2.19(2)	2.049(2)
M-N_4 (pyr)	2.12(2)	2.057(2)
M-N_2 (pip)	3.37(2)	4.961(2)
M-Br_1, M-Br_2	2.492(3), 2.472(4)	2.3293(4), 2.3848(4)

* Denotes non-coordinated pyridine.

A.4 Reactivity of Co and Fe complexes

With these new complexes in hand, we began to investigate their redox capabilities and reactivity toward small molecules. Cyclic voltammetry experiments (Fig. A.6) of $CoBr_2TPE^{pip}$ and $FeBr_2TPE^{pip}$ in 0.1 M $[Bu_4N][PF_6]$ in CH_3CN showed irreversible reduction events. When excess $[Bu_4N][Br]$ was added to $FeBr_2TPE^{pip}$, an irreversible and reversible reduction were observed at -1.69 V (irreversible, onset potential) and -2.43 V (reversible, $E_{1/2}$) vs Fc. Oxidative events for both complexes were observed at -0.19 V (Fe) and +0.464 V and +0.977 V (overlapping events, Co). This data suggests we should be able to access reactivity in lower and higher oxidation states of these complexes.

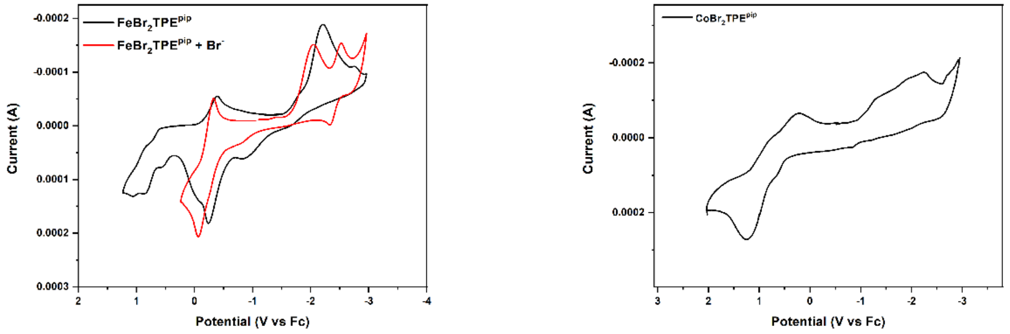

Figure A.6 Cyclic voltammetry of $FeBr_2TPE^{pip}$, with additional $[Bu_4N][Br]$ (left) and $CoBr_2TPE^{pip}$ (right) in 0.1 M $[Bu_4N][PF_6]$ in CH_3CN.

We initially examined the reduction reactions of both $CoBr_2$- and $FeBr_2TPE^{pip}$ complexes. When the teal-colored Co complex was reduced in THF with KC_8, $LiEt_3BH$, or Mg^0 turnings, the solution turned deep blue, and a paramagnetic complex with slightly shifted peaks and one new resonance compared to the starting complex was observed by ^{1}H NMR spectroscopy in all three cases, with occasional small amounts of free ligand also observed. If we added reagents that we predict would react with a low valent cobalt(I) complex, such as iodobenzene or 2,6-dichloropyridine N-oxide (^{Cl}PyO) following reduction with KC_8, no reaction is observed. This same species is also observed in small amounts with the addition of dichloro-dicyanoquinone (DDQ), an oxidant. These results suggests that the new species formed is likely a dimeric species, possibly with bridging bromide ligands. The lack of secondary sphere bulk would make this feasible and explains the lack of reactivity towards the aryl iodide and OAT reagent.

Similarly, when $FeBr_2$TPEpip was reduced with KC_8 or $LiEt_3BH$, the solution became nearly black, and attempts to obtain ^{1}H NMR spectra were futile, as the sample could never shim correctly, and even the solvent peak was drastically broadened. We proposed that the reduction conditions led to formation of Fe clusters or nanoparticles, which we could not easily characterize.

We next examined the reactivity of the two complexes with small molecules form the +2 oxidation state. The reaction of $CoBr_2TPE^{pip}$ with ^{Cl}PyO was gave no reaction, while the reaction of N-methylmorpholine N-oxide (NMO) resulted in a new paramagnetic species we attribute to the coordination of the morpholine moiety; oxidation of the complex resulted in decomposition of the complex overnight. Reactions with K^tBuO and $HBAr'_4$ resulted in demetallation of the ligand, which we also observe with the iron analogue. Interestingly, the addition of 1 eq. of KOH to $CoBr_2TPE^{pip}$ resulted in the shift of several peaks and loss of one in the ^{1}H NMR spectrum. This suggests a ligand exchange of -OH for -Br may have taken place. We then subjected this species to 1 eq. of KHMDS in an attempt to form a cobalt-oxo and observed full consumption of the proposed hydroxide complex, alongside formation of a new paramagnetic species. We also observed some demetallation within about 1 hour, and full decomposition of the new species overnight. While we have yet to fully characterize these two new species, they are indicative of the reactivity of the Co complex for reactivity with oxygen containing substrates.

Finally, we attempted to demonstrate these complexes were suitable for hydroboration catalysis. In THF, $FeBr_2TPE^{pip}$, HBpin, and Na^{t}BuO were combined with dodecane and stirred for 22 h at room temperature (Fig. A.7). The reactions were analyzed by ^{1}H NMR spectroscopy against an internal standard, although the yield data is inconsistent and need replication before yield data can be reliably reported. The cobalt derivative was also tested, and control reactions were run side by side with these reactions, the qualitative results of which are outline in Table A.2.

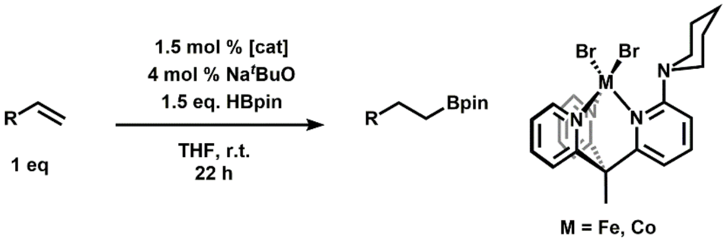

Figure A.7 Scheme for catalytic hydroboration reactions with MBr_2TPE^{pip}

The formation of new alkene peaks in the ^{1}H NMR spectra of these reaction led us to the conclusion that rather performing hydroboration reactions, we were instead performing some kind of isomerization or cyclization reaction. ^{11}B NMR data of the reactions with $FeBr_2TPE^{pip}$ and $CoBr_2TPE^{pip}$ indicate hydroboration occurs, although the spectra for these reactions indicate the hydroborated product is only a minor pathway with the iron complex but makes up significant portion of the products when $CoBr_2TPE^{pip}$ is used. Oxidative workup of the products from the reaction yielded the carboxylic acid products, rather than any ketones, indicating these reactions undergo isomerization, rather than cyclization reactions.

Table A.2 Analysis of hydroboration reactions under different conditions

Entry	[cat]	Borane	Unreacted Dodecene	Hydroboration	Isomerization
1	[Fe]		yes	trace (^{11}B)	yes
2	[Fe]	no HBpin	yes	--	trace
3	[Co]		no	yes (^{11}B)*	yes
4	[Co]	no HBpin	yes	--	no
5	$FeBr_2$		trace	no	yes*
6	$FeBr_2$	no HBpin†	trace	no	yes*

* Denotes a major species. † Added $LiEt_3BH$.

We note the total conversion of dodecane is inconsistent with the yield of the isomerization and/or hydroboration products, particularly with $FeBr_2TPE^{pip}$. Analysis of the NMR and GC-MS data only allow us to observe the isomerization product, suggesting that other pathways are not likely unless they are removed during workup. Control reactions without HBpin and without the TPE^{pip} complex (Table A.2, entries 5 and 6) still result in the same isomerized species. The evidence from the control reactions is clear: the hydroboration is not achieved with $FeBr_2TPE^{pip}$ in high yields because the isomerization reaction of the alkene by $FeBr_2$ outcompetes the reaction. Indeed, the isomerization conversion is comparable between the $FeBr_2$ salt and the TPE^{pip} complex, suggesting that the reaction is not directly impacted by the ligand. Follow up studies for the hydroboration reaction using $CoBr_2TPE^{pip}$ are warranted based on these results, and control reactions against other cobalt complexes should be run. Ideally, we could examine the effect of secondary sphere H-bonds on the rate and product distribution of this reaction in comparisons to the TPE^{pip} H-bond acceptor ligand described here.

A.5 Conclusions and Future Directions

In conclusion, we report the synthesis of a tripodal pyridine ligand, TPE^{pip}, featuring a H-bond acceptor in the secondary sphere, and the subsequent synthesis and reactivity of Fe, Co, and Zn complexes of the ligand. We have established that TPE^{pip} is not a suitable ligand for reductive chemistry, resulting in formation of unreactive dimeric species or clusters. Investigation of small molecule reactions showed addition of substrates often resulted in demetallation rather than productive reality, although there may be some promising chemistry between $CoBr_2TPE^{pip}$ and hydroxide. Finally, hydroboration reactions were studied, and divergent reactivity was observed between the cobalt and iron analogues, with isomerization of the starting alkene highly favored by the iron complex, and competitive hydroboration and isomerization in the reaction with the cobalt variant.

There are several clear routes for the continuation of this project. First is to finalize a route to the H-bonding ligands. Our initial pass at the synthesis of the ligand seems to form a new ligand that would suggest we've made the desired compound, but more detailed NMR and mass spec analysis will be required to help confirm the desired squaramide ligand has been synthesized. Additionally, while this synthesis is being optimized, it would be useful to incorporate the singly-substituted squaramide ligand (TPE^{NHsq}) into our library of ligands. Synthesis of Fe and Co complexes with this ligand would allow us to directly compare to the TPE^{pip} ligand and eventually the TPE^{NHsqam}, as it serves as the intermediate between the two, with only one H-bond donor. We anticipate that the complexes with one or two H-bonding interactions should have more attractive interactions with ligands bound to the metal center, which should provide stabilization of the products of their reaction, rather than demetallation or decomposition as observed with the TPEpip complexes.

Second, we anticipate that reactions with the bis-triflate complexes for small molecule activation may be easier to access than with the dihalide species described above. For example, the activation of O_2 by $Fe(OTf)_2TPE^R$ may be accessible. Alternatively, we may be able to induce reactions by adding a halide abstracting reagent to open a coordination site once the complex and substrate are in solution together. This may circumvent some of the decomposition pathways we observed.

Additionally, the divergent reactivity of $CoBr_2TPE^{pip}$ and $FeBr_2TPE^{pip}$ for alkene hydroboration warrants follow-up studies. The control reactions with $FeBr_2$ salt indicate the necessity for control reactions to compare the activity towards hydroboration. More importantly, the incorporation of one or two H-bond donors (TPE^{NHsq} and TPE^{NHsqam}) rather than using a H-bond acceptor (TPE^{pip}) could have a drastic effect on the outcome and distribution of this reaction. Hydrogen bonding interactions in hydroboration reactions could be competitive with the substrate for borylation, so optimization or selection of different, more activated substrates may be necessary to be able to study the effects of H-bonding on the rate and/or product distribution of hydroboration.

Finally, we anticipate a nickel analogue of these complexes would be interesting for analogous comparisons to the neutral TPM nickel complexes recently reported by the Sanford group. Their studies indicated that the nickel(III) complexes formed using the TPM ligand underwent rapid C-C bond formation from a reductive elimination reaction that was significantly slower with the related nickel(IV) complex. The similarities of our TPE ligand framework compared the neutral TPM make this an interesting organometallic platform to compare against. The heteroatom-carbon coupling reaction works well for nickel(IV) but not for nickel(III) – if H-bonds capable of interacting with the heteroatom could position the nucleophile close to the metal center, heteroatom-carbon coupling could be favored.

In summary, we have only begun to scratch the surface of the chemistry that may be accessible using a tripodal ligand with bifurcated H-bonds. We've demonstrated that an analogous H-bond accepting ligand can participated in some small molecule activations or catalysis, but the full breadth of this chemistry has not really been explored. We envision the incorporation of H-bonds will enable capture of small molecules, prevent unproductive dimerization pathways, and provide necessary stabilization of reactive intermediates/products.

A.6 Acknowledgments

We gratefully acknowledge Dr. Jacob B. Geri for synthesis of the TPE^{Br} ligand and Jared Gonder for work towards the synthesis of TPE^{NHsqam} and for the synthesis and crystallization of $ZnBr_2TPE^{pip}$. We acknowledge Dr. Matthias Zeller for crystal data collection and the structure solution for $ZnBr_2TPE^{pip}$, and Dr. Jeff Kampf for crystal data collection for $CoBr_2TPE^{pip}$.

A.7 Supporting Information

A.7.1 General Considerations

All air- and moisture-sensitive manipulations were performed using standard Schlenk techniques or in an inert atmosphere glovebox with an atmosphere of purified nitrogen. The glovebox was equipped with a cold well designed for low temperature experiments as well as a −35 °C freezer for cooling samples and crystallizations. Solvents were purified using a Glass Contour solvent purification system through percolation through a Cu catalyst, molecular sieves, and alumina. Solvents were then stored over sodium and/or molecular sieves. Deuterated solvents were purchased from Cambridge Isotope Laboratories and used as received.

Iron dibromide, iron dichloride, iron bis-triflate, cobalt bromide, cobalt dichloride, zinc bis-triflate, $LiEt_3BH$ (0.1 M, THF), and KHMDS were purchased from commercial vendors and used as received. Dichloro-dicyanoqunioline (DDQ), N-methlyl morpholine N-oxide (NMO), 2,6-dichlorpyridine N-oxide (^{Cl}PyO), magnesium turnings, potassium hydroxide, and potassium tert-butoxide were purchased from commercial vendors and dried under vacuum before transferring to a nitrogen glovebox. Ferrocene was purchased from a commercial vendor and sublimed prior to use. Diethyl squarate, iodobenzene, cyclohexene, dodecane, and styrene were dried over calcium hydride, distilled under vacuum, brought into the glovebox and stored over sieves. Potassium graphite,[204] Brookhart's acid ($HBAr'_4$),[294] were synthesized according to literature procedures. TPE^{NTr} were synthesized by Jacob B. Geri by stirring TPE^{Br} with LiNHTr in THF at 70 °C for 24 h. TPE^{Br}[282] and 3,5-bis(trifluoromethyl) phenyl squaramide (sqam) were synthesized as previously reported.

Caution! Potassium graphite is a potentially pyrophoric and/or explosive material that should be handled with caution under an inert atmosphere where possible.

NMR spectra were acquired on Varian 400 MHz, 500 MHz, or 700 MHz spectrometers as indicated below. ^1H NMR spectra are referenced to non-deuterated internal solvent residuals and are reported in parts per million (ppm) relative to tetramethylsilane. ^{19}F and ^2H NMR spectra are referenced to their respective ^1H spectra. Multiplicities are reported as follows: singlet (s), doublet (d), triplet (t), quartet (q). The spectra for paramagnetic molecules were obtained by using an acquisition time of 0.5 s, thus the peak widths reported have an error of ±2 Hz.

Mass spectra were recorded on an Agilent 6230 TOF HPLC-MS with a liquid phase of 95% acetonitrile, 5% water, 0.1% formic acid. Electrochemistry was performed with a Pinewave Wavenow potentiostat under a dinitrogen atmosphere with a glassy carbon working electrode, a platinum counter electrode, and a silver wire pseudo-reference electrode. Measurements were taken at a scan rate of 100 mV/s, scanning reductively from the open circuit potential. Samplex were referenced against an internal ferrocene standard. Electrolyte, $[NBu_4][PF_6]$, was used in 0.1 M in CH_3CN.

A.7.2 Synthesis of ligands

TPE^{NH2}: Tritylamine TPE (TPE^{NTr}, 100 mg, 0.192 mmol) was dissolved in EtOH/trifluoroacetic acid (9:1) and stirred at room temperature for 5 h. The solvent was removed by rotary evaporation and redissolved in Et_2O, then extracted with H_2O (3 x 20 mL). The solution was neutralized with saturated NaHcO3 (40 mL), and washed with DCM (3 x 15 mL). Organic fractions were combined and dried. A pale brown solid was recovered (37 mg, 69 %). ^{1}H NMR (400 MHz, CH_2Cl_2) δ 8.5162 (dd, *J* = 4.6, 1.5 Hz, 2H), 7.5637 (td, *J* = 8.0, 1.9 Hz, 2H), 7.3108 (q, *J* = 8.7, 8.3 Hz, 1H), 7.1598 – 7.0346 (m, 4H), 6.3253 (dd, *J* = 23.6, 7.9 Hz, 2H), 4.3757 (s, 2H), 2.1900 (s, 3H).

TPE^{NHsq}: Modified from previous reported procedure.[295] TPE^{NH2} (5.8 mg, 0.021 mmol) was combined with diethyl squarate (93.3 μL, 0.0223 mmol) in ethanol (20 mL) and stirred a 80 °C for 20 h. The solvent was removed under vacuum to leave a sticky yellow oil (8.5 mg) which was used without further purification before carrying on to the next step for the synthesis of TPE^{NHsqam}. ^{1}H NMR (400 MHz, *d*-DMSO) δ 10.6529 (s, 1H), 8.5286 (d, *J* = 5.1 Hz, 2H), 8.0319 (t, *J* = 8.0 Hz, 2H), 7.7972 (t, *J* = 8.0 Hz, 1H), 7.5369 – 7.4212 (m, 4H), 7.1332 (d, *J* = 8.4 Hz, 1H), 7.0489 (d, *J* = 7.6 Hz, 1H), 4.6512 (q, *J* = 7.5, 7.1 Hz, 1H), 4.5319 (q, *J* = 7.1 Hz, 4H), 2.1928 (s, 3H), 2.0728 (s, 4H), 1.9079 (s, 0H), 1.7523 (s, 0H), 1.3426 (dt, *J* = 22.7, 7.0 Hz, 8H), 1.2349 (s, 0H).

Attempted synthesis of TPE^{NHsqam}:

Linear route from TPE^{NHsq}: Crude material from the synthesis of TPE^{NHsq} (8.5 mg) was dissolved in EtOH (2 mL) and stirred. 3,5-bis(trifluoromethyl) aniline was added and the reaction mixture heated to 80 °C for 20 h. The solution as removed from heat, the solvent evaporated, and crude NMR spectrum obtained. ^{1}H NMR (400 MHz, *d*-DMSO) δ 11.2032 (s, 1H), 10.6842 (s, 1H), 10.3671 (s, 3H), 8.5694 – 8.5011 (m, 2H), 8.2565 (s, 6H), 8.0447 (td, *J* = 7.7, 7.2, 1.9 Hz, 4H), 7.8473 – 7.7576 (m, 2H), 7.5501 – 7.4320 (m, 7H), 7.1393 (d, *J* = 8.3 Hz, 1H), 7.0481 (d, *J* = 7.7

Hz, 1H), 4.8009 (q, *J* = 7.0 Hz, 2H), 4.7024 – 4.5556 (m, 6H), 4.5629 (s, 3H), 4.5453 (s, 1H), 2.1987 (s, 3H), 1.4590 – 1.3632 (m, 4H), 1.3446 (q, *J* = 7.0 Hz, 14H), 1.2886 – 1.1358 (m, 3H), 1.0536 (t, *J* = 7.0 Hz, 2H).

Convergent route: TPE^{NH2} (5 mg, 0.018 mmol) was combined with 3,5-bis(trifluoromethyl)phenyl squareamide (sqam, 7.7 mg, 0.022 mmol) and stirred overnight at the given temperature (Table A.3).

Table A.3 Conditions for attempted synthesis of TPE^{NHsqam}

Solvent	Temperature (°C)	Time (h)	Product
EtOH	50	18	no reaction
CH_3CN	r.t.	18	no reaction
CH_3CN/DMSO	60	18	no reaction
CH_3CN/DMSO	80	18	no reaction
EtOH + Et_3N	80	18	trace new species
CH_3CN	r.t.	18	no reaction
CH_3CN + $Zn(OTf)_2$	r.t	18	Zn complex
THF + KTol	-80 to r.t.	18	deprotonated

TPE^{pip}: In a 20 mL scintillation vial open to air, TPE^{Br} (1.50 mL, 0.488 M in THF, 0.73 mmol) was combined with K_2CO_3 (210 mg, 1.52 mmol) and piperidine (3.0 mL, 30 mmol) and stirred at 100 °C for 18 h. The solution was cooled, 50 mL H_2O added and extracted with Et_2O (3x 70 mL). The combined organics were washed with 100 mL saturated NaCl solution, and the organic solution was dried over $NaSO_4$. The solvent was removed and directly loaded onto a Biotage column (25 g, 25 % EtOAc/hexanes 18 CV, 25-100% EtOAc over 6 CV). Fractions 6-10 were combined and dried (138, 55%). ^1H NMR (400 MHz, CH_2Cl_2) δ 8.5040 (dd, *J* = 4.9, 1.7 Hz, 2H), 7.5405 (td, *J* = 7.8, 1.9 Hz, 2H), 7.3645 (t, *J* = 8.0 Hz, 1H), 7.1403 – 7.0213 (m, 4H), 6.4857 (d, *J* = 8.4 Hz, 1H), 6.3490 (d, *J* = 7.5 Hz, 1H), 3.4203 – 3.3432 (m, 5H), 2.2019 (s, 3H), 1.5419 (dq, *J* = 28.1, 5.5 Hz, 8H).

A.7.3 Synthesis of complexes

$CoBr_2TPE^{pip}$: In a 20 mL vial, TPE^{pip} (66 mg, 0.192 mmol) was combined with $CoBr_2$ (46 mg, 0.211 mmol) in 20 mL CH_2Cl_2 and stirred at room temperature overnight. The resulting teal solution was filtered and dried to yield a teal solid (110 mg, quantitative). ^{1}H NMR (400 MHz, CH_2Cl_2) δ -38.65, -14.91, -8.05, -2.08, 11.65, 30.96, 27.43, 38.61, 47.12, 72.87, 72.87, 79.27.

$FeBr_2TPE^{pip}$: In a 20 mL vial, TPE^{pip} (20 mg, 0.058 mmol) was combined with $FeBr_2$ (14 mg, 0.065 mmol) in 10 mL CH_2Cl_2 and stirred at room temperature for 2 h after which the yellow solution was filtered and dried, washed with pentane, and dried to yield a yellow solid (34 mg, quantitative). ^{1}H NMR (400 MHz, CH_2Cl_2) δ -10.71, 2.29, 7.40, 18.51, 26.51, 41.17, 74.42.

$ZnBr_2TPE^{pip}$: In a 20 mL vial, TPE^{pip} (81 mg, 0.235 mmol) was combined with $ZnBr_2$ (57 mg, 0.253 mmol) in 10 mL CH_2Cl_2 and stirred overnight. The resulting colorless solution was filtered and pumped down, redissolved in CH_2Cl_2, triturated with pentane, and dried to yield an off-white solid (133 mg, quantitative). ^{1}H NMR (400 MHz, CH_2Cl_2) δ 8.9404 (dd, *J* = 5.3, 1.8 Hz, 2H), 8.0391 (td, *J* = 8.0, 1.9 Hz, 2H), 7.8305 (d, *J* = 8.2 Hz, 2H), 7.5881 – 7.5059 (m, 2H), 7.3324 (s, 1H), 6.5641 (s, 1H), 5.8669 (s, 1H), 3.1766 (t, *J* = 5.2 Hz, 5H), 2.2632 (s, 4H), 1.5412 (q, *J* = 6.1, 5.6 Hz, 3H), 1.4621 – 1.3833 (m, 5H).

$CoCl_2TPE^{pip}$ and **$FeCl_2TPE^{pip}$**: Same as above in CH_3CN.

$Fe(OTf)_2TPE^{pip}$ and **$Zn(OTf)_2TPE^{pip}$**: Same as above in CH_3CN. **$Fe(OTf)_2TPE^{pip}$** (83%).

A.7.4 Reactivity of $FeBr_2TPE^{pip}$ and $CoBr_2TPE^{pip}$

Reduction reactions

General procedure: $CoBr_2TPE^{pip}$ (10 mg, 0.018 mmol) or $FeBr_2TPE^{pip}$ (10 mg, 0.018 mmol) was dissolved in THF (2-4 mL) and combined with the reductant in THF (see below) at room temperature. Reactions were typically allowed to stir for 30 min – 2 hours, then overnight and were monitored by ^{1}H NMR spectroscopy.

KC_8: 3.0 mg, 0.022 mmol, 1.2 eq.; in 1-2 mL THF (run at room temperature and frozen THF)

$LiEt_3BH$: 0.18 mL (0.1 M in THF); 1 eq.

Mg^0: 1.0 mg, 0.0411 mmol, 2.3 eq.; in 4 mL THF

*$FeBr_2TPE^{pip}$ reductions were frozen in THF and KC_8 or $LiEt_3BH$ added after just thaw, then allowed to warm to room temperature.

Reactions with "reduced" $CoBr_2TPE^{pip}$: Follow general procedure for reduction from frozen THF, then add substrate and bring to room temperature to stir for 3 hr, then overnight.

Oxidation reactions

Follow the same general procedure as for reductions.

DDQ: 4.0 mg, 0.0232 mmol, 1.3 eq; in 2 mL THF

NMO: 2.2 mg, 0.0189 mmol, 1.1 eq; in 2 mL THF

^{Cl}PyO: 3.0 mg, 0.0182 mmol, 1.04 eq; in 2 mL THF

Small molecule reactions.

Follow general procedure as the reduction reactions: stirred at room temperature for 2 h.

KO^tBu: 2.2 mg, 0.0196 mmol, 1.1 eq; 4 mL THF

KOH: 1.0 mg, 0.0188 mmol, 1.1 eq; 3 mL THF

Followed by KHMDS: 4 mg, 0.0201 mmol, 1.13 eq.

$HBAr'_4 \bullet 2\ Et_2O$: 10 mg, 0.0099 mmol, 1.1 eq; 4 mL THF

Catalytic reactions.

General procedure. Dodecene (0.66 mmol, 1 eq.), catalyst (0.01 mmol, 1.5 mol %), and HBpin (1.00 mmol, 1.5 eq) were combined in THF (2 mL) and then Na^tBuO (0.023 mmol, 4 mol %)

added. The reaction was stirred at room temperature for 22 hours, and the solvent removed under vacuum. The organics were extracted with pentane, filtered through a silica plug and dried. NMR samples were prepared in $CDCl_3$ (600 μL) with PhTMS (0.11 mmol) as an internal standard and ^1H and ^{11}B spectra were obtained on 400 MHz instrument.

See Table A.2 in text for conditions and conversion.

Bibliography

1. Borovik, A. S., Bioinspired Hydrogen Bond Motifs in Ligand Design: The Role of Noncovalent Interactions in Metal Ion Mediated Activation of Dioxygen. *Acc. Chem. Res.* **2005,** *38* (1), 54-61.

2. Hosseinzadeh, P.; Lu, Y., Design and fine-tuning redox potentials of metalloproteins involved in electron transfer in bioenergetics. *Biochimica et Biophysica Acta (BBA) - Bioenergetics* **2016,** *1857* (5), 557-581.

3. Borovik, A. S., Bioinspired hydrogen bond motifs in ligand design: the role of noncovalent interactions in metal ion mediated activation of dioxygen. *Acc. Chem. Res.* **2005,** *38* (1), 54-61.

4. Holm, R. H.; Kennepohl, P.; Solomon, E. I., Structural and Functional Aspects of Metal Sites in Biology. *Chem. Rev.* **1996,** *96* (7), 2239-2314.

5. Liu, J.; Chakraborty, S.; Hosseinzadeh, P.; Yu, Y.; Tian, S.; Petrik, I.; Bhagi, A.; Lu, Y., Metalloproteins Containing Cytochrome, Iron–Sulfur, or Copper Redox Centers. *Chem. Rev.* **2014,** *114* (8), 4366-4469.

6. Warren, J. J.; Mayer, J. M., Moving Protons and Electrons in Biomimetic Systems. *Biochemistry* **2015,** *54* (10), 1863-1878.

7. Fontecilla-Camps, J. C.; Volbeda, A.; Cavazza, C.; Nicolet, Y., Structure/Function Relationships of [NiFe]- and [FeFe]-Hydrogenases. *Chem. Rev.* **2007,** *107* (10), 4273-4303.

8. Lubitz, W.; Ogata, H.; Rüdiger, O.; Reijerse, E., Hydrogenases. *Chem. Rev.* **2014,** *114* (8), 4081-4148.

9. Schindelin, H.; Kisker, C.; Schlessman, J. L.; Howard, J. B.; Rees, D. C., Structure of ADP·AIF4–-stabilized nitrogenase complex and its implications for signal transduction. *Nature* **1997,** *387* (6631), 370-376.

10. Sippel, D.; Einsle, O., The structure of vanadium nitrogenase reveals an unusual bridging ligand. *Nature Chemical Biology* **2017,** *13* (9), 956-960.

11. Sahu, S.; Goldberg, D. P., Activation of Dioxygen by Iron and Manganese Complexes: A Heme and Nonheme Perspective. *J. Am. Chem. Soc.* **2016,** *138* (36), 11410-11428.

12. Zaragoza, J. P. T.; Goldberg, D. P., CHAPTER 1 Dioxygen Binding and Activation Mediated by Transition Metal Porphyrinoid Complexes. In *Dioxygen-dependent Heme Enzymes*, The Royal Society of Chemistry: 2019; pp 1-36.

13. MacBeth, C. E.; Golombek, A. P.; Young, V. G., Jr.; Yang, C.; Kuczera, K.; Hendrich, M. P.; Borovik, A. S., O2 activation by nonheme iron complexes: A monomeric Fe(III)-Oxo complex derived from O2. *Science* **2000,** *289* (5481), 938-41.

14. MacBeth, C. E.; Gupta, R.; Mitchell-Koch, K. R.; Young, V. G.; Lushington, G. H.; Thompson, W. H.; Hendrich, M. P.; Borovik, A. S., Utilization of Hydrogen Bonds To Stabilize M−O(H) Units: Synthesis and Properties of Monomeric Iron and Manganese Complexes with Terminal Oxo and Hydroxo Ligands. *J. Am. Chem. Soc.* **2004,** *126* (8), 2556-2567.

15. Lucas, R. L.; Zart, M. K.; Mukherjee, J.; Sorrell, T. N.; Powell, D. R.; Borovik, A. S., A modular approach toward regulating the secondary coordination sphere of metal ions: differential dioxygen activation assisted by intramolecular hydrogen bonds. *J Am Chem Soc* **2006,** *128* (48), 15476-89.

16. Shook, R. L.; Borovik, A. S., The effects of hydrogen bonds on metal-mediated O2activation and related processes. *Chem. Commun.* **2008,** (46), 6095-6107.

17. Berreau, L. M., Bioinorganic chemistry of group 12 complexes supported by tetradentate tripodal Ligands having internal hydrogen-bond donors. *Eur. J. Inorg. Chem.* **2006,** *2006* (2), 273-283.

18. Dahl, E. W.; Kiernicki, J. J.; Zeller, M.; Szymczak, N. K., Hydrogen Bonds Dictate O_2 Capture and Release within a Zinc Tripod. *J. Am. Chem. Soc.* **2018,** *140* (32), 10075-10079.

19. Burns, K. T.; Marks, W. R.; Cheung, P. M.; Seda, T.; Zakharov, L. N.; Gilbertson, J. D., Uncoupled Redox-Inactive Lewis Acids in the Secondary Coordination Sphere Entice Ligand-Based Nitrite Reduction. *Inorg. Chem.* **2018,** *57* (16), 9601-9610.

20. Kiernicki, J. J.; Zeller, M.; Szymczak, N. K., Hydrazine Capture and N–N Bond Cleavage at Iron Enabled by Flexible Appended Lewis Acids. *J. Am. Chem. Soc.* **2017,** *139* (50), 18194-18197.

21. Kiernicki, J. J.; Zeller, M.; Szymczak, N. K., Examining the Generality of Metal–Ligand Cooperativity Across a Series of First-Row Transition Metals: Capture, Bond Activation, and Stabilization. *Inorg. Chem.* **2020,** *59* (13), 9279-9286.

22. Dahl, E. W.; Dong, H. T.; Szymczak, N. K., Phenylamino derivatives of tris(2-pyridylmethyl)amine: hydrogen-bonded peroxodicopper complexes. *Chem. Commun.* **2018,** *54* (8), 892-895.

23. Manabu, H.; Koichiro, J.; Hideki, M.; Hisahiko, E., Synthesis and Structure of a New Tripodal Polypyridine Copper(II) Complex That Enables to Recognize a Small Molecule. *Chem. Lett.* **1995,** *24* (1), 61-62.

24. Ogo, S.; Wada, S.; Watanabe, Y.; Iwase, M.; Wada, A.; Harata, M.; Jitsukawa, K.; Masuda, H.; Einaga, H., Synthesis, Structure, and Spectroscopic Properties of [Feiii(tnpa)(OH)(PhCOO)]ClO4: A Model Complex for an Active Form of Soybean Lipoxygenase-1. *Angew. Chem. Int. Ed.* **1998,** *37* (15), 2102-2104.

25. Jensen, M. P.; Mehn, M. P.; Que Jr., L., Intramolecular Aromatic Amination through Iron-Mediated Nitrene Transfer. *Angew. Chem. Int. Ed.* **2003,** *42* (36), 4357-4360.

26. Jensen, M. P.; Lange, S. J.; Mehn, M. P.; Que, E. L.; Que, L., Biomimetic Aryl Hydroxylation Derived from Alkyl Hydroperoxide at a Nonheme Iron Center. Evidence for an FeIVO Oxidant. *J. Am. Chem. Soc.* **2003,** *125* (8), 2113-2128.

27. Chang, C. J.; Chng, L. L.; Nocera, D. G., Proton-Coupled O−O Activation on a Redox Platform Bearing a Hydrogen-Bonding Scaffold. *J. Am. Chem. Soc.* **2003,** *125* (7), 1866-1876.

28. Piro, N. A.; Lichterman, M. F.; Harman, W. H.; Chang, C. J., A Structurally Characterized Nitrous Oxide Complex of Vanadium. *J. Am. Chem. Soc.* **2011,** *133* (7), 2108-2111.

29. Harman, W. H.; Chang, C. J., N2O Activation and Oxidation Reactivity from a Non-Heme Iron Pyrrole Platform. *J. Am. Chem. Soc.* **2007,** *129* (49), 15128-15129.

30. Bigi, J. P.; Harman, W. H.; Lassalle-Kaiser, B.; Robles, D. M.; Stich, T. A.; Yano, J.; Britt, R. D.; Chang, C. J., A High-Spin Iron(IV)–Oxo Complex Supported by a Trigonal Nonheme Pyrrolide Platform. *J. Am. Chem. Soc.* **2012,** *134* (3), 1536-1542.

31. Soo, H. S.; Komor, A. C.; Iavarone, A. T.; Chang, C. J., A Hydrogen-Bond Facilitated Cycle for Oxygen Reduction by an Acid- and Base-Compatible Iron Platform. *Inorg. Chem.* **2009,** *48* (21), 10024-10035.

32. Mukherjee, J.; Lucas, R. L.; Zart, M. K.; Powell, D. R.; Day, V. W.; Borovik, A. S., Synthesis, Structure, and Physical Properties for a Series of Monomeric Iron(III) Hydroxo Complexes with Varying Hydrogen-Bond Networks. *Inorg. Chem.* **2008,** *47* (13), 5780-5786.

33. Borovik, A. S., Bioinspired Hydrogen Bond Motifs In Ligand Design: The Role Of Noncovalent Interactions In Metal Ion Mediated Activation Of Dioxygen. *Acc. Chem. Res.* **2005,** *38* (1), 54-61.

34. Lucas, R. L.; Zart, M. K.; Murkerjee, J.; Sorrell, T. N.; Powell, D. R.; Borovik, A. S., A Modular Approach toward Regulating the Secondary Coordination Sphere of Metal Ions: Differential Dioxygen Activation Assisted by Intramolecular Hydrogen Bonds. *J. Am. Chem. Soc.* **2006,** *128* (48), 15476-15489.

35. Sano, Y.; Weitz, A. C.; Ziller, J. W.; Hendrich, M. P.; Borovik, A. S., Unsymmetrical Bimetallic Complexes with MII–(μ-OH)–MIII Cores (MIIMIII = FeIIFeIII, MnIIFeIII, MnIIMnIII): Structural, Magnetic, and Redox Properties. *Inorg. Chem.* **2013,** *52* (18), 10229-10231.

36. Lau, N.; Sano, Y.; Ziller, J. W.; Borovik, A. S., Terminal NiII−OH/−OH2 complexes in trigonal bipyramidal geometries derived from H2O. *Polyhedron* **2017,** *125,* 179-185.

37. Shook, R. L.; Borovik, A. S., Role of the Secondary Coordination Sphere in Metal-Mediated Dioxygen Activation. *Inorganic Chemistry* **2010,** *49* (8), 3646-3660.

38. Ford, C. L.; Park, Y. J.; Matson, E. M.; Gordon, Z.; Fout, A. R., A bioinspired iron catalyst for nitrate and perchlorate reduction. *Science* **2016,** *354* (6313), 741-743.

39. Matson, E. M.; Bertke, J. A.; Fout, A. R., Isolation of iron(II) aqua and hydroxyl complexes featuring a tripodal H-bond donor and acceptor ligand. *Inorg. Chem.* **2014,** *53* (9), 4450-8.

40. Gordon, Z.; Miller, T. J.; Leahy, C. A.; Matson, E. M.; Burgess, M.; Drummond, M. J.; Popescu, C. V.; Smith, C. M.; Lord, R. L.; Rodriguez-Lopez, J.; Fout, A. R., Characterization of Terminal Iron(III)-Oxo and Iron(III)-Hydroxo Complexes Derived from O2 Activation. *Inorg. Chem.* **2019,** *58* (23), 15801-15811.

41. Matson, E. M.; Park, Y. J.; Fout, A. R., Facile Nitrite Reduction in a Non-heme Iron System: Formation of an Iron(III)-Oxo. *J. Am. Chem. Soc.* **2014,** *136* (50), 17398-17401.

42. Widger, L. R.; Davies, C. G.; Yang, T.; Siegler, M. A.; Troeppner, O.; Jameson, G. N. L.; Ivanović-Burmazović, I.; Goldberg, D. P., Dramatically Accelerated Selective Oxygen-Atom Transfer by a Nonheme Iron(IV)-Oxo Complex: Tuning of the First and Second Coordination Spheres. *J. Am. Chem. Soc.* **2014,** *136* (7), 2699-2702.

43. Yadav, V.; Gordon, J. B.; Siegler, M. A.; Goldberg, D. P., Dioxygen-Derived Nonheme Mononuclear Fe(III)(OH) Complex and Its Reactivity with Carbon Radicals. *J Am Chem Soc* **2019,** *141* (26), 10148-10153.

44. Moore, C. M.; Szymczak, N. K., 6,6′-Dihydroxy terpyridine: a proton-responsive bifunctional ligand and its application in catalytic transfer hydrogenation of ketones. *Chem. Commun.* **2013,** *49* (4), 400-402.

45. Moore, C. M.; Quist, D. A.; Kampf, J. W.; Szymczak, N. K., A 3-fold-symmetric ligand based on 2-hydroxypyridine: regulation of ligand binding by hydrogen bonding. *Inorg. Chem.* **2014,** *53* (7), 3278-80.

46. Dahl, E. W.; Szymczak, N. K., Hydrogen Bonds Dictate the Coordination Geometry of Copper: Characterization of a Square-Planar Copper(I) Complex. *Angew. Chem. Int. Ed.* **2016,** *55* (9), 3101-3105.

47. Shanahan, J. P.; Mullis, D. M.; Zeller, M.; Szymczak, N. K., Reductively Stable Hydrogen-Bonding Ligands Featuring Appended CF2–H Units. *J. Am. Chem. Soc.* **2020,** *142* (19), 8809-8817.

48. Poulos, T. L.; Li, H.; Raman, C. S., Heme-mediated oxygen activation in biology: cytochrome c oxidase and nitric oxide synthase. *Curr. Opin. Chem. Biol.* **1999,** *3* (2), 131-137.

49. Tinberg, C. E.; Lippard, S. J., Dioxygen Activation in Soluble Methane Monooxygenase. *Acc. Chem. Res.* **2011,** *44* (4), 280-288.

50. Selke, M.; Sisemore, M. F.; Ho, R. Y. N.; Wertz, D. L.; Valentine, J. S., Dioxygen activation by iron complexes. The search for reactive intermediates. *J. Mol. Catal. A: Chem.* **1997,** *117* (1), 71-82.

51. Faponle, A. S.; de Visser, S. P., Chapter Four - The Role of Nonheme Transition Metal-Oxo, -Peroxo, and -Superoxo Intermediates in Enzyme Catalysis and Reactions of Bioinspired Complexes. In *Adv. Inorg. Chem.*, van Eldik, R.; Hubbard, C. D., Eds. Academic Press: 2017; Vol. 70, pp 167-194.

52. Boer, J. L.; Mulrooney, S. B.; Hausinger, R. P., Nickel-dependent metalloenzymes. *Arch Biochem Biophys* **2014,** *544*, 142-52.

53. Solomon, E. I.; Chen, P.; Metz, M.; Lee, S.-K.; Palmer, A. E., Oxygen Binding, Activation, and Reduction to Water by Copper Proteins. *Angew. Chem. Int. Ed.* **2001,** *40* (24), 4570-4590.

54. Quist, D. A.; Diaz, D. E.; Liu, J. J.; Karlin, K. D., Activation of dioxygen by copper metalloproteins and insights from model complexes. *JBIC Journal of Biological Inorganic Chemistry* **2017,** *22* (2), 253-288.

55. Oloo, W. N.; Feng, Y.; Iyer, S.; Parmelee, S.; Xue, G.; Que, L., Cyclohexene as a substrate probe for the nature of the high-valent iron-oxo oxidant in Fe(TPA)-catalyzed oxidations. *New J. Chem.* **2013,** *37* (11), 3411.

56. Chen, K.; Que, L., Stereospecific Alkane Hydroxylation by Non-Heme Iron Catalysts: Mechanistic Evidence for an FeVO Active Species. *J. Am. Chem. Soc.* **2001,** *123* (26), 6327-6337.

57. Kim, J.; Harrison, R. G.; Kim, C.; Que, L., Fe(TPA)-Catalyzed Alkane Hydroxylation. Metal-Based Oxidation vs Radical Chain Autoxidation. *J. Am. Chem. Soc.* **1996,** *118* (18), 4373-4379.

58. Larson, V. A.; Battistella, B.; Ray, K.; Lehnert, N.; Nam, W., Iron and manganese oxo complexes, oxo wall and beyond. *Nature Reviews Chemistry* **2020,** *4* (8), 404-419.

59. Oloo, W. N.; Que, L., Bioinspired Nonheme Iron Catalysts for C–H and C═C Bond Oxidation: Insights into the Nature of the Metal-Based Oxidants. *Acc. Chem. Res.* **2015,** *48* (9), 2612-2621.

60. Wang, K.; Huang, J.; Chen, H.; Wang, Y.; Song, S., Recent advances in electrochemical 2e oxygen reduction reaction for on-site hydrogen peroxide production and beyond. *Chem. Commun.* **2020,** *56* (81), 12109-12121.

61. Kim, S. O.; Sastri, C. V.; Seo, M. S.; Kim, J.; Nam, W., Dioxygen Activation and Catalytic Aerobic Oxidation by a Mononuclear Nonheme Iron(II) Complex. *J. Am. Chem. Soc.* **2005,** *127* (12), 4178-4179.

62. Surendhran, R.; D'Arpino, A. A.; Sciscent, B. Y.; Cannella, A. F.; Friedman, A. E.; MacMillan, S. N.; Gupta, R.; Lacy, D. C., Deciphering the mechanism of O2 reduction with electronically tunable non-heme iron enzyme model complexes. *Chem. Sci.* **2018,** *9* (26), 5773-5780.

63. Rettenmeier, C. A.; Wadepohl, H.; Gade, L. H., Electronic structure and reactivity of nickel(I) pincer complexes: their aerobic transformation to peroxo species and site selective C–H oxygenation. *Chem. Sci.* **2016,** *7* (6), 3533-3542.

64. Ching, W.-M.; Zhou, A.; Klein, J. E. M. N.; Fan, R.; Knizia, G.; Cramer, C. J.; Guo, Y.; Que, L., Characterization of the Fleeting Hydroxoiron(III) Complex of the Pentadentate TMC-py Ligand. *Inorg. Chem.* **2017,** *56* (18), 11129-11140.

65. Hong, S.; Lee, Y.-M.; Cho, K.-B.; Seo, M. S.; Song, D.; Yoon, J.; Garcia-Serres, R.; Clémancey, M.; Ogura, T.; Shin, W.; Latour, J.-M.; Nam, W., Conversion of high-spin iron(iii)–alkylperoxo to iron(iv)–oxo species via O–O bond homolysis in nonheme iron models. *Chem. Sci.* **2014,** *5* (1), 156-162.

66. Kieber-Emmons, M. T.; Annaraj, J.; Seo, M. S.; Van Heuvelen, K. M.; Tosha, T.; Kitagawa, T.; Brunold, T. C.; Nam, W.; Riordan, C. G., Identification of an "End-on" Nickel−Superoxo Adduct, [Ni(tmc)(O2)]+. *J. Am. Chem. Soc.* **2006,** *128* (44), 14230-14231.

67. Cho, J.; Kang, H. Y.; Liu, L. V.; Sarangi, R.; Solomon, E. I.; Nam, W., Mononuclear nickel(II)-superoxo and nickel(III)-peroxo complexes bearing a common macrocyclic TMC ligand. *Chem Sci* **2013,** *4* (4), 1502-1508.

68. Kryatov, S. V.; Taktak, S.; Korendovych, I. V.; Rybak-Akimova, E. V.; Kaizer, J.; Torelli, S.; Shan, X.; Mandal, S.; MacMurdo, V. L.; Mairata i Payeras, A.; Que, L., Jr., Dioxygen binding to complexes with Fe(II)2(mu-OH)2 cores: steric control of activation barriers and O2-adduct formation. *Inorg. Chem.* **2005,** *44* (1), 85-99.

69. Theopold, K. H.; Reinaud, O. M.; Doren, D.; Konecny, R., Dioxygen activation with sterically hindered tris(pyrazolyl)borate cobalt complexes. In *Stud. Surf. Sci. Catal.*, Grasselli, R. K.; Oyama, S. T.; Gaffney, A. M.; Lyons, J. E., Eds. Elsevier: 1997; Vol. 110, pp 1081-1088.

70. Liu, Y.; Lau, T. C., Activation of Metal Oxo and Nitrido Complexes by Lewis Acids. *J Am Chem Soc* **2019,** *141* (9), 3755-3766.

71. Jasniewski, A. J.; Que, L., Jr., Dioxygen Activation by Nonheme Diiron Enzymes: Diverse Dioxygen Adducts, High-Valent Intermediates, and Related Model Complexes. *Chem. Rev.* **2018,** *118* (5), 2554-2592.

72. Li, F.; Van Heuvelen, K. M.; Meier, K. K.; Münck, E.; Que, L., Sc3+-Triggered Oxoiron(IV) Formation from O2 and its Non-Heme Iron(II) Precursor via a Sc3+–Peroxo–Fe3+ Intermediate. *J. Am. Chem. Soc.* **2013,** *135* (28), 10198-10201.

73. Goldsmith, C. R.; Stack, T. D. P., Hydrogen Atom Abstraction by a Mononuclear Ferric Hydroxide Complex: Insights into the Reactivity of Lipoxygenase. *Inorg. Chem.* **2006,** *45* (15), 6048-6055.

74. Ogo, S.; Yamahara, R.; Roach, M.; Suenobu, T.; Aki, M.; Ogura, T.; Kitagawa, T.; Masuda, H.; Fukuzumi, S.; Watanabe, Y., Structural and spectroscopic features of a cis (hydroxo)-Fe(III)-(carboxylato) configuration as an active site model for lipoxygenases. *Inorg. Chem.* **2002,** *41* (21), 5513-20.

75. Gibson, D. T.; Parales, R. E., Aromatic hydrocarbon dioxygenases in environmental biotechnology. *Curr. Opin. Biotechnol.* **2000,** *11* (3), 236-243.

76. Sacramento, J. J. D.; Goldberg, D. P., Oxidation of an indole substrate by porphyrin iron(iii) superoxide: relevance to indoleamine and tryptophan 2,3-dioxygenases. *Chem. Commun.* **2020,** *56* (20), 3089-3092.

77. Furukawa, K., Engineering dioxygenases for efficient degradation of environmental pollutants. *Curr. Opin. Biotechnol.* **2000,** *11* (3), 244-249.

78. Puri, M.; Que, L., Toward the Synthesis of More Reactive S = 2 Non-Heme Oxoiron(IV) Complexes. *Acc. Chem. Res.* **2015,** *48* (8), 2443-2452.

79. Lim, M. H.; Rohde, J. U.; Stubna, A.; Bukowski, M. R.; Costas, M.; Ho, R. Y.; Munck, E.; Nam, W.; Que, L., Jr., An FeIV=O complex of a tetradentate tripodal nonheme ligand. *Proc Natl Acad Sci U S A* **2003,** *100* (7), 3665-70.

80. Barman, S. K.; Jones, J. R.; Sun, C.; Hill, E. A.; Ziller, J. W.; Borovik, A. S., Regulating the Basicity of Metal-Oxido Complexes with a Single Hydrogen Bond and Its Effect on C-H Bond Cleavage. *J Am Chem Soc* **2019,** *141* (28), 11142-11150.

81. Park, Y. J.; Ziller, J. W.; Borovik, A. S., The Effects of Redox-Inactive Metal Ions on the Activation of Dioxygen: Isolation and Characterization of a Heterobimetallic Complex Containing a MnIII–(μ-OH)–CaII Core. *J. Am. Chem. Soc.* **2011,** *133* (24), 9258-9261.

82. Powell-Jia, D.; Ziller, J. W.; DiPasquale, A. G.; Rheingold, A. L.; Borovik, A. S., A structure and reactivity analysis of monomeric Ni(ii)–hydroxo complexes prepared from water. *Dalton Transactions* **2009,** (16), 2986-2992.

83. Park, Y. J.; Cook, S. A.; Sickerman, N. S.; Sano, Y.; Ziller, J. W.; Borovik, A. S., Heterobimetallic complexes with MIII-(μ-OH)-MII cores (MIII = Fe, Mn, Ga; MII = Ca, Sr, and Ba): structural, kinetic, and redox properties. *Chem. Sci.* **2013,** *4* (2), 717-726.

84. Lee, J. L.; Ross, D. L.; Barman, S. K.; Ziller, J. W.; Borovik, A. S., C–H Bond Cleavage by Bioinspired Nonheme Metal Complexes. *Inorg. Chem.* **2021,** *60* (18), 13759-13783.

85. Chiang, C.-W.; Kleespies, S. T.; Stout, H. D.; Meier, K. K.; Li, P.-Y.; Bominaar, E. L.; Que, L.; Münck, E.; Lee, W.-Z., Characterization of a Paramagnetic Mononuclear Nonheme Iron-Superoxo Complex. *J. Am. Chem. Soc.* **2014,** *136* (31), 10846-10849.

86. Fukuzumi, S.; Lee, Y. M.; Nam, W., Structure and reactivity of the first-row d-block metal-superoxo complexes. *Dalton Trans* **2019,** *48* (26), 9469-9489.

87. Shan, X.; Que, L.; Gray, H. B., Intermediates in the Oxygenation of a Nonheme Diiron(II) Complex, Including the First Evidence for a Bound Superoxo Species. *Proceedings of the National Academy of Sciences of the United States of America* **2005,** *102* (15), 5340-5345.

88. Kim, J.; Kim, C.; Harrison, R. G.; Wilkinson, E. C.; Que, L., Fe(TPA)-catalyzed alkane hydroxylation can be a metal-based oxidation. *J. Mol. Catal. A: Chem.* **1997,** *117* (1), 83-89.

89. Serrano-Plana, J.; Acuña-Parés, F.; Dantignana, V.; Oloo, W. N.; Castillo, E.; Draksharapu, A.; Whiteoak, C. J.; Martin-Diaconescu, V.; Basallote, M. G.; Luis, J. M.; Que Jr., L.; Costas, M.; Company, A., Acid-Triggered O−O Bond Heterolysis of a Nonheme FeIII(OOH) Species for the Stereospecific Hydroxylation of Strong C−H Bonds. *Chemistry – A European Journal* **2018,** *24* (20), 5331-5340.

90. Mairata i Payeras, A.; Ho, R. Y. N.; Fujita, M.; Que, J., Lawrence, The Reaction of [FeII(tpa)] with H2O2 in Acetonitrile and Acetone—Distinct Intermediates and Yet Similar Catalysis. *Chemistry – A European Journal* **2004,** *10* (20), 4944-4953.

91. Oh, N. Y.; Seo, M. S.; Lim, M. H.; Consugar, M. B.; Park, M. J.; Rohde, J.-U.; Han, J.; Kim, K. M.; Kim, J.; Que, J. L.; Nam, W., Self-hydroxylation of perbenzoic acids at a nonheme iron(ii) center. *Chem. Commun.* **2005,** (45), 5644-5646.

92. Morimoto, Y.; Hanada, S.; Kamada, R.; Fukatsu, A.; Sugimoto, H.; Itoh, S., Hydroxylation of Unactivated C(sp3)–H Bonds with m-Chloroperbenzoic Acid Catalyzed by an Iron(III) Complex Supported by a Trianionic Planar Tetradentate Ligand. *Inorg. Chem.* **2021**.

93. Cho, K. B.; Hirao, H.; Shaik, S.; Nam, W., To rebound or dissociate? This is the mechanistic question in C-H hydroxylation by heme and nonheme metal-oxo complexes. *Chem Soc Rev* **2016,** *45* (5), 1197-210.

94. Bassan, A.; Blomberg, M. R. A.; Siegbahn, P. E. M.; Que, L., Two Faces of a Biomimetic Non-Heme HO□FeV□O Oxidant: Olefin Epoxidation versus cis-Dihydroxylation. *Angew. Chem. Int. Ed.* **2005,** *44* (19), 2939-2941.

95. Mas-Ballesté, R.; Que, L., Iron-Catalyzed Olefin Epoxidation in the Presence of Acetic Acid: Insights into the Nature of the Metal-Based Oxidant. *J. Am. Chem. Soc.* **2007,** *129* (51), 15964-15972.

96. Borrell, M.; Costas, M., Mechanistically Driven Development of an Iron Catalyst for Selective Syn-Dihydroxylation of Alkenes with Aqueous Hydrogen Peroxide. *J Am Chem Soc* **2017,** *139* (36), 12821-12829.

97. Ayad, M.; Gebbink, R. J. M. K.; Mest, Y. L.; Schollhammer, P.; Poul, N. L.; Pétillon, F. Y.; Mandon, D., Mononuclear iron(II) complexes containing a tripodal and macrocyclic nitrogen ligand: synthesis, reactivity and application in cyclohexane oxidation catalysis. *Dalton Transactions* **2018,** *47* (43), 15596-15612.

98. Hsu, H.-F.; Dong, Y.; Shu, L.; Young, V. G.; Que, L., Crystal Structure of a Synthetic High-Valent Complex with an Fe2(μ-O)2 Diamond Core. Implications for the Core Structures of Methane Monooxygenase Intermediate Q and Ribonucleotide Reductase Intermediate X. *J. Am. Chem. Soc.* **1999,** *121* (22), 5230-5237.

99. Sekino, M.; Furutachi, H.; Tasaki, K.; Ishikawa, T.; Mori, S.; Fujinami, S.; Akine, S.; Sakata, Y.; Nomura, T.; Ogura, T.; Kitagawa, T.; Suzuki, M., New mechanistic insight into intramolecular arene hydroxylation initiated by (μ-1,2-peroxo)diiron(iii) complexes with dinucleating ligands. *Dalton Transactions* **2016,** *45* (2), 469-473.

100. Goetz, M. K.; Hill, E. A.; Filatov, A. S.; Anderson, J. S., Isolation of a Terminal Co(III)-Oxo Complex. *J Am Chem Soc* **2018,** *140* (41), 13176-13180.

101. Hill, E. A.; Kelty, M. L.; Filatov, A. S.; Anderson, J. S., Isolable iodosylarene and iodoxyarene adducts of Co and their O-atom transfer and C–H activation reactivity. *Chem. Sci.* **2018,** *9* (19), 4493-4499.

102. McNeece, A. J.; Jesse, K.; Xie, J.; Filatov, A. S.; Anderson, J. S., Generation and Oxidative Reactivity of a Ni(II) Superoxo Complex via Ligand-Based Redox Non-Innocence. *J. Am. Chem. Soc.* **2020**.

103. Goetz, M. K.; Anderson, J. S., Experimental Evidence for p Ka-Driven Asynchronicity in C-H Activation by a Terminal Co(III)-Oxo Complex. *J Am Chem Soc* **2019,** *141* (9), 4051-4062.

104. Gordon, J. B.; Vilbert, A. C.; DiMucci, I. M.; MacMillan, S. N.; Lancaster, K. M.; Moënne-Loccoz, P.; Goldberg, D. P., Activation of Dioxygen by a Mononuclear Nonheme Iron Complex: Sequential Peroxo, Oxo, and Hydroxo Intermediates. *J. Am. Chem. Soc.* **2019,** *141* (44), 17533-17547.

105. Yadav, V.; Gordon, J. B.; Siegler, M. A.; Goldberg, D. P., Dioxygen-Derived Nonheme Mononuclear FeIII(OH) Complex and Its Reactivity with Carbon Radicals. *J. Am. Chem. Soc.* **2019**.

106. Lehnert, N.; Musselman, B. W.; Seefeldt, L. C., Grand challenges in the nitrogen cycle. *Chem. Soc. Rev.* **2021,** *50* (6), 3640-3646.

107. Fukuda, Y.; Tse, K. M.; Nakane, T.; Nakatsu, T.; Suzuki, M.; Sugahara, M.; Inoue, S.; Masuda, T.; Yumoto, F.; Matsugaki, N.; Nango, E.; Tono, K.; Joti, Y.; Kameshima, T.; Song, C.; Hatsui, T.; Yabashi, M.; Nureki, O.; Murphy, M. E. P.; Inoue, T.; Iwata, S.; Mizohata, E., Redox-coupled proton transfer mechanism in nitrite reductase revealed by femtosecond crystallography. *Proceedings of the National Academy of Sciences* **2016,** *113* (11), 2928-2933.

108. Lundberg, J. O.; Weitzberg, E.; Gladwin, M. T., The nitrate–nitrite–nitric oxide pathway in physiology and therapeutics. *Nature Reviews Drug Discovery* **2008,** *7* (2), 156-167.

109. Kurtz, J. D. M., Flavo-diiron enzymes: nitric oxide or dioxygen reductases? *Dalton Transactions* **2007,** (37), 4115-4121.

110. Antonyuk, S. V.; Strange, R. W.; Sawers, G.; Eady, R. R.; Hasnain, S. S., Atomic resolution structures of resting-state, substrate- and product-complexed Cu-nitrite reductase provide insight into catalytic mechanism. *Proceedings of the National Academy of Sciences of the United States of America* **2005,** *102* (34), 12041-12046.

111. Kumar, M.; Dixon, N. A.; Merkle, A. C.; Zeller, M.; Lehnert, N.; Papish, E. T., Hydrotris(triazolyl)borate Complexes as Functional Models for Cu Nitrite Reductase: The Electronic Influence of Distal Nitrogens. *Inorg. Chem.* **2012,** *51* (13), 7004-7006.

112. Hsu, S. C. N.; Chang, Y.-L.; Chuang, W.-J.; Chen, H.-Y.; Lin, I. J.; Chiang, M. Y.; Kao, C.-L.; Chen, H.-Y., Copper(I) Nitro Complex with an Anionic [HB(3,5-Me2Pz)3]- Ligand: A Synthetic Model for the Copper Nitrite Reductase Active Site. *Inorg. Chem.* **2012,** *51* (17), 9297-9308.

113. Hunt, A. P.; Batka, A. E.; Hosseinzadeh, M.; Gregory, J. D.; Haque, H. K.; Ren, H.; Meyerhoff, M. E.; Lehnert, N., Nitric Oxide Generation on Demand for Biomedical Applications via Electrocatalytic Nitrite Reduction by Copper BMPA- and BEPA-Carboxylate Complexes. *ACS Catalysis* **2019,** *9* (9), 7746-7758.

114. Cioncoloni, G.; Roger, I.; Wheatley, P. S.; Wilson, C.; Morris, R. E.; Sproules, S.; Symes, M. D., Proton-Coupled Electron Transfer Enhances the Electrocatalytic Reduction of Nitrite to NO in a Bioinspired Copper Complex. *ACS Catalysis* **2018**, 5070-5084.

115. Chandra Maji, R.; Mishra, S.; Bhandari, A.; Singh, R.; Olmstead, M. M.; Patra, A. K., A Copper(II) Nitrite That Exhibits Change of Nitrite Binding Mode and Formation of Copper(II) Nitrosyl Prior to Nitric Oxide Evolution. *Inorg. Chem.* **2018**.

116. Sakhaei, Z.; Kundu, S.; Donnelly, J. M.; Bertke, J. A.; Kim, W. Y.; Warren, T. H., Nitric oxide release via oxygen atom transfer from nitrite at copper(ii). *Chem. Commun.* **2017,** *53* (3), 549-552.

117. Moore, C. M.; Szymczak, N. K., Nitrite reduction by copper through ligand-mediated proton and electron transfer. *Chem. Sci.* **2015,** *6* (6), 3373-3377.

118. Ichikawa, K.; Matsumoto, T.; Ogo, S., Critical aspects of [NiFe]hydrogenase ligand composition. *Dalton Trans* **2009,** (22), 4304-9.

119. Perotto, C. U.; Marshall, G.; Jones, G. J.; Stephen Davies, E.; Lewis, W.; McMaster, J.; Schroder, M., A Ni(i)Fe(ii) analogue of the Ni-L state of the active site of the [NiFe] hydrogenases. *Chem Commun (Camb)* **2015,** *51* (95), 16988-91.

120. Liao, R.-Z.; Siegbahn, P. E. M., Energetics for the Mechanism of Nickel-Containing Carbon Monoxide Dehydrogenase. *Inorg. Chem.* **2019,** *58* (12), 7931-7938.

121. Manesis, A. C.; Musselman, B. W.; Keegan, B. C.; Shearer, J.; Lehnert, N.; Shafaat, H. S., A Biochemical Nickel(I) State Supports Nucleophilic Alkyl Addition: A Roadmap for Methyl Reactivity in Acetyl Coenzyme A Synthase. *Inorg. Chem.* **2019,** *58* (14), 8969-8982.

122. Kieber-Emmons, M. T.; Riordan, C. G., Dioxygen activation at monovalent nickel. *Acc. Chem. Res.* **2007,** *40* (7), 618-25.

123. Gwak, J.; Ahn, S.; Baik, M.-H.; Lee, Y., One metal is enough: a nickel complex reduces nitrate anions to nitrogen gas. *Chem. Sci.* **2019,** *10* (18), 4767-4774.

124. Maroney, M. J.; Ciurli, S., Nonredox Nickel Enzymes. *Chem. Rev.* **2014,** *114* (8), 4206-4228.

125. Wilson, J. R.; Zeller, M.; Szymczak, N. K., Hydrogen-bonded nickel(i) complexes. *Chem. Commun.* **2021,** *57* (6), 753-756.

126. Fukuzumi, S.; Lee, Y.-M.; Nam, W., Structure and reactivity of the first-row d-block metal-superoxo complexes. *Dalton Transactions* **2019,** *48* (26), 9469-9489.

127. Desbouis, D.; Troitsky, I. P.; Belousoff, M. J.; Spiccia, L.; Graham, B., Copper(II), zinc(II) and nickel(II) complexes as nuclease mimetics. *Coord. Chem. Rev.* **2012,** *256* (11), 897-937.

128. Can, M.; Armstrong, F. A.; Ragsdale, S. W., Structure, Function, and Mechanism of the Nickel Metalloenzymes, CO Dehydrogenase, and Acetyl-CoA Synthase. *Chem. Rev.* **2014,** *114* (8), 4149-4174.

129. Shafaat, H. S.; Rüdiger, O.; Ogata, H.; Lubitz, W., [NiFe] hydrogenases: A common active site for hydrogen metabolism under diverse conditions. *Biochimica et Biophysica Acta (BBA) - Bioenergetics* **2013,** *1827* (8), 986-1002.

130. Fichtner, C.; Laurich, C.; Bothe, E.; Lubitz, W., Spectroelectrochemical Characterization of the [NiFe] Hydrogenase of Desulfovibrio vulgaris Miyazaki F. *Biochemistry* **2006,** *45* (32), 9706-9716.

131. Lindahl, P. A.; Münck, E.; Ragsdale, S. W., CO dehydrogenase from Clostridium thermoaceticum. EPR and electrochemical studies in CO2 and argon atmospheres. *J. Biol. Chem.* **1990,** *265* (7), 3873-3879.

132. Ragsdale, S. W., Life with Carbon Monoxide. *Crit. Rev. Biochem. Mol. Biol.* **2004,** *39* (3), 165-195.

133. Kyritsis, P.; Dennison, C.; Sykes, A. G., Structure and Reactivity of the Blue Copper Proteins. In *Bioinorganic Chemistry: An Inorganic Perspective of Life*, Kessissoglou, D. P., Ed. Springer Netherlands: Dordrecht, 1995; pp 67-76.

134. Tasker, S. Z.; Standley, E. A.; Jamison, T. F., Recent advances in homogeneous nickel catalysis. *Nature* **2014,** *509* (7500), 299-309.

135. Skubi, K. L.; Blum, T. R.; Yoon, T. P., Dual Catalysis Strategies in Photochemical Synthesis. *Chem. Rev.* **2016,** *116* (17), 10035-10074.

136. Verschueren, R. H.; De Borggraeve, W. M., Electrochemistry and Photoredox Catalysis: A Comparative Evaluation in Organic Synthesis. *Molecules* **2019,** *24* (11), 2122.

137. Monos, T. M.; Stephenson, C. R. J., Photoredox Catalysis of Iridium(III)-Based Photosensitizers. In *Iridium(III) in Optoelectronic and Photonics Applications*, 2017; pp 541-581.

138. Ren, H.; Li, G.-F.; Zhu, B.; Lv, X.-D.; Yao, L.-S.; Wang, X.-L.; Su, Z.-M.; Guan, W., How Does Iridium(III) Photocatalyst Regulate Nickel(II) Catalyst in Metallaphotoredox-Catalyzed C–S Cross-Coupling? Theoretical and Experimental Insights. *ACS Catalysis* **2019,** *9* (5), 3858-3865.

139. Groves, J. T., High-valent iron in chemical and biological oxidations. *J. Inorg. Biochem.* **2006,** *100* (4), 434-447.

140. Plesniak, M. P.; Huang, H.-M.; Procter, D. J., Radical cascade reactions triggered by single electron transfer. *Nature Reviews Chemistry* **2017,** *1* (10), 0077.

141. Han, F. S., Transition-metal-catalyzed Suzuki-Miyaura cross-coupling reactions: a remarkable advance from palladium to nickel catalysts. *Chem Soc Rev* **2013,** *42* (12), 5270-98.

142. Morris, R. H., Brønsted–Lowry Acid Strength of Metal Hydride and Dihydrogen Complexes. *Chem. Rev.* **2016,** *116* (15), 8588-8654.

143. Creutz, S. E.; Peters, J. C., Exploring secondary-sphere interactions in Fe–NxHy complexes relevant to N2 fixation. *Chem. Sci.* **2017,** *8* (3), 2321-2328.

144. Weiss, C. J.; Egbert, J. D.; Chen, S.; Helm, M. L.; Bullock, R. M.; Mock, M. T., Protonation Studies of a Tungsten Dinitrogen Complex Supported by a Diphosphine Ligand Containing a Pendant Amine. *Organometallics* **2014,** *33* (9), 2189-2200.

145. Shanahan, J. P.; Szymczak, N. K., Hydrogen Bonding to a Dinitrogen Complex at Room Temperature: Impacts on N2 Activation. *J. Am. Chem. Soc.* **2019,** *141* (21), 8550-8556.

146. Wongnate, T.; Sliwa, D.; Ginovska, B.; Smith, D.; Wolf, M. W.; Lehnert, N.; Raugei, S.; Ragsdale, S. W., The radical mechanism of biological methane synthesis by methyl-coenzyme M reductase. *Science* **2016,** *352* (6288), 953-958.

147. Hoffman, B. M.; Lukoyanov, D.; Dean, D. R.; Seefeldt, L. C., Nitrogenase: A Draft Mechanism. *Acc. Chem. Res.* **2013,** *46* (2), 587-595.

148. Hoffman, B. M.; Lukoyanov, D.; Yang, Z.-Y.; Dean, D. R.; Seefeldt, L. C., Mechanism of Nitrogen Fixation by Nitrogenase: The Next Stage. *Chem. Rev.* **2014,** *114* (8), 4041-4062.

149. Volbeda, A.; Fontecilla-Camps, J. C., The active site and catalytic mechanism of NiFe hydrogenases. *Dalton Transactions* **2003,** (21), 4030-4038.

150. Bhattacharya, P.; Heiden, Z. M.; Wiedner, E. S.; Raugei, S.; Piro, N. A.; Kassel, W. S.; Bullock, R. M.; Mock, M. T., Ammonia Oxidation by Abstraction of Three Hydrogen Atoms from a Mo–NH3 Complex. *J. Am. Chem. Soc.* **2017,** *139* (8), 2916-2919.

151. Geri, J. B.; Shanahan, J. P.; Szymczak, N. K., Testing the Push-Pull Hypothesis: Lewis Acid Augmented N2 Activation at Iron. *J. Am. Chem. Soc.* **2017,** *139* (16), 5952-5956.

152. Han, F.-S., Transition-metal-catalyzed Suzuki–Miyaura cross-coupling reactions: a remarkable advance from palladium to nickel catalysts. *Chem. Soc. Rev.* **2013,** *42* (12), 5270-5298.

153. Zimmermann, P.; Limberg, C., Activation of Small Molecules at Nickel(I) Moieties. *J. Am. Chem. Soc.* **2017,** *139* (12), 4233-4242.

154. Nag, K.; Chakravorty, A., Monovalent, trivalent and tetravalent nickel. *Coord. Chem. Rev.* **1980,** *33* (2), 87-147.

155. Lin, C. Y.; Power, P. P., Complexes of Ni(i): a "rare" oxidation state of growing importance. *Chem Soc Rev* **2017,** *46* (17), 5347-5399.

156. Shima, S.; Pilak, O.; Vogt, S.; Schick, M.; Stagni, M. S.; Meyer-Klaucke, W.; Warkentin, E.; Thauer, R. K.; Ermler, U., The crystal structure of [Fe]-hydrogenase reveals the geometry of the active site. *Science* **2008,** *321* (5888), 572-5.

157. Hiromoto, T.; Warkentin, E.; Moll, J.; Ermler, U.; Shima, S., The Crystal Structure of an Fe -Hydrogenase-Substrate Complex Reveals the Framework for H-2 Activation. *Angew. Chem. Int. Ed.* **2009,** *48* (35), 6457-6460.

158. Huang, G. F.; Wagner, T.; Wodrich, M. D.; Ataka, K.; Bill, E.; Ermler, U.; Hu, X. L.; Shima, S., The atomic-resolution crystal structure of activated [Fe]-hydrogenase. *Nat Catal* **2019,** *2* (6), 537-543.

159. Moore, C. M.; Dahl, E. W.; Szymczak, N. K., Beyond H2: exploiting 2-hydroxypyridine as a design element from [Fe]-hydrogenase for energy-relevant catalysis. *Curr. Opin. Chem. Biol.* **2015,** *25,* 9-17.

160. Jeoung, J.-H.; Dobbek, H., Carbon Dioxide Activation at the Ni,Fe-Cluster of Anaerobic Carbon Monoxide Dehydrogenase. *Science* **2007,** *318* (5855), 1461-1464.

161. Han, Z.; Horak, K. T.; Lee, H. B.; Agapie, T., Tetranuclear Manganese Models of the OEC Displaying Hydrogen Bonding Interactions: Application to Electrocatalytic Water Oxidation to Hydrogen Peroxide. *J. Am. Chem. Soc.* **2017,** *139* (27), 9108-9111.

162. Yadav, V.; Gordon, J. B.; Siegler, M. A.; Goldberg, D. P., Dioxygen-Derived Nonheme Mononuclear FeIII(OH) Complex and Its Reactivity with Carbon Radicals. *J. Am. Chem. Soc.* **2019,** *141* (26), 10148-10153.

163. Dahl, E. W.; Louis-Goff, T.; Szymczak, N. K., Second sphere ligand modifications enable a recyclable catalyst for oxidant-free alcohol oxidation to carboxylates. *Chem. Commun.* **2017,** *53* (14), 2287-2289.

164. Nichols, E. M.; Derrick, J. S.; Nistanaki, S. K.; Smith, P. T.; Chang, C. J., Positional effects of second-sphere amide pendants on electrochemical CO2 reduction catalyzed by iron porphyrins. *Chem. Sci.* **2018,** *9* (11), 2952-2960.

165. Delgado, M.; Gilbertson, J. D., Ligand-based reduction of nitrate to nitric oxide utilizing a proton-responsive secondary coordination sphere. *Chem. Commun.* **2017,** *53* (81), 11249-11252.

166. Costentin, C.; Drouet, S.; Robert, M.; Savéant, J.-M., A Local Proton Source Enhances CO<sub>2</sub> Electroreduction to CO by a Molecular Fe Catalyst. *Science* **2012,** *338* (6103), 90.

167. Azcarate, I.; Costentin, C.; Robert, M.; Savéant, J.-M., Through-Space Charge Interaction Substituent Effects in Molecular Catalysis Leading to the Design of the Most Efficient Catalyst of CO2-to-CO Electrochemical Conversion. *J. Am. Chem. Soc.* **2016,** *138* (51), 16639-16644.

168. Pegis, M. L.; McKeown, B. A.; Kumar, N.; Lang, K.; Wasylenko, D. J.; Zhang, X. P.; Raugei, S.; Mayer, J. M., Homogenous Electrocatalytic Oxygen Reduction Rates Correlate with Reaction Overpotential in Acidic Organic Solutions. *ACS Cent. Sci.* **2016,** *2* (11), 850-856.

169. Connor, G. P.; Lease, N.; Casuras, A.; Goldman, A. S.; Holland, P. L.; Mayer, J. M., Protonation and electrochemical reduction of rhodium– and iridium–dinitrogen complexes in organic solution. *Dalton Transactions* **2017,** *46* (41), 14325-14330.

170. Creutz, S. E.; Peters, J. C., Catalytic reduction of N2 to NH3 by an Fe-N2 complex featuring a C-atom anchor. *J Am Chem Soc* **2014,** *136* (3), 1105-15.

171. Holloway, J. H.; Hope, E. G., Novel synthesis using inorganic fluorides. *J. Fluorine Chem.* **1996,** *76* (2), 209-212.

172. Fagnou, K.; Lautens, M., Halide Effects in Transition Metal Catalysis. *Angew. Chem. Int. Ed.* **2002,** *41* (1), 26-47.

173. Moore, C. M.; Szymczak, N. K., Redox-induced fluoride ligand dissociation stabilized by intramolecular hydrogen bonding. *Chem. Commun.* **2015,** *51* (25), 5490-5492.

174. Thammavongsy, Z.; LeDoux, M. E.; Breuhaus-Alvarez, A. G.; Seda, T.; Zakharov, L. N.; Gilbertson, J. D., Pyridinediimine Iron Dicarbonyl Complexes with Pendant Lewis Bases and Lewis Acids Located in the Secondary Coordination Sphere. *Eur. J. Inorg. Chem.* **2013,** *2013* (22-23), 4008-4015.

175. Felton, G. A. N.; Glass, R. S.; Lichtenberger, D. L.; Evans, D. H., Iron-Only Hydrogenase Mimics. Thermodynamic Aspects of the Use of Electrochemistry to Evaluate Catalytic Efficiency for Hydrogen Generation. *Inorg. Chem.* **2006,** *45* (23), 9181-9184.

176. da Mota, M. M.; Rodgers, J.; Nelson, S. M., The co-ordination number of transition-metal ions. Part VII. An evaluation of steric factors in the stabilisation of high-spin five-co-ordinate nickel(II) complexes of multidendate α-pyridyl ligands. *J. Chem. Soc. A* **1969,** *0* (0), 2036-2044.

177. Matsumoto, T.; Nagahama, T.; Cho, J.; Hizume, T.; Suzuki, M.; Ogo, S., Preparation and Reactivity of a Nickel Dihydride Complex. *Angew. Chem. Int. Ed.* **2011,** *50* (45), 10578-10580.

178. Takashita, K.; Matsumoto, T.; Yatabe, T.; Nakai, H.; Ogo, S., A Non-precious Metal, Ni Molecular Catalyst for a Fuel Cell Cathode. *Chem. Lett.* **2016,** *45* (2), 137-139.

179. Casitas, A.; Canta, M.; Solà, M.; Costas, M.; Ribas, X., Nucleophilic Aryl Fluorination and Aryl Halide Exchange Mediated by a CuI/CuIII Catalytic Cycle. *J. Am. Chem. Soc.* **2011,** *133* (48), 19386-19392.

180. Chatt, J.; Hayter, R. G., 167. Ligand field strengths of the halide, methyl, phenyl, and hydride anions. *Journal of the Chemical Society (Resumed)* **1961,** (0), 772.

181. Steiner, T., The hydrogen bond in the solid state. *Angew. Chem. Int. Ed.* **2002,** *41* (1), 48-76.

182. Steed, J. W.; Atwood, J. L., *Supramolecular Chemistry*. 2nd ed.; Wiley: West Sussex, 2009.

183. Huong, P. V.; Schlaak, M., Raman and infrared band shapes of the N・H+...X-hydrogen bond in trimethylaminium halide crystals. *Chem. Phys. Lett.* **1974,** *27* (1), 111-113.

184. Brammer, L.; Bruton, E. A.; Sherwood, P., Understanding the Behavior of Halogens as Hydrogen Bond Acceptors. *Cryst. Growth Des.* **2001,** *1* (4), 277-290.

185. Szajna-Fuller, E.; Chambers, B. M.; Arif, A. M.; Berreau, L. M., Carboxylate Coordination Chemistry of a Mononuclear Ni(II) Center in a Hydrophobic or Hydrogen Bond Donor Secondary Environment: Relevance to Acireductone Dioxygenase. *Inorg. Chem.* **2007,** *46* (14), 5486-5498.

186. Szajna, E.; Dobrowolski, P.; Fuller, A. L.; Arif, A. M.; Berreau, L. M., NMR studies of mononuclear octahedral Ni(II) complexes supported by tris((2-pyridyl)methyl)amine-type ligands. *Inorg. Chem.* **2004,** *43* (13), 3988-97.

187. Cambridge Structural Database, Version 5.41, October 2020, Cambridge Crystallographic Data Centre, 12 Union Road, Cambridge CB2 1EZ, UK.

188. Soshnikov, I. E.; Semikolenova, N. V.; Bryliakov, K. P.; Antonov, A. A.; Sun, W.-H.; Talsi, E. P., EPR spectroscopic study of Ni(I) species in the catalyst system for ethylene polymerization based on α-diimine Ni(II) complex activated by MMAO. *J. Organomet. Chem.* **2019,** *880*, 267-271.

189. Arendt, K. M.; Doyle, A. G., Dialkyl Ether Formation by Nickel-Catalyzed Cross-Coupling of Acetals and Aryl Iodides. *Angew. Chem. Int. Ed.* **2015,** *54* (34), 9876-9880.

190. Suh, M. P.; Oh, K. Y.; Lee, J. W.; Bae, Y. Y., Acetamide Coordination in a Nickel(I) Macrocyclic Complex: Synthesis, Properties, and X-ray Crystal Structure of a Five-Coordinate Nickel(I) Iminol Complex of 1,3,6,8,12,15-Hexaazatricyclo[13.3.1.18,12]icosane. *J. Am. Chem. Soc.* **1996,** *118* (4), 777-783.

191. Addison, A. W.; Rao, T. N.; Reedijk, J.; van Rijn, J.; Verschoor, G. C., Synthesis, structure, and spectroscopic properties of copper(II) compounds containing nitrogen–sulphur donor ligands; the crystal and molecular structure of aqua[1,7-bis(N-methylbenzimidazol-2′-yl)-2,6-dithiaheptane]copper(II) perchlorate. *J. Chem. Soc., Dalton Trans.* **1984,** (7), 1349-1356.

192. Manojlovic-Muir, L.; Muir, K. W.; Davis, W. M.; Mirza, H. A.; Puddephatt, R. J., A fluxional binuclear nickel(I) complex and evidence for reversible A-frame formation. *Inorg. Chem.* **1992,** *31* (5), 904-909.

193. Sacconi, L.; Dapporto, P.; Stoppioni, P., Synthesis, properties, and structural characterization of dinuclear halogen-bridged nickel(I) complexes with tris(2-diphenylarsinoethyl)amine. *Inorg. Chem.* **1977,** *16* (2), 224-227.

194. Gagne, R. R.; Ingle, D. M., One-electron-reduced nickel(II)-macrocyclic ligand complexes. Four-coordinate nickel(I) species and nickel(II)-ligand radical species which form paramagnetic, five-coordinate nickel(I) adducts. *Inorg. Chem.* **1981,** *20* (2), 420-425.

195. Jones, G. D.; Martin, J. L.; McFarland, C.; Allen, O. R.; Hall, R. E.; Haley, A. D.; Brandon, R. J.; Konovalova, T.; Desrochers, P. J.; Pulay, P.; Vicic, D. A., Ligand Redox Effects in the Synthesis, Electronic Structure, and Reactivity of an Alkyl−Alkyl Cross-Coupling Catalyst. *J. Am. Chem. Soc.* **2006,** *128* (40), 13175-13183.

196. Scarborough, C. C.; Lancaster, K. M.; DeBeer, S.; Weyhermüller, T.; Sproules, S.; Wieghardt, K., Experimental Fingerprints for Redox-Active Terpyridine in [Cr(tpy)2](PF6)n (n = 3–0), and the Remarkable Electronic Structure of [Cr(tpy)2]1–. *Inorg. Chem.* **2012,** *51* (6), 3718-3732.

197. Chirik, P. J.; Wieghardt, K., Radical Ligands Confer Nobility on Base-Metal Catalysts. *Science* **2010,** *327* (5967), 794-795.

198. Kannan, S.; Moody, M. A.; Barnes, C. L.; Duval, P. B., Fluoride Abstraction and Reversible Photochemical Reduction of Cationic Uranyl(VI) Phosphine Oxide Complexes. *Inorg. Chem.* **2006,** *45* (23), 9206-9212.

199. Khaled, M. B.; El Mokadem, R. K.; Weaver, J. D., Hydrogen Bond Directed Photocatalytic Hydrodefluorination: Overcoming Electronic Control. *J. Am. Chem. Soc.* **2017,** *139* (37), 13092-13101.

200. Erdmann, P.; Leitner, J.; Schwarz, J.; Greb, L., An Extensive Set of Accurate Fluoride Ion Affinities for p-Block Element Lewis Acids and Basic Design Principles for Strong Fluoride Ion Acceptors. *ChemPhysChem* **2020,** *21* (10), 987-994.

201. Yang, J. D.; Wang, Y.; Xue, X. S.; Cheng, J. P., A Systematic Evaluation of the N-F Bond Strength of Electrophilic N-F Reagents: Hints for Atomic Fluorine Donating Ability. *J Org Chem* **2017,** *82* (8), 4129-4135.

202. Yang, J.-D.; Wang, Y.; Xue, X.-S.; Cheng, J.-P., A Systematic Evaluation of the N–F Bond Strength of Electrophilic N–F Reagents: Hints for Atomic Fluorine Donating Ability. *The Journal of Organic Chemistry* **2017,** *82* (8), 4129-4135.

203. We acknowledge the differences between the BDE (homolytic) and FIA (heterolytic) parameters. In contrast to the FIA parameters, the BDE values for these substrates have been reported, and provide one guiding metric.

204. Chakraborty, S.; Chattopadhyay, J.; Guo, W.; Billups, W. E., Functionalization of Potassium Graphite. *Angew. Chem. Int. Ed.* **2007,** *46* (24), 4486-4488.

205. Hughes, R. P.; Lindner, D. C.; Rheingold, A. L.; Yap, G. P. A., Synthesis and Structure of the Thallium(I) Salt of the Tetrakis{3,5-bis(trifluoromethyl)phenyl}borate Anion. *Inorg. Chem.* **1997,** *36* (8), 1726-1727.

206. Beni, A.; Dei, A.; Laschi, S.; Rizzitano, M.; Sorace, L., Tuning the Charge Distribution and Photoswitchable Properties of Cobalt–Dioxolene Complexes by Using Molecular Techniques. *Chemistry – A European Journal* **2008,** *14* (6), 1804-1813.

207. Bruker, 2019. Apex3 v2019.1-0, SAINT V8.40A, Bruker AXS Inc.: Madison (WI), USA.

208. L. Krause, R. Herbst-Irmer, G.M. Sheldrick, and D. Stalke, J. Appl. Cryst., 2015, 48, 3-10.

209. CrystalClear Expert 2.0 r16, Rigaku Americas and Rigaku Corporation (2014), Rigaku Americas, 9009, TX, USA 77381-5209, Rigaku Tokyo, 196-8666, Japan.

210. CrysAlisPro 1.171.40.53 (Rigaku Oxford Diffraction, 2019).

211. SHELXTL suite of programs, Version 6.14, 2000-2003, Bruker Advanced X-ray Solutions, Bruker AXS Inc., Madison, Wisconsin: USA

212. Sheldrick, G.M. A short history of SHELX. Acta Crystallogr. A., 2008, 64, 1, 112-122.

213. a) Sheldrick, G.M. University of Göttingen, Germany, 2018. b) Sheldrick, G.M. Crystal structure refinement with SHELXL. Acta Crystallogr. Sect. C Struct. Chem., 2015, 71, 1, 3-8.

214. Hübschle, C.B., Sheldrick, G.M. & Dittrich, B. ShelXle: a Qt graphical user interface for SHELXL. J. Appl. Crystallogr., 2011, 44, 6, 1281-1284.

215. Decker, A.; Solomon, E. I., Dioxygen activation by copper, heme and non-heme iron enzymes: comparison of electronic structures and reactivities. *Curr. Opin. Chem. Biol.* **2005,** *9* (2), 152-163.

216. Gordon, Z.; Drummond, M. J.; Matson, E. M.; Bogart, J. A.; Schelter, E. J.; Lord, R. L.; Fout, A. R., Tuning the Fe(II/III) Redox Potential in Nonheme Fe(II)-Hydroxo Complexes through Primary and Secondary Coordination Sphere Modifications. *Inorg. Chem.* **2017,** *56* (9), 4852-4863.

217. Palaniandavar, M.; Visvaganesan, K., Mononuclear non-heme iron(III) complexes of linear and tripodal tridentate ligands as functional models for catechol dioxygenases: Effect of N-alkyl substitution on regioselectivity and reaction rate. *J Chem Sci* **2011,** *123* (2), 145-162.

218. Oloo, W. N.; Feng, Y.; Iyer, S.; Parmelee, S.; Xue, G.; Que, L., Cyclohexene as a substrate probe for the nature of the high-valent iron-oxo oxidant in Fe(TPA)-catalyzed oxidations. *New J. Chem.* **2013,** *37* (11), 3411-3415.

219. Ogo, S., H2 and O2 activation--a remarkable insight into hydrogenase. *Chem Rec* **2014,** *14* (3), 397-409.

220. Gordon, Z.; Miller, T. J.; Leahy, C. A.; Matson, E. M.; Burgess, M.; Drummond, M. J.; Popescu, C. V.; Smith, C. M.; Lord, R. L.; Rodríguez-López, J.; Fout, A. R., Characterization of Terminal Iron(III)–Oxo and Iron(III)–Hydroxo Complexes Derived from O2 Activation. *Inorg. Chem.* **2019,** *58* (23), 15801-15811.

221. Song, F.; Wang, C.; Falkowski, J. M.; Ma, L.; Lin, W., Isoreticular Chiral Metal−Organic Frameworks for Asymmetric Alkene Epoxidation: Tuning Catalytic Activity by Controlling Framework Catenation and Varying Open Channel Sizes. *J. Am. Chem. Soc.* **2010,** *132* (43), 15390-15398.

222. Tripodi, G. L.; Dekker, M. M. J.; Roithová, J.; Que Jr., L., Tuning the H-Atom Transfer Reactivity of Iron(IV)-Oxo Complexes as Probed by Infrared Photodissociation Spectroscopy. *Angew. Chem. Int. Ed.* **2021,** *60* (13), 7126-7131.

223. Ward, A. L.; Elbaz, L.; Kerr, J. B.; Arnold, J., Nonprecious Metal Catalysts for Fuel Cell Applications: Electrochemical Dioxygen Activation by a Series of First Row Transition Metal Tris(2-pyridylmethyl)amine Complexes. *Inorg. Chem.* **2012,** *51* (8), 4694-4706.

224. Pegis, M. L.; Roberts, J. A. S.; Wasylenko, D. J.; Mader, E. A.; Appel, A. M.; Mayer, J. M., Correction to Standard Reduction Potentials for Oxygen and Carbon Dioxide Couples in Acetonitrile and N,N-Dimethylformamide. *Inorg. Chem.* **2020,** *59* (12), 8638-8638.

225. Pegis, M. L.; Roberts, J. A. S.; Wasylenko, D. J.; Mader, E. A.; Appel, A. M.; Mayer, J. M., Standard Reduction Potentials for Oxygen and Carbon Dioxide Couples in Acetonitrile and N,N-Dimethylformamide. *Inorg. Chem.* **2015,** *54* (24), 11883-11888.

226. Tian, Z.; Fattahi, A.; Lis, L.; Kass, S. R., Cycloalkane and Cycloalkene C−H Bond Dissociation Energies. *J. Am. Chem. Soc.* **2006,** *128* (51), 17087-17092.

227. Fisher, K. J.; Feuer, M. L.; Lant, H. M. C.; Mercado, B. Q.; Crabtree, R. H.; Brudvig, G. W., Concerted proton-electron transfer oxidation of phenols and hydrocarbons by a high-valent nickel complex. *Chem. Sci.* **2020,** *11* (6), 1683-1690.

228. Bae, S. H.; Seo, M. S.; Lee, Y.-M.; Cho, K.-B.; Kim, W.-S.; Nam, W., Mononuclear Nonheme High-Spin (S=2) versus Intermediate-Spin (S=1) Iron(IV)–Oxo Complexes in Oxidation Reactions. *Angew. Chem. Int. Ed.* **2016,** *55* (28), 8027-8031.

229. Bordwell, F. G.; Cheng, J. P.; Satish, A. V.; Twyman, C. L., Acidities and homolytic bond dissociation energies (BDEs) of benzyl-type carbon-hydrogen bonds in sterically congested substrates. *The Journal of Organic Chemistry* **1992,** *57* (24), 6542-6546.

230. Warren, J. J.; Tronic, T. A.; Mayer, J. M., Thermochemistry of Proton-Coupled Electron Transfer Reagents and its Implications. *Chem. Rev.* **2010,** *110* (12), 6961-7001.

231. Connelly, N. G.; Geiger, W. E., Chemical Redox Agents for Organometallic Chemistry. *Chem. Rev.* **1996,** *96* (2), 877-910.

232. Russell, A. D.; Gilroy, J. B.; Lam, K.; Haddow, M. F.; Harvey, J. N.; Geiger, W. E.; Manners, I., Metal□Metal Bond Formation Between [n]Metallocenophanes: Synthesis and Characterisation of a Dicarba[2]ruthenocenophanium Dimer. *Chemistry – A European Journal* **2012,** *18* (26), 8000-8003.

233. Bruker (2019). Apex3 v2019.1-0, SAINT V8.40A, Bruker AXS Inc.: Madison (WI), USA

234. Krause, L., Herbst-Irmer, R., Sheldrick, G.M. & Stalke, D. (2015). J. Appl. Cryst. 48, 3-10

235. SHELXTL suite of programs, Version 6.14, 2000-2003, Bruker Advanced X-ray Solutions, Bruker AXS Inc., Madison, Wisconsin: USA; Sheldrick, G.M. A short history of SHELX. Acta Crystallogr A. 2008, 64(1), 112–122.

236. Sheldrick, G.M. A short history of SHELX. Acta Crystallogr A. 2008, 64(1), 112–122.

237. Sheldrick, G. M., "SHELXT--Integrated space-group and crystal-structure determination", Acta Crystallogr A. 2015, A71, 3-8.

238. a) Sheldrick, G.M. University of Göttingen, Germany, 2018. b) Sheldrick, G.M. Crystal structure refinement with SHELXL. Acta Crystallogr Sect C Struct Chem. 2015, 71(1), 3–8

239. Hübschle, C.B., Sheldrick, G.M. & Dittrich, B. ShelXle: a Qt graphical user interface for SHELXL. J. Appl. Crystallogr. 2011, 44(6), 1281–1284.

240. CrystalClear Expert 2.0 r16, Rigaku Americas and Rigaku Corporation (2014), Rigaku Americas, 9009, TX, USA 77381-5209, Rigaku Tokyo, 196-8666, Japan.

241. CrysAlisPro 1.171.40.53 (Rigaku Oxford Diffraction, 2019).

242. Sheldrick, G., Crystal structure refinement with SHELXL. *Acta Cryst. C* **2015,** *71* (1), 3-8.

243. Dolomanov, O. V.; Bourhis, L. J.; Gildea, R. J.; Howard, J. A. K.; Puschmann, H., OLEX2: a complete structure solution, refinement and analysis program. *J. Appl. Crystallogr.* **2009,** *42* (2), 339-341.

244. Hoffman, B. M.; Dean, D. R.; Seefeldt, L. C., Climbing Nitrogenase: Toward a Mechanism of Enzymatic Nitrogen Fixation. *Acc. Chem. Res.* **2009,** *42* (5), 609-619.

245. Horrell, S.; Kekilli, D.; Strange, R. W.; Hough, M. A., Recent structural insights into the function of copper nitrite reductases. *Metallomics* **2017**.

246. Kundu, S.; Kim, W. Y.; Bertke, J. A.; Warren, T. H., Copper(II) Activation of Nitrite: Nitrosation of Nucleophiles and Generation of NO by Thiols. *J. Am. Chem. Soc.* **2017,** *139* (3), 1045-1048.

247. Chandra Maji, R.; Mishra, S.; Bhandari, A.; Singh, R.; Olmstead, M. M.; Patra, A. K., A Copper(II) Nitrite That Exhibits Change of Nitrite Binding Mode and Formation of Copper(II) Nitrosyl Prior to Nitric Oxide Evolution. *Inorg. Chem.* **2018,** *57* (3), 1550-1561.

248. Kujime, M.; Izumi, C.; Tomura, M.; Hada, M.; Fujii, H., Effect of a tridentate ligand on the structure, electronic structure, and reactivity of the copper(I) nitrite complex: role of the conserved three-histidine ligand environment of the type-2 copper site in copper-containing nitrite reductases. *J. Am. Chem. Soc.* **2008,** *130* (19), 6088-6098.

249. Emsley, J., Very strong hydrogen bonding. *Chem. Soc. Rev.* **1980,** *9* (1), 91-124.

250. Bordwell, F. G.; Zhang, X. M.; Cheng, J. P., Bond dissociation energies of the nitrogen-hydrogen bonds in anilines and in the corresponding radical anions. Equilibrium acidities of aniline radical cations. *The Journal of Organic Chemistry* **1993,** *58* (23), 6410-6416.

251. Liang, H.-C.; Kim, E.; Incarvito, C. D.; Rheingold, A. L.; Karlin, K. D., A Bis-Acetonitrile Two-Coordinate Copper(I) Complex: Synthesis and Characterization of Highly Soluble B(C6F5)4- Salts of [Cu(MeCN)2]+ and [Cu(MeCN)4]+. *Inorg. Chem.* **2002,** *41* (8), 2209-2212.

252. CrystalClear Expert 2.0 r16, Rigaku Americas and Rigaku Corporation (2014), Rigaku Americas, 9009, TX, USA 77381-5209, Rigaku Tokyo, 196-8666, Japan.

253. CrysAlisPro 1.171.40.53 (Rigaku Oxford Diffraction, 2019).

254. Thordarson, P., Determining association constants from titration experiments in supramolecular chemistry. *Chem Soc Rev* **2011,** *40* (3), 1305-23.

255. *Gaussian 09, Revision A.02, M. J. Frisch, G. W. Trucks, H. B. Schlegel, G. E. Scuseria, M. A. Robb, J. R. Cheeseman, G. Scalmani, V. Barone, G. A. Petersson, H. Nakatsuji, X. Li, M. Caricato, A. Marenich, J. Bloino, B. G. Janesko, R. Gomperts, B. Mennucci, H. P. Hratchian, J.*

V. Ortiz, A. F. Izmaylov, J. L. Sonnenberg, D. Williams-Young, F. Ding, F. Lipparini, F. Egidi, J. Goings, B. Peng, A. Petrone, T. Henderson, D. Ranasinghe, V. G. Zakrzewski, J. Gao, N. Rega, G. Zheng, W. Liang, M. Hada, M. Ehara, K. Toyota, R. Fukuda, J. Hasegawa, M. Ishida, T. Nakajima, Y. Honda, O. Kitao, H. Nakai, T. Vreven, K. Throssell, J. A. Montgomery, Jr., J. E. Peralta, F. Ogliaro, M. Bearpark, J. J. Heyd, E. Brothers, K. N. Kudin, V. N. Staroverov, T. Keith, R. Kobayashi, J. Normand, K. Raghavachari, A. Rendell, J. C. Burant, S. S. Iyengar, J. Tomasi, M. Cossi, J. M. Millam, M. Klene, C. Adamo, R. Cammi, J. W. Ochterski, R. L. Martin, K. Morokuma, O. Farkas, J. B. Foresman, and D. J. Fox, Gaussian, Inc., Wallingford CT, 2016.

256. Rassolov, V. A.; Ratner, M. A.; Pople, J. A.; Redfern, P. C.; Curtiss, L. A., 6-31G* basis set for third-row atoms. *J. Comput. Chem.* **2001,** *22* (9), 976-984.

257. Blackaby, W. J. M.; Harriman, K. L. M.; Greer, S. M.; Folli, A.; Hill, S.; Krewald, V.; Mahon, M. F.; Murphy, D. M.; Murugesu, M.; Richards, E.; Suturina, E.; Whittlesey, M. K., Extreme g-Tensor Anisotropy and Its Insensitivity to Structural Distortions in a Family of Linear Two-Coordinate Ni(I) Bis-N-heterocyclic Carbene Complexes. *Inorg. Chem.* **2022**.

258. Blackaby, W. J. M.; Sabater, S.; Poulten, R. C.; Page, M. J.; Folli, A.; Krewald, V.; Mahon, M. F.; Murphy, D. M.; Richards, E.; Whittlesey, M. K., Mono- and dinuclear Ni(i) products formed upon bromide abstraction from the Ni(i) ring-expanded NHC complex [Ni(6-Mes)(PPh3)Br]. *Dalton Trans* **2018,** *47* (3), 769-782.

259. He, W.; Beattie, D. D.; Zhou, H.; Bowes, E. G.; Schafer, L. L.; Love, J. A.; Kennepohl, P., Direct metal–carbon bonding in symmetric bis(C–H) agostic nickel(i) complexes. *Chem. Sci.* **2021,** *12* (46), 15298-15307.

260. Wagner, C. L.; Herrera, G.; Lin, Q.; Hu, C. T.; Diao, T., Redox Activity of Pyridine-Oxazoline Ligands in the Stabilization of Low-Valent Organonickel Radical Complexes. *J. Am. Chem. Soc.* **2021,** *143* (14), 5295-5300.

261. Schneck, F.; Finger, M.; Siewert, I.; Schneider, S., Solvent dependent C−H Bond Strength in a Nickel Pincer Complex. *Zeitschrift für anorganische und allgemeine Chemie* **2021,** *647* (14), 1478-1485.

262. Valdez-Moreira, J. A.; Beagan, D. M.; Yang, H.; Telser, J.; Hoffman, B. M.; Pink, M.; Carta, V.; Smith, J. M., Hydrocarbon Oxidation by an Exposed, Multiply Bonded Iron(III) Oxo Complex. *ACS Cent. Sci.* **2021,** *7* (10), 1751-1755.

263. Di Berto Mancini, M.; Del Gelsomino, A.; Di Stefano, S.; Frateloreto, F.; Lapi, A.; Lanzalunga, O.; Olivo, G.; Sajeva, S., Change of Selectivity in C–H Functionalization Promoted by Nonheme Iron(IV)-oxo Complexes by the Effect of the N-hydroxyphthalimide HAT Mediator. *ACS Omega* **2021,** *6* (40), 26428-26438.

264. Munshi, S.; Sinha, A.; Yiga, S.; Banerjee, S.; Singh, R.; Hossain, M. K.; Haukka, M.; Valiati, A. F.; Huelsmann, R. D.; Martendal, E.; Peralta, R.; Xavier, F.; Wendt, O. F.; Paine, T. K.; Nordlander, E., Hydrogen-atom and oxygen-atom transfer reactivities of iron(iv)-oxo complexes of quinoline-substituted pentadentate ligands. *Dalton Transactions* **2022,** *51* (3), 870-884.

265. Dissanayake, D. M. M. M.; Petel, B. E.; Brennessel, W. W.; Bren, K. L.; Matson, E. M., Hydrogen bonding promotes diversity in nitrite coordination modes at a single iron(II) center. *J. Coord. Chem.* **2020,** *73* (17-19), 2664-2676.

266. Burns, K. T.; Marks, W. R.; Cheung, P. M.; Seda, T.; Zakharov, L. N.; Gilbertson, J. D., Uncoupled Redox-Inactive Lewis Acids in the Secondary Coordination Sphere Entice Ligand-Based Nitrite Reduction. *Inorg. Chem.* **2018,** *57* (16), 9601-9610.

267. Kwon, Y. M.; Delgado, M.; Zakharov, L. N.; Seda, T.; Gilbertson, J. D., Nitrite reduction by a pyridinediimine complex with a proton-responsive secondary coordination sphere. *Chem. Commun.* **2016,** *52* (73), 11016-11019.

268. Surya Prakash, G. K.; Hu, J.; Olah, G. A., Facile preparation of di- and monofluoromethyl ketones from trifluoromethyl ketones via fluorinated enol silyl ethers. *J. Fluorine Chem.* **2001,** *112* (2), 355-360.

269. Chen, K.; Que, L., Jr., Stereospecific alkane hydroxylation by non-heme iron catalysts: mechanistic evidence for an Fe(V)=O active species. *J Am Chem Soc* **2001,** *123* (26), 6327-37.

270. Ghosh, S.; Dey, A.; Sun, Y.; Scholes, C. P.; Solomon, E. I., Spectroscopic and Computational Studies of Nitrite Reductase: Proton Induced Electron Transfer and Backbonding Contributions to Reactivity. *J. Am. Chem. Soc.* **2009,** *131* (1), 277-288.

271. Cook, S. A.; Hill, E. A.; Borovik, A. S., Lessons from Nature: A Bio-Inspired Approach to Molecular Design. *Biochemistry* **2015,** *54* (27), 4167-4180.

272. Santoro, A.; Sambiagio, C.; McGowan, P. C.; Halcrow, M. A., Synthesis and coordination chemistry of 1,1,1-tris-(pyrid-2-yl)ethane. *Dalton Transactions* **2014,** *44* (3), 1060-1069.

273. Adam, K. R.; Anderson, P. A.; Astley, T.; Atkinson, I. M.; Charnock, J. M.; Garner, C. D.; Gulbis, J. M.; Hambley, T. W.; Hitchman, M. A.; Keene, F. R.; Tiekink, E. R. T., Stabilization of cobalt(I) by the tripodal ligandstris(2-pyridyl)methane and tris(2-pyridyl)phosphine. Structural,spectroscopic and ab initio studies of the[CoL2]n+ species. *J. Chem. Soc., Dalton Trans.* **1997,** *0* (4), 519-530.

274. Roberts, C. C.; Camasso, N. M.; Bowes, E. G.; Sanford, M. S., Impact of Oxidation State on Reactivity and Selectivity Differences between Nickel(III) and Nickel(IV) Alkyl Complexes. *Angew. Chem. Int. Ed.* **2019,** *58* (27), 9104-9108.

275. Cummins, D. C.; Yap, G. P. A.; Theopold, K. H., Scorpionates of the “Tetrahedral Enforcer” Variety as Ancillary Ligands for Dinitrogen Complexes of First Row Transition Metals (Cr–Co). *Eur. J. Inorg. Chem.* **2016,** *2016* (15-16), 2349-2356.

276. Fujisawa, K.; Sakuma, S.; Ikarugi, R.; Jose, A.; Solomon, E. I., Thermally stable manganese(III) peroxido complexes with hindered N3 tripodal ligands: Structures and their physicochemical properties. *J. Inorg. Biochem.* **2021,** *225*, 111597.

277. Lehnert, N.; Cornelissen, U.; Neese, F.; Ono, T.; Noguchi, Y.; Okamoto, K.-I.; Fujisawa, K., Synthesis and Spectroscopic Characterization of Copper(II)-Nitrito Complexes with Hydrotris(pyrazolyl)borate and Related Coligands. *Inorg. Chem.* **2007,** *46* (10), 3916-3933.

278. Zhao, L.; Shi, X.; Cheng, J., Calcium-Catalyzed Dehydrogenative Silylation of Aromatic Ethers with Hydrosilane. *ACS Catalysis* **2021,** *11* (4), 2041-2046.

279. Liu, Z.; Cao, S.; Yu, W.; Wu, J.; Yi, F.; Anderson, E. A.; Bi, X., Site-Selective C–H Benzylation of Alkanes with N-Triftosylhydrazones Leading to Alkyl Aromatics. *Chem* **2020,** *6* (8), 2110-2124.

280. Roberts, C. C.; Chong, E.; Kampf, J. W.; Canty, A. J.; Ariafard, A.; Sanford, M. S., Nickel(II/IV) Manifold Enables Room-Temperature C(sp3)–H Functionalization. *J. Am. Chem. Soc.* **2019,** *141* (49), 19513-19520.

281. Arikawa, Y.; Yamada, M.; Takemoto, N.; Horiuchi, S.; Sakuda, E.; Umakoshi, K., NO Migratory Insertion into Ruthenium–Aryl Bond with a Hydridotris(pyrazolyl)borato Ligand. *Organometallics* **2021,** *40* (3), 302-305.

282. Ünal, E. A.; Wiedemann, D.; Seiffert, J.; Boyd, J. P.; Grohmann, A., Efficient synthesis of pentakis- and tris(pyridine) ligands. *Tetrahedron Lett.* **2012,** *53* (1), 54-55.

283. Dahl, E. W.; Szymczak, N. K., Hydrogen Bonds Dictate the Coordination Geometry of Copper: Characterization of a Square-Planar Copper(I) Complex. *Angew. Chem. Int. Ed.* **2016,** *55* (9), 3101-3105.

284. Picci, G.; Kubicki, M.; Garau, A.; Lippolis, V.; Mocci, R.; Porcheddu, A.; Quesada, R.; Ricci, P. C.; Scorciapino, M. A.; Caltagirone, C., Simple squaramide receptors for highly efficient anion binding in aqueous media and transmembrane transport. *Chem. Commun.* **2020,** *56* (75), 11066-11069.

285. Wolf, F. F.; Neudörfl, J.-M.; Goldfuss, B., Hydrogen-bonding cyclodiphosphazanes: superior effects of 3,5-(CF3)2-substitution in anion-recognition and counter-ion catalysis. *New J. Chem.* **2018,** *42* (7), 4854-4870.

286. Schaufelberger, F.; Seigel, K.; Ramström, O., Hydrogen-Bond Catalysis of Imine Exchange in Dynamic Covalent Systems. *Chemistry – A European Journal* **2020,** *26* (67), 15581-15588.

287. Rostami, A.; Ebrahimi, A.; Husband, J.; Anwar, M. U.; Csuk, R.; Al-Harrasi, A., Squaramide–Quaternary Ammonium Salt as an Effective Binary Organocatalytic System for Oxazolidinone Synthesis from Isocyanates and Epoxides. *Eur. J. Org. Chem.* **2020,** *2020* (12), 1881-1895.

288. TAVERAS, A. G.; AKI, C. J.; BOND, R. W.; CHAO, J.; DWYER, M.; FERREIRA, J. A.; PACHTER, J.; BALDWIN, J. J.; KAISER, B.; LI, G.; MERRITT, J. R.; NELSON, K. H. J.; ROKOSZ, L. L. 3,4-DI-SUBSTITUTED CYCLOBUTENE-1, 2-DIONES AS CXC CHEMOKINE RECEPTOR ANTAGONISTS. 2003.

289. Takaishi, K.; Okuyama, T.; Kadosaki, S.; Uchiyama, M.; Ema, T., Hemisquaramide Tweezers as Organocatalysts: Synthesis of Cyclic Carbonates from Epoxides and CO2. *Org. Lett.* **2019,** *21* (5), 1397-1401.

290. Liedtke, T.; Hilche, T.; Klare, S.; Gansäuer, A., Condition Screening for Sustainable Catalysis in Single-Electron Steps by Cyclic Voltammetry: Additives and Solvents. *ChemSusChem* **2019,** *12* (13), 3166-3171.

291. Sandler, I.; Larik, F. A.; Mallo, N.; Beves, J. E.; Ho, J., Anion Binding Affinity: Acidity versus Conformational Effects. *The Journal of Organic Chemistry* **2020,** *85* (12), 8074-8084.

292. Larcher, A.; Nocentini, A.; Supuran, C. T.; Winum, J.-Y.; van der Lee, A.; Vasseur, J.-J.; Laurencin, D.; Smietana, M., Bis-benzoxaboroles: Design, Synthesis, and Biological Evaluation as Carbonic Anhydrase Inhibitors. *ACS Medicinal Chemistry Letters* **2019,** *10* (8), 1205-1210.

293. Yang, L.; Powell, D. R.; Houser, R. P., Structural variation in copper(i) complexes with pyridylmethylamide ligands: structural analysis with a new four-coordinate geometry index, τ4. *Dalton Transactions* **2007,** (9), 955-964.

294. Brookhart, M.; Grant, B.; Volpe, A. F., [(3,5-(CF3)2C6H3)4B]-[H(OEt2)2]+: a convenient reagent for generation and stabilization of cationic, highly electrophilic organometallic complexes. *Organometallics* **1992,** *11* (11), 3920-3922.

295. Butera, J. A.; Antane, M. M.; Antane, S. A.; Argentieri, T. M.; Freeden, C.; Graceffa, R. F.; Hirth, B. H.; Jenkins, D.; Lennox, J. R.; Matelan, E.; Norton, N. W.; Quagliato, D.; Sheldon, J. H.; Spinelli, W.; Warga, D.; Wojdan, A.; Woods, M., Design and SAR of Novel Potassium Channel Openers Targeted for Urge Urinary Incontinence. 1. N-Cyanoguanidine Bioisosteres Possessing in Vivo Bladder Selectivity. *J. Med. Chem.* **2000,** *43* (6), 1187-1202.